Fourier Based High-resolution Near-field Sound Imaging

Rick Scholte

Fourier Based High-resolution Near-field Sound Imaging

PROEFSCHRIFT

ter verkrijging van de graad van doctor aan de
Technische Universiteit Eindhoven, op gezag van de
Rector Magnificus, prof.dr.ir. C.J. van Duijn, voor een
commissie aangewezen door het College voor
Promoties in het openbaar te verdedigen
op donderdag 18 december 2008 om 16.00 uur

door

Rick Scholte

geboren te Zwolle

Dit proefschrift is goedgekeurd door de promotoren:

prof.dr.ir. N.B. Roozen
en
prof.dr. H. Nijmeijer

Copromotor:
dr.ir. I. Lopez

Contents

Nomenclature

List of Acronyms

Symbol   *Description*

A/D	analog-to-digital
ANSITE	automated near-field sound imaging technology Eindhoven
AR	autoregressive
ATM	acoustic transfer matrix
BEM	boundary element method
CCD	charge-coupled device
CNAH	cylindrical near-field acoustic holography
COS	cut-off and slope iteration
DFT	discrete Fourier transform
EPR	evanescent-to-propagating ratio
ESM	equivalent source method
FFT	fast Fourier transform
GCV	generalized cross-validation
HELS	Helmholtz least squares
IBEM	inverse boundary element method
IFRF	inverse frequency response function
IIR	infinite impulse response
NAH	near-field acoustic holography
NCP	normalized cumulative periodogram
OCV	ordinary cross-validation
PC	personal computer
PCA	principle component analysis
PET	polyethylene terephthalate
PNAH	planar near-field acoustic holography
RMSRE	root mean squared reconstruction error
SNR	signal-to-noise ratio
SONAH	statistically optimal near-field acoustic holography
SSR	spatial sensor resolution

List of Acronyms (continued)

Symbol	Description
SSIR	spatial sound image resolution
STSF	spatial transformation of sound fields
STW	Dutch technology foundation
TDIF	TASCAM digital interface

List of Symbols

Symbol	Description	Unit
a	prediction error coefficient	
$\mathbf{a}$	prediction error vector	
c	speed of sound	[m/s]
d_{sensor}	sensor diameter	[m]
E_z	maximum evanescent wave amplitude at distance z	
E_{z_h}	maximum evanescent wave amplitude at distance z_h	
E_{z_s}	maximum evanescent wave amplitude at distance z_s	
f	frequency	[Hz]
f_s	signal frequency	[Hz]
$\mathbf{F}$	spatial Fourier transform matrix	
$\mathbf{F}^{-1}$	inverse spatial Fourier transform matrix	
$\mathbf{G}$	forward propagation matrix	
h_i	prediction filter coefficient	
$\mathbf{h}$	impulse response vector	
$\mathbf{H}_f$	filter function matrix operator	
$H_{f,hp}$	high-pass filter function	
$H_f^{k_{co}}$	low-pass truncation filter function	
$H_f^{k_{co},\phi}$	modified exponential filter function	
$H_f^{k_{co},\gamma}$	exponential filter function	
H_f^{λ}	Tikhonov filter function	
$\mathbf{I_n}$	identity matrix	
k	wavenumber	[rad/m]
k_{co}	filter cut-off wavenumber	[rad/m]
k_{ev}	useful evanescent k-space content	[rad/m]
k_n	discrete wavenumber	[rad/m]
k_r	radiation circle wavenumber	[rad/m]
k_s	spatial sampling wavenumber	[rad/m]
k_x	wavenumber in x-direction	[rad/m]
k_{xy}	wavenumber in x, y-direction	[rad/m]

List of Symbols (continued)

Symbol	Description	Unit
k_y	wavenumber in y-direction	[rad/m]
k_z	wavenumber in z-direction	[rad/m]
L	Tikhonov filter weight function	
$\mathbf{L}$	Tikhonov filter weight matrix	
m	spatial index number in x-direction	
M	total number of elements in m	
n	spatial index number in y-direction	
n_b	border-padding index number	
N	total number of elements in n	
N_b	total number of elements in n_b	
N	maximum noise amplitude	
p	sound pressure	[Pa]
$\tilde{p}$	Fourier transformed sound pressure	[Pa]
$\tilde{p}_b$	border-padded $\tilde{p}$	[Pa]
$\tilde{p}_{ex}$	exact pressure on the source	[Pa]
$\tilde{p}_{re}$	reconstructed pressure on the source	[Pa]
$\hat{\tilde{p}}$	spatial Fourier transformed sound pressure	[Pa]
$\hat{\tilde{p}}_d$	discrete version of $\hat{\tilde{p}}$	[Pa]
$\hat{\tilde{p}}_{sf}$	filtered sound pressure at the source	[Pa]
$\tilde{p}_{s,\lambda}$	regularized sound pressure	[Pa]
$\hat{\tilde{p}}_{s,\lambda}$	regularized pressure in k-space	[Pa]
P_z	maximum propagating wave amplitude at distance z	
P_{z_h}	maximum propagating wave amplitude at distance z_h	
P_{z_s}	maximum propagating wave amplitude at distance z_s	
r_h	radial hologram or standoff distance	[m]
r_s	radial source distance	[m]
R	spatial resolution	[m]
S	maximum field amplitude	
t	time	[s]
$\hat{\tilde{v}}_x$	particle velocity in x-direction, k-space and frequency	[m/s]
$\hat{\tilde{v}}_y$	particle velocity in y-direction, k-space and frequency	[m/s]
$\hat{\tilde{v}}_z$	particle velocity in z-direction, k-space and frequency	[m/s]
w	spatial window vector	
w_j	weight function	
x	spatial coordinate scalar	[m]
X	spatial interval width in x-direction	[m]

List of Symbols (continued)

Symbol	Description	Unit
x_n	spatial discrete coordinate scalar	[m]
X_r	hologram circumference	[m]
$\mathbf{x}_{reg}$	regularized solution	
y	spatial coordinate scalar	[m]
Y	spatial interval width in y-direction	[m]
y_m	spatial discrete coordinate scalar	[m]
z	spatial coordinate scalar	[m]
z_h	hologram or standoff distance	[m]
z_s	source distance in the z-direction	[m]
α	tapering ratio	
γ	exponential filter factor	
δ	sensor distance or grid spacing	[m]
δ_s	spatial sensor distance or grid spacing	[m]
Δk	wavenumber interval	[rad/m]
ζ	ζ-criterion function	
η	perturbation norm	
$\hat{\eta}$	normalized perturbation norm	
κ	curvature	
λ	wavelength	[m]
λ	regularization parameter	
λ_s	sampling wavelength	[m]
ρ	residual norm	
$\hat{\rho}$	normalized residual norm	
ϕ	taper ratio (between 0 and 1)	
ϕ	minimum horizontal angle	[rad]
ω	angular frequency ($\omega = 2\pi f$)	[rad/m]
∇	gradient operator	
∂	differential operator	
$\sqcap_X$	spatial interval function in x-direction	
$\sqcap_Y$	spatial interval function in y-direction	
$\sqcap$	rectangular function	
$\sqcup$	spatial sampling function	
δ	Dirac function	

Introduction

Sound plays a major part in everyday life. Often sound is perceived as entertaining, annoying, communicative, functional, harmful, or most likely a combination of these. For industry it becomes more and more important to invest in low-noise design of their products due to increasingly stringent governmental policies and regulations regarding sound radiation and noise pollution. Also, a low-noise design yields less wear on components since their vibrations are minimized and life-time is potentially increased. Another benefit is the competitive advantage of a low-noise design, which is often preferred by customers. Additionally, there are often product specific reasons for the need to design and produce low-noise products. On the other hand, there are also functional requirements to optimally produce the correct sounds, since simply suppressing sound is not always beneficial in the sense of perception by the user. Take, for example, the quality aspects of a vacuum cleaner, an electric razor, the slamming of a car door, concert hall acoustics, the car navigation system that produces enough acoustic energy in order to be audible for the driver, the performance of a speaker system, a musical instrument, and so on. In almost every field of acoustics there is a need to better understand the source positions, behavior, intensity and physical insight in acoustic sources.

The past decades, many acoustic design tools and model-based approaches have emerged that aid in the design and calculation of the acoustic properties of products. However, an important impediment is that these tools simulate the acoustic behavior up to a certain accuracy. In practise it is very important that the acoustic behavior of products in a certain design phase is visualized accurately by means of measurement based analysis. More in detail, multiple acoustic measurements in front of and at a distance from a product are combined to calculate and visualize the acoustic sources on or close to the product surface. This process is known as inverse acoustics.

This thesis focusses on the further development of inverse acoustic methods by improving existing and developing new measurement and signal processing techniques, neces-

sary to make them widely applicable and industrially robust. The research is part of the project "Inverse Acoustics", which is a joint initiative of the Eindhoven University of Technology and the University of Twente, and funded by the Dutch Technology Foundation (Stichting Technische Wetenschappen, STW). Within this project three main research areas are defined and distributed over the three available groups. The research in the Dynamics and Control group at the Mechanical Engineering Department in Eindhoven focusses on "Measurement methods and signal processing in Inverse Acoustics".

1.1 Early history of sound visualization

Inverse acoustics are methods where acoustic measurements of sound radiation are performed at a certain distance from the source(s). These measurements are used to calculate the inverse solution of the acoustic wave equation and determine the sound distribution somewhere in between the actual source and the measurement area. An acoustic measurement based analysis method called acoustic holography was developed in the mid 1960s (30; 34), following the theory of optical holography from the late 1940s, which is developed by Gabor while he worked on resolution improvements of electron microscopes (5; 6). The brilliant idea of Gabor, which makes holography possible, is the addition of a reference wave, so the object wave is biased and thus indirectly records both the phase and the amplitude of the object wave instead of only the amplitude, which was common practise before. This method records light waves, emitted by a laser and reflected by an object of interest, on a light-sensitive film. By re-emitting laser light on the film it re-creates all the rays of light that originally came from the object, thus re-creating a three-dimensional image of the original object from a two-dimensional film also referred to as hologram. The term hologram refers to the Greek word 'holos' meaning 'whole' and 'gramma' meaning 'message': The two-dimensional hologram contains a complete, three-dimensional message or image of the source. The same theory holds for far-field acoustic hologram measurements, from which the inverse solutions of propagating sound waves are made, providing source localization at spatial resolutions in the order of the observed acoustic wavelength.

Use of near-field information for inverse determination of waveform patterns by means of holography was first introduced into the acoustic field by Williams and Maynard in the 1980s (59; 29). The near-field of a source includes evanescent waves that have spatial variations that are much smaller than the propagating wave patterns, thus potentially increasing the spatial resolution of inversely calculated source images. The use of two-dimensional spatial Fast Fourier Transform (FFT) allows a straightforward multiplication with an inverse propagation matrix based on Green's functions, which results in an extremely fast calculation of the source distribution on the area of interest, contrary to the two-dimensional spatial convolution with the sound propagation kernel required without two-dimensional FFT.

A second type of near-field inverse acoustic methods is model-based and applicable to arbitrary shaped objects. Two methods were introduced in the late 1980s: Gardner (7) introduced the inverse Helmholtz integral equation method followed by Veronesi (52) with a method based on the inversion of an acoustic transfer matrix (ATM), which is called Inverse Frequency Response Function (IFRF). There are two main types of IFRF methods, where one is based on measurements of the actual transfer paths, while the other is based on the Inverse Boundary Element Method (IBEM) (20). Both these techniques require a large amount of time to either measure or calculate the inverse ATM and also requires (in case of IBEM) a BEM model of the product under investigation.

Nowadays both NAH types are of major interest to both science and industry. One of the ongoing questions here is if the practical and industrial importance of arbitrary shapes outweighs the time consumption and engineering difficulties of implementing models. Often, in practical circumstances basic shapes closely in front of a product or source are more than adequate to visualize, detect and quantify the acoustic sources present. In most cases time constraints and ease of use are more important. Therefore, in this work the first type of inverse acoustic source calculation based on Fourier transforms is investigated, more in particular Planar and Cylindrical Near-field Acoustic Holography.

1.2 State of the art

1.2.1 Fourier based near-field acoustic holography

The acoustic wave-equation is a partial differential equation that describes the propagation of sound waves through a medium. Usually, when initial source conditions are known, the forward problem is easily calculated. However, in sound source identification where initial source conditions are unknown, the so-called inverse solution of the wave-equation is calculated. Soundwave properties at a certain distance from the source are used to back-propagate the sound waves to identify the original source. For continuous time and space the possibility exists to calculate the source exactly, but discretizing both space and time for computer calculations and visualization introduces distinct boundaries and uncertainties.

The acoustic wave equation for an infinitesimal change in sound pressure $p(x, y, z, t)$, continuous in time and space, from its equilibrium value is given by

$$\nabla^2 p(x, y, z, t) - \frac{1}{c^2} \frac{\partial^2 p(x, y, z, t)}{\partial t^2} = 0, \tag{1.1}$$

where c is the speed of sound and the Laplacian operator is defined as

$$\nabla^2 \equiv \frac{\partial^2}{\partial x^2} + \frac{\partial^2}{\partial y^2} + \frac{\partial^2}{\partial z^2}. \tag{1.2}$$

At a random position in space, sound pressure is observed in time. The linearity of sound waves makes it possible to separate the pressure signal in a number of sine waves by Fourier transforming $p(x, y, z, t)$. The Fourier transform of $p(x, y, z, t)$ results in sound pressure as a function of frequency f, but to avoid excessive appearances of π the angular frequency $\omega = 2\pi f$ is used. The continuous Fourier transform of $p(x, y, z, t)$ is

$$\tilde{p}(x, y, z, \omega) = \int\limits_{-\infty}^{\infty} p(x, y, z, t)e^{-j\omega t}dt. \tag{1.3}$$

Consider an infinite space with a number of sources in it and an infinite plane at $z = z_s = 0$, separating the source space from the source-free space. All sources of sound exist in the subspace where $z \leq z_s$, consequently for $z > z_s$ the medium holds no sources. At a distance $z > z_s$ in the source-free area the planar sound pressure information is observed as a function of x and y, parallel to the source plane. Equivalent to time-frequency Fourier analysis, Fourier transforming two-dimensional spatial sound pressure $\tilde{p}(x, y, z, \omega)$ projects sound pressure as wave frequencies or wavenumbers with a k_x and k_y component. The continuous spatial Fourier transform of $\tilde{p}(x, y, z, \omega)$ is defined as

$$\hat{\tilde{p}}(k_x, k_y, z, \omega) = \int\limits_{-\infty}^{\infty} \int\limits_{-\infty}^{\infty} \tilde{p}(x, y, z, \omega)e^{-j(k_x x + k_y y)}dxdy. \tag{1.4}$$

Given the source-free boundary condition for $z > 0$, the relationship between the Fourier Transform of the pressure in a plane $z = z_s = 0$ and the transform of the plane at $z > z_s$ is:

$$\hat{\tilde{p}}(k_x, k_y, z, \omega) = \hat{\tilde{p}}(k_x, k_y, 0, \omega)e^{jk_z z}. \tag{1.5}$$

Assume $\hat{\tilde{p}}(k_x, k_y, 0, \omega)$ is unknown, yet the sound pressure at a continuous plane parallel to the source plane in the source-free space at $z = z_h > z_s$ is available. The general expression to extrapolate k-space sound pressure spectrum from $z = z_h$ to a plane $z > z_s$ is

$$\hat{\tilde{p}}(k_x, k_y, z, \omega) = \hat{\tilde{p}}(k_x, k_y, z_h, \omega)e^{jk_z(z-z_h)}. \tag{1.6}$$

By using Euler's equation, the particle velocity k-space spectrum in normal direction $\hat{\tilde{v}}_z(k_x, k_y, z, \omega)$ can be determined from the sound pressure spectrum in k-space:

$$\hat{\tilde{v}}_z(k_x, k_y, z, \omega) = \hat{\tilde{p}}(k_x, k_y, z_h, \omega)\frac{k_z}{\rho c_0 k}e^{jk_z(z-z_h)}. \tag{1.7}$$

Equivalently, $\hat{\tilde{v}}_x(k_x, k_y, z, \omega)$, $\hat{\tilde{v}}_y(k_x, k_y, z, \omega)$ and sound intensity can be derived, also Near-field Acoustic Holography (NAH) is applicable to general form source areas,

including planar, cylindrical and spherical sources, see (56) and (41) for an extensive derivation and listing of all inverse solutions.

Spatial Transformation of Sound Fields (STSF) by Hald of Brüel&Kjær (10; 11), which is in fact a combination of PNAH and Principle Component Analysis (PCA). The STSF method deals with the detection and visualization of incoherent sources, the hologram measurements are basically split up in multiple incoherent holograms by means of PCA that are individually inverse calculated by PNAH. Drawbacks of this procedure are equal to PNAH, with the main concerns being k-space filtering and spatial windowing.

Patch NAH uses zero-padding and k-space regularization to iteratively extrapolate the measurement aperture or hologram (37; 58). The original hologram is then inserted into the extrapolated data, which is fed into the two-dimensional FFT again until a pre-defined threshold is met in order to stop the iterative process. Major impediments of these types of extrapolation are either the need for exact knowledge of the wavenumber content of the source of interest (38), or the assumption of white noise over the entire measurement aperture with a known variance (58). This results in a good performance for well-defined cases in a perfectly known and controllable environment, yet problems arise when the sources of interest are unknown together with the amount and type of noise or disturbance, which is often the case in more practical and industrial situations.

1.2.2   Other inverse acoustic methods

The last two decades various alternatives to NAH were developed. In 1995 Wang and Wu (54; 55) presented a method that avoids spatial windowing effects and is based on spherical wave expansions, the method is called the Helmholtz Least Squares (HELS) method. Again, the spatial windowing difficulties with NAH and the need to measure many more points triggered the development of another method that avoids spatial Fourier Transformation: Statistically Optimized Near-field Acoustic Holography (SONAH), which was introduced by Steiner and Hald in 1999 (48; 49) and further developed in 2003 by Hald (12). SONAH avoids the FFT entirely and calculates the inverse propagation from the hologram to the source plane by a spatial convolution. This method is one of the most popular procedures to deal with the leakage problems concerning the FFT. While there are still problems with practical application, especially in the presence of measurement noise and background noise (21; 13). Methods are investigated to regularize the inverse solutions and to counter background noise by the application of double layered arrays (14; 18).

Inverse Boundary Element Method (IBEM) or Inverse Frequency Response Function (IFRF) techniques were introduced by Veronesi (52) and developed by Ih and Kim (20; 24), and further investigated by Visser (53), a method that requires a BEM model of the source of interest and the calculation of an inverse transfer matrix. The inversion

process can be very accurate, but the main drawbacks are long calculation times and very extensive models in order to obtain high resolution images of the source distributions.

In IBEM the numerical computation of integrals considerably reduces the speed and efficiency of the method and for this reason the equivalent source method (ESM) or the method of superposition was introduced into the acoustical domain by Koopmann (26). The acoustic field in ESM is represented by a number of equivalent sources on a surface close to the structure surface or actual source of interest, the inverse matrix relation is similar to the one in IBEM, however, without the numerical computation of integrals. ESM applied to NAH was first introduced by Sarkissian (39; 40). According to Valdivia and Williams, who extensively compare IBEM and ESM with each other (51), there is a considerable speed increase with the application of ESM while methods show very similar reconstruction errors.

Problems considering the wide-spread practicability of aforementioned methods is what they have in common. In one way or the other, the methods are either too computationally intensive for effective application in industrial practise, or the inverse solutions require too much a priori knowledge of the source, such that only a carefully regulated research environment suffices, or the processing requires highly trained technicians to operate, etc. Effort and research considering these problems is made showing the growing amount of publications and interest in the topic of NAH and all of the alternative methods.

1.3 Challenges

The potential benefits of Fourier based NAH are greatly appreciated, but the practical difficulties mainly concerning spatial windowing and k-space filtering triggered the development of alternative methods described in section 1.2.2. This thesis discusses these practical difficulties of high-resolution Fourier based NAH and presents a theoretical basis, backed-up with numerical simulations and practical examples for dealing with these problems. The following subsections split the problem description into a scientific, more fundamental, part and the linked industrial challenges mostly facing the practical application.

1.3.1 Scientific challenges

The main scientific challenges that are addressed in this thesis are:

· Investigate the time-space constraints for NAH and develop methods to handle these constraints (standoff distance, spatial resolution, frequency band of interest, noise conditions, influence of surroundings, etc.).

· Counter the difficulties with spatial windowing for Fourier based NAH in a fast and

converging manner.

· Compare combinations of k-space filter functions and stopping rules and determine the optimal method which is suitable under a wide variety of conditions.

· Investigate incoherent sources discrimination methods suitable for NAH.

· Develop a framework to automatically render an "appropriate" solution for the provided inverse problem.

· Test the investigated and developed methods in numerical and practical experiments.

1.3.2 Industrial challenges

Important factors in industrially successful acoustic measurement and imaging systems are ease of use, flexibility and technical functionality. Functionality in the sense that it provides the required information in specific acoustic problems. In acoustic imaging practise often acoustic noise cancelation or acoustic performance problems are observed, but also vibration testing and modal analysis are optional.

The following challenges are faced in this thesis when industrial utilization of NAH is concerned:

· Wide applicability of NAH for a large number of different source types.

· Spatial sound image resolutions ranging from extremely small to large size apertures.

· Application in acoustically hazardous surroundings with background noise and reflecting surfaces.

· User-friendly measurement systems in order to determine an acoustic hologram.

· Development of a fully automated near-field sound imaging system suitable for non-expert usage and automated product quality control.

1.4 Objective

The main objective of this thesis is to investigate Fourier based NAH, identify the main problem areas concerning the implementation and application on a wide variety of sources, under different circumstances, in a wide resolution range, while taking into account industrial requirements considering practicability at utilization.

1.5 Contributions of the thesis

Near-field sound imaging requires a multidisciplinary approach in which all aspects from sound measurements to visualization and everything in between are carefully investigated, designed and integrated. This thesis presents a frame-work for full integration of

a high-resolution near-field sound imaging system built around a Fourier based inverse kernel. Various types of sensor systems are developed, built and tested that are suitable for extremely high spatial resolutions, but also for large measurement grids. The system is fully scalable and currently suitable for planar and cylindrical source or reconstruction surfaces. Given a required resolution and frequencies of interest, a sound imaging system is able to automatically determine measurement distance, inter-sensor distance and automatically calculate the inverse solution based on NAH.

More in detail, spatial properties with respect to aliasing, leakage and signal-to-noise ratio are investigated, and explicit methods and rules are developed to assist in proper determination of the acoustic holograms. A method to reduce leakage and avoid the spatial windowing problems is introduced, implemented and tested. This method, called border-padding, extrapolates truncated aperture information from the hologram outward, which makes the data more suitable for the two-dimensional spatial FFT.

Noise blows up in the ill-posed process of inverse near-field acoustics, thus regularization methods are required to find a trade-off between noise blow-up and suppression of required source information. Regularization methods are split up into filter functions and stopping rules, which are applied in k-space in case of Fourier based NAH. A number of newly developed filters are tested, compared to existing solutions and combined with various stopping rules that determine the proper k-space cut-offs for the filter. It is suggested to use both the cut-off and the filter slope in the regularization process. Cut-off and Slope iteration combines these filter parameters to properly and automatically determine the near-optimal modified low-pass k-space filters.

One of the major practical challenges for sound imaging is to move the measurement system out of the anechoic chamber or acoustic facilities and into more industrial settings. Especially background noise and reflections cause problems during measurements. NAH is shown to be less sensitive to background noise when certain boundary conditions are taken into account. The use of a double layered array is expected to make it possible to measure in small interiors, for example cars, planes, coaches, trucks and helicopters.

Numerical and experimental validation of the discussed topics and solutions are provided in detail with a number of fundamental tests in an anechoic environment, but also more practical cases in real industrial environments. The integration of fundamental developments in NAH and the industrial context is finalized in the patent pending ANSITE system, where ANSITE stands for "Automated Near-field Sound Imaging Technology Eindhoven".

1.6 Outline

In chapter 2 the spatial properties of the acoustic near-field with respect to the measurement device, source distance, surrounding disturbances, sensor positioning and total

measurement aperture are discussed. Spatial acoustic resolution, aliasing and leakage are phenomena that are defined and discussed. In order to minimize leakage after FFT and preserve information near the aperture edges, in chapter 3, a newly developed method called border-padding is introduced. This method makes it possible to measure small apertures without loss of information near the edges with minimal processing speed decrease. Regularization is applied to find a near-optimal trade-off between noise blow up and suppression of required source information. In chapter 4 regularization in k-space is devided in filter functions and stopping rules. A number of newly developed filter functions is compared to established filters and their parameters are set by utilizing various stopping rules. These stopping rules include Generalized Cross Validation (GCV), the L-curve criterion and the newly introduced Cut-Off and Slope (COS) iteration. Chapter 6 describes the integration of the developed and investigated methods into a single framework suitable for automated high-resolution NAH: the ANSITE technology. The fundamental and industrial validation of the presented methods is provided in chapter 7, where a number of case studies are discussed that cover a wide range of applications. Finally, chapter 8 presents the concluding remarks and future recommendations following the presented research.

Spatial properties in near-field acoustic holography

Proper spatial sampling of the acoustic near-field is the first, and very important, step in the correct implementation of a NAH system. This proces is part of the measurement phase where the acoustic hologram, which forms the input to the inverse calculation of the sound field, is built. In this chapter the major issues and concerns regarding the spatial properties of the NAH measurement are reviewed, defined and discussed. Section 2.1 gives the discrete solution of the inverse problem with PNAH that results after spatial sampling of the hologram plane. Discrete spatial sampling is carried out with a spatial sensor resolution, which, together with the influence of measurement noise (sensor noise, calibration errors or background disturbances for example), determines the resulting spatial sound image resolution that is defined in section 2.2. The correct standoff distance sought after in section 2.3 is small enough to guarantee a high spatial sound image resolution, and large enough to prevent spatial aliasing. In high-resolution sound imaging in particular, the set-up, size and sensitivity pattern of the sensor is very important since it acts like a k-space filter when the sensor dimensions are within the spatial sensor resolution, which is shown in section 2.4. Finally, an extensive numerical example that combines all previously mentioned spatial properties in NAH in section 2.5, followed by conclusions in section 2.6.

2.1 Spatial sampling and discrete inverse solution

2.1.1 discrete solution for PNAH

In practice, it is impossible to measure sound quantities continuously neither in space, nor in time. The finite measurement plane is best represented by a rectangular or truncation window, which basically is one at a given interval of time or space and zero outside. The spatial interval function in x-direction, $\sqcap_X(x)$, is defined by

$$\sqcap_X(x) = \begin{cases} 1, & |x| < X/2 \\ \frac{1}{2}, & |x| = X/2 \\ 0, & |x| > X/2. \end{cases} \tag{2.1}$$

Besides time sampling, discrete acoustic image processing requires spatial sampling in the form of a limited number of sensor positions, within the chosen spatial interval. The sampling function for the spatial domain x-direction is represented in the form of a Dirac comb function,

$$\sqcup(x) = \sum_{n=-\infty}^{\infty} \delta(x - x_n), \tag{2.2}$$

for a given sequence $\{x_n\}_{-\infty}^{\infty}$. For reasons of simplicity the pressure $\tilde{p}(x, y, z, \omega)$ observed at a distance z and a given angular frequency, ω, is written as $\tilde{p}_z(x, y)$. Spatially sampling a bounded plane $\tilde{p}_z(x, y)$ by applying (2.1) and (2.2) is mathematically described as

$$\tilde{p}_z(x_n, y_m) = \tilde{p}_z(x, y) \sqcap_X (x) \sqcap_Y (y) \sqcup (x) \sqcup (y). \tag{2.3}$$

Without taking any precautions with respect to leakage and aliasing, its corresponding angular spectrum $\hat{\tilde{p}}_z(k_x, k_y)$ for sequences $\{x_n\}_{-\infty}^{\infty}$ and $\{y_m\}_{-\infty}^{\infty}$ is computed by

$$\hat{\tilde{p}}_z(k_x, k_y) = \int_{-\infty}^{\infty} \int_{-\infty}^{\infty} \tilde{p}_z(x_n, y_m) e^{-j(k_x x + k_y y)} dx dy. \tag{2.4}$$

Taking the finite boundaries of the plane into account, the fully discretized pressure counterpart in k-space at the hologram plane, $\hat{\tilde{p}}_d(k_x, k_y)$, is written as

$$\hat{\tilde{p}}_d(k_x, k_y) = \sum_{n=-\frac{N}{2}}^{\frac{N}{2}-1} \sum_{m=-\frac{M}{2}}^{\frac{M}{2}-1} \tilde{p}_d(x_n, y_m) e^{-2\pi j(k_x \frac{n}{N} + k_y \frac{m}{M})} \tag{2.5}$$

The discrete solution of the wave-equation in k-space of an unknown, steady state pressure distribution $\tilde{p}_z(k_x, k_y)$ in a source-free half-space, $z > 0$, is defined in (59) as

$$\hat{\tilde{p}}_d(k_{x_n}, k_{y_m}, z) = \hat{\tilde{p}}_d(k_{x_n}, k_{y_m}, z_h) e^{jk_z(z-z_h)}, \tag{2.6}$$

where $z = z_h$ is the hologram distance. From (2.6) it follows that k_z is determined from the wavenumbers in both $x-$ and $y-$direction, i.e. k_x and k_y, and the acoustic wavenumber, k, that follows from ω and c_0. In k-space, k_z is determined by $k_z = \pm\sqrt{k^2 - k_x^2 - k_y^2}$ of which three types of solutions to this equation, with k already known, can be found:

$$k_x^2 + k_y^2 = 0 \qquad\qquad plane\ wave\ in\ z-direction, \qquad (2.7)$$

$$0 < k_x^2 + k_y^2 \leq k^2 \qquad\qquad propagating\ waves;\ k_z\ real, \qquad (2.8)$$

$$k_x^2 + k_y^2 > k^2 \qquad\qquad evanescent\ waves;\ k_z\ complex. \qquad (2.9)$$

The radiation circle lies exactly at $k^2 = k_x^2 + k_y^2$ and is denoted as k_r, outside this circle waves are evanescent, whereas inside waves are propagating. Applying (2.6) to propagating waves ((2.7) and (2.8)) results in a phase shift, evanescent waves (2.9) are multiplied in k-space by an exponential power of increasing strength with increasing k_z. Before this operation in k-space is possible, the spatial data is first pre-processed before the FFT is applied. The pre-processing includes the reduction of leakage, yet this topic is extensively discussed in chapter 3. Here, the sampling function and the influence of the higher, evanescent wavenumbers on the spatial resolution of the sound images are the main focus.

2.2 Spatial resolution

Originally, the spatial resolution was derived in the context of optical and electron microscopy, where the most well-known definition is the Rayleigh criterion (35), which originated from light optics. This criterion states that resolution is the minimum distance by which two point scatterers must be separated to be discernible for a given wavelength and aperture of the imaging system. In remote sensing technology, for example earth observation or weather satellite imaging, spatial resolution is defined as the minimum separation between two objects for which the images appear distinct and separate (36). Note that this is not the size of the smallest detectable object, although resolution and scale of an image make estimation of it possible. Digital image processing, however, uses other definitions of spatial resolution. Here, spatial resolution is often defined as the measure of how closely lines in an image are resolved or, also, the number of independent pixel values per unit length. For NAH a slightly different definition of spatial resolution is introduced, which is split up into the spatial sensor and spatial sound image resolution.

2.2.1   spatial sensor resolution

The spatial sensor resolution (SSR) is comparable to the pixel resolution in digital image processing, where images are built from a number of pixels per inch (ppi) or dots per

inch (dpi). The spatial sensor resolution is introduced as the number of sensors per unit length or sensors per meter (spm). The SSR is calculated by the inverse of the minimal sensor distance or grid spacing δ_s in a regular or rectangular array of sensors:

$$SSR = \frac{1}{\delta_s} = \frac{k_s}{\pi} \; [spm] , \qquad (2.10)$$

where $k_s = \frac{2\pi}{\lambda_s}$ is the sampling wavenumber, with λ_s the sampling wavelength, and $\delta_s = \frac{1}{2}\lambda_s$. The spatial sensor resolution is the hard lower limit for the smallest variations in the spatial sound field that can be observed. In NAH practice, the sound image resolution is worse than the sensor resolution limit after the inverse solution is determined, which is mainly due to noise and other errors.

2.2.2 spatial sound image resolution

Here, the spatial sound image resolution (SSIR) is defined as the minimum distance between two sound sources for which the sound images resolve as unique and separate. The question is when two sources are actually separate. In optics, a commonly used alternative interpretation of the Rayleigh criterion (35; 22) states that the dip between two maxima of two Gaussian-shaped image features of similar intensity can be resolved if it measures at least 21% of the maximum. Figure 2.1a shows an unresolved identification of two sources, while the sources in Figure 2.1b are clearly resolved with a dip of 21% with respect to the maximum value. Another way to define sound image resolutions from an image is given in (25), which depends on the full width, half maximum principle. In practice it is easier to determine a dip of at least 21% than full width, half maximum values in a sound image, so the proposed measure based on the Rayleigh criterion is used in practical cases. In case there are no evanescent waves available from the measurements and $\delta_s < 2\lambda$, the minimal $SSIR$ is determined by the free field acoustic wavelength λ:

$$SSIR_{min} = \frac{\lambda}{2}. \qquad (2.11)$$

This can be defined as the minimum resolution for an acoustic image, provided $\delta_s < \lambda$, which is the resolution that can be obtained by classical beam-forming or acoustic holography. For NAH, it is suggested to use the cut-off wavenumber, k_{co}, of the proper k-space low-pass filter in the determination of the actual spatial sound image resolution:

$$SSIR = \frac{\pi}{k_{co}}. \qquad (2.12)$$

(a) unresolved   **(b)** resolved   **(c)** full width half maximum
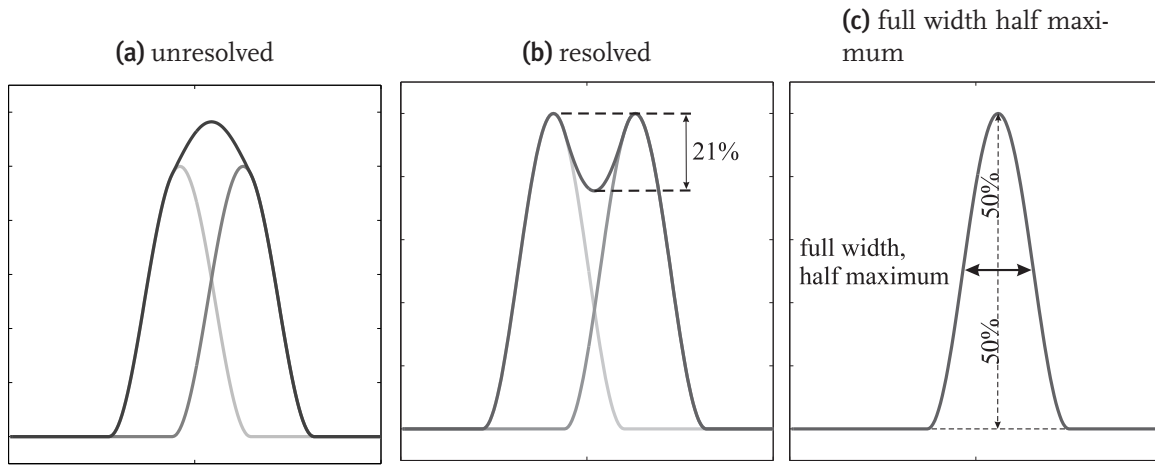
Figure 2.1: visualization of spatial sound image resolution definitions

Reason for this is that the k-space low-pass filter determines which wavenumbers are passed or stopped; the higher the cut-off wavenumber, the smaller the potential detail in the resulting sound images. Critical in this process is the proper determination of k_{co}, since a wrong choice heavily influences the potential SSIR: a higher than optimal k_{co} possibly results in the identification of sources that are actually noise, and a lower than optimal k_{co} heavily degrades the potential SSIR. More on the subject of near-optimal k-space filtering is given in chapter 4.

2.2.3 influence of measurement noise on resolution

Measurement noise influences the complete k-space spectrum, however, especially the evanescent waves given by (2.9) are of concern. In order to understand the influence of noise on inverse acoustics problems, it helps to observe it from a measurement point of view. A sensor array measures the hologram at a certain standoff distance from the source. Due to sensor noise, calibration differences across the array, background noise, etc., a certain noise level amplitude E exists. Now, for propagating waves the noise hardly poses a problem, because these are generally well above the noise floor and are identified easily, also further into the (free) field. On the other hand, evanescent wave amplitudes drop with an exponential power as a function of the measurement distance, while the noise floor remains more or less stable. This behavior is visualized in Figure 2.2. The evanescent wave amplitude drops with an exponential power with respect to the propagating wave amplitude. The evanescent wave is undistinguishable from the noise when the amplitude drops below the noise floor (bottom of Figure 2.2), at this distance the boundary between near-field and far-field for this specific case is set. Also, the outer boundary of the near-field varies inversely with the signal frequency, which can be derived from (2.6) for example. Practically speaking, the acoustic near-field becomes larger when the
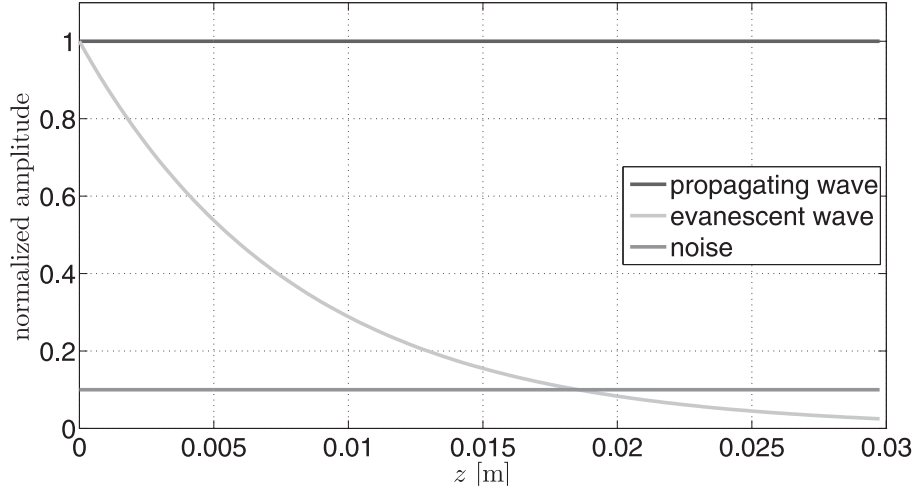
Figure 2.2: influence of measurement or standoff distance z on the evanescent wave amplitude that drops below the noise floor

error level of the measurement system drops, or the signal-to-noise ratio improves. The dynamic range or signal-to-noise ratio SNR between the maximum field amplitude, S, for a propagating wave and N, the noise amplitude, is given by

$$SNR = 20 \log_{10} \left(\frac{S}{N} \right).$$

<div align="right">(2.13)</div>

For an evanescent wave, this means the SNR drops with increasing standoff distance, up to the point where $SNR = 0$ dB. Now, the evanescent waves cannot be distinguished from the noise, and the evanescent information is considered useless for the inverse calculation, since chances are great that the noise will blow up as the reconstruction distance increases. For higher wavenumbers and greater standoff distance the space is no longer considered to be the near-field of the source under investigation. This is an important quantity, because the SNR influences the maximum observable wavenumber as a function of the standoff distance, $(z_h - z_s)$. Maynard and Williams (29) determined the spatial resolution, R, based on the assumption that both the maximum propagating and evanescent wave have equal amplitudes at the source ($z = z_s = 0$):

$$R = \frac{\pi}{\sqrt{k^2 + \left(\frac{SNR \ln 10}{20(z_h - z_s)} \right)^2}}.$$

<div align="right">(2.14)</div>

Often in practice, though, the evanescent wave amplitude near the source is much higher than the propagating counterpart. Here, a derivation is given of the $SSIR$ that takes different levels of the maximum evanescent and propagating field amplitudes at the source

plane into account. First, the evanescent-to-propagating ratio EPR_z is defined:

$$EPR_z = 20 \log_{10} \left(\frac{E_z}{P_z} \right),$$
(2.15)

where E_z is the maximum evanescent wave amplitude and P_z is the maximum propagating wave amplitude both at a distance $z > 0$. The propagating wave has a constant amplitude while it travels from the source plane to the hologram plane in the near-field, and the evanescent wave decays with an exponential power as a function of wavenumber and distance. The maximum evanescent wave amplitude at the source plane E_{z_h} is

$$E_{z_h} = E_{z_s} e^{-(z_h - z_s)\sqrt{k_x^2 + k_y^2 - k^2}}.$$
(2.16)

In order to reconstruct the evanescent wave E_{z_s} properly, E_{z_h} must be larger than the noise amplitude N:

$$E_{z_s} e^{-(z_h - z_s)\sqrt{k_x^2 + k_y^2 - k^2}} > N.$$
(2.17)

From (2.15) and $P_{z_s} = P_{z_h}$, it follows that $E_{z_s} = P_{z_h} 10^{\frac{EPR_{z_s}}{20}}$, thus (2.17) can be written as

$$\sqrt{k_x^2 + k_y^2 - k^2} < \frac{\ln \left(\frac{P_{z_h} 10^{\frac{EPR_{z_s}}{20}}}{N} \right)}{(z_h - z_s)},$$
(2.18)

$$\sqrt{k_x^2 + k_y^2 - k^2} < \frac{\ln \left(\frac{P_{z_h}}{N} \right) + \ln \left(10^{\frac{EPR_{z_s}}{20}} \right)}{(z_h - z_s)}.$$
(2.19)

Now, fill in $S = P_{z_h}$ in (2.13) and use this in (2.19), which results in

$$\sqrt{k_x^2 + k_y^2 - k^2} < \frac{(SNR + EPR_{z_s}) \ln 10}{20(z_h - z_s)},$$
(2.20)

and

$$SSIR = \frac{\pi}{\sqrt{k^2 + \left(\frac{(SNR + EPR) \ln 10}{20(z_h - z_s)} \right)^2}}.$$
(2.21)

To illustrate the behavior of the SNR and EPR, their influence on the $SSIR$ is visualized in Figure 2.3. It is clear that the EPR is of significant influence on the obtainable resolution; for example, a hologram measurement at $z_h = 1$ cm, a signal frequency $f = 1$ kHz and a $SNR = 30$ dB shows an increase in $SSIR$ from 7 to 5 cm when the EPR changes from 0 to 30 dB. From these results, one might conclude that, for the best NAH results (highest $SSIR$), a high-quality measurement system (maximum SNR), as close to the source as possible (small standoff distance $z_h - z_s$) should be chosen, however, in the next section it is shown that this is not always a good choice.
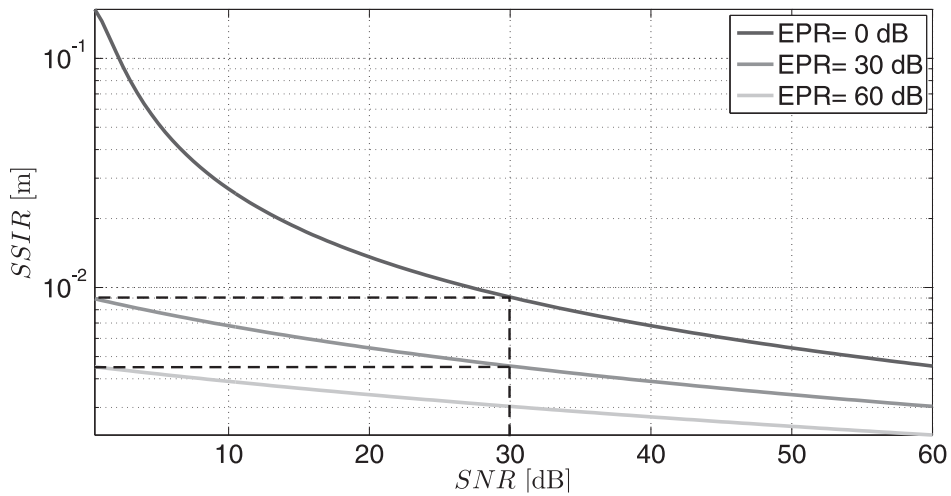
Figure 2.3: $SSIR$ changes after PNAH for increasing SNR of the maximum propagating wave amplitude at a fixed standoff distance $z_h = 1$ cm, $f = 1$ kHz and three different values of the EPR

2.3 Standoff distance and spatial aliasing

2.3.1 spatial aliasing

An important issue when acquiring a holographic measurement is the distance from the tip of the sensor to the source plane, i.e.: $z_h - z_s$. From (2.21), it follows that the resolution strongly depends on the standoff distance, because a decrease in size boosts resolution. There are two main reasons why decreasing the standoff distance, $z_h - z_s$, has its limits. The first reason is the influence of the sensor on the acoustic behavior of the source. Diffraction and a change in acoustic impedance can be of great importance on short distances. The second reason is the spatial sampling resolution, or the minimal sensor distance δ_s. The minimal sensor distance and standoff distance are interlinked because of aliasing effects. Aliasing is a well-known issue in digital signal processing and is a result of the under-sampling of data.

Spatial aliasing can best be explained by showing an example of a two-dimensional waveform, where two waveforms of different frequencies travel in two different directions, see Figure 2.4. In the following illustrations dark areas mark high sound pressure, whereas light areas mark low sound pressure. The interfering wave pattern is illustrated in Fig-

(a)　　　　　　(b)　　　　　　(c)　　　　　　(d)
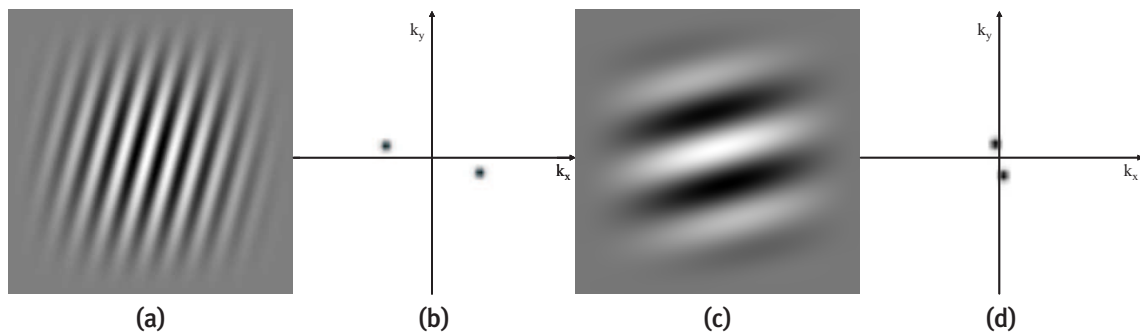
Figure 2.4: separate wave patterns and corresponding wavenumber spectra; the wave illustrated in (a) has the smallest wavelength that results in a spectrum (b) with energy in the highest wavenumbers, whereas the wave illustrated in (c) has the largest wavelength and energy in the lower wavenumbers, illustrated in (d).

ure 2.5a. From this waveform, a two-dimensional FFT results in the waveform spectrum of Figure 2.5d. The two components can be clearly discriminated from the image, which also shows the different directions and waveform frequencies. Given exactly the same input, but now sampled at a fixed rate (Figure 2.5b), which is lower than the wavenumber of the highest waveform present in the sample, results in an under sampled wavenumber spectrum. The dotted square shows the Nyquist waveform frequency, and it is clear from Figure 2.5e that the original spectrum in the dash-dotted ellipses is now infinitely repeated in all directions. Because the sampling rate is too low, the neighboring spectra overlap and energy in the higher waveform is positioned in a lower waveform. The new spectrum is shown in the dotted area, which marks the Nyquist waveform frequency again. This effect is called spatial aliasing. The inverse Fourier transformation of this spectrum results in a completely different waveform as can be seen in Figure 2.5c. Note that zero-padding outside the Nyquist wavenumber is applied to properly interpolate the resulting spatial information.

2.3.2   natural anti-aliasing filter

In time domain digital signal processing, typically, a low-pass filter applied before sampling is used to ensure that frequencies higher than half the sampling frequency are not present. However, it is not possible to apply an analogue filter for spatial acoustic data, because the high wavenumbers are present in the near-field of the source and cannot
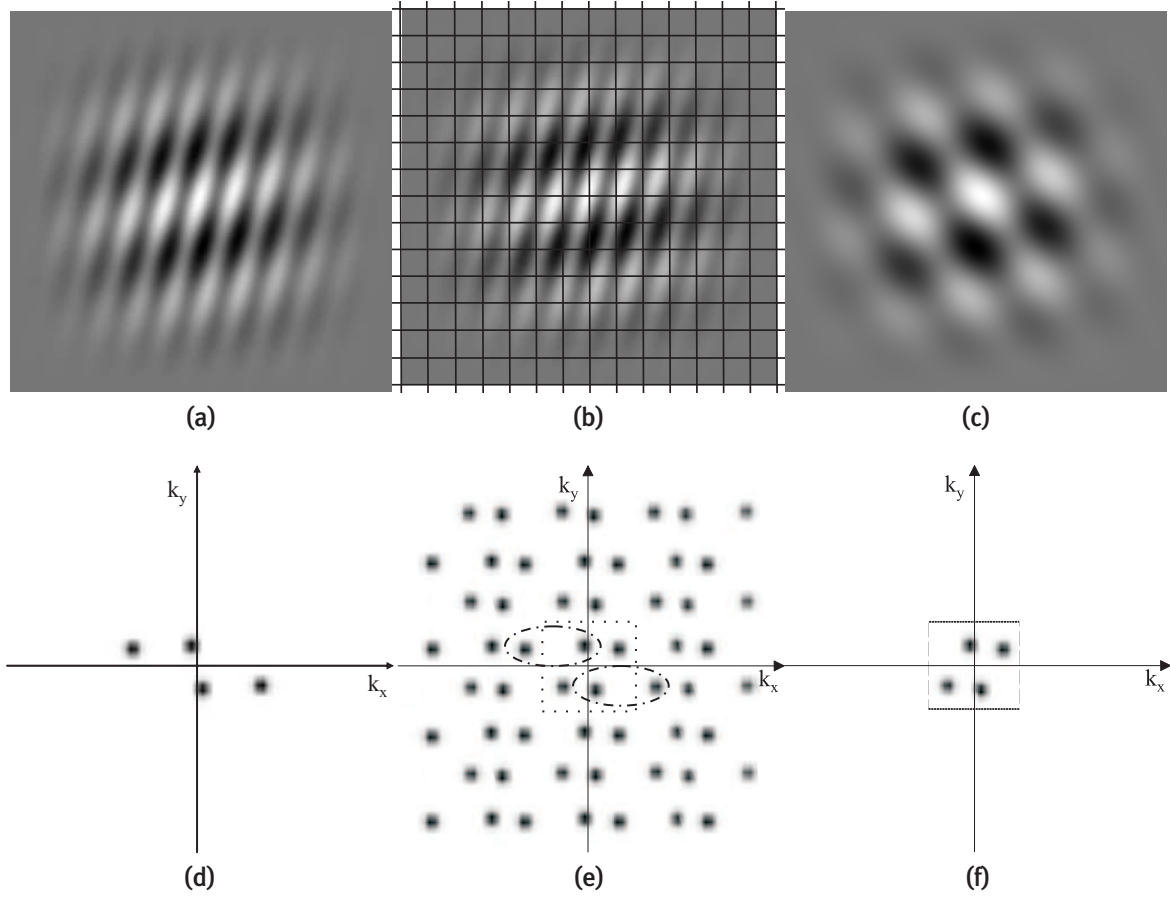
Figure 2.5: wave pattern where two waves travel in different directions (a), which results in the wavenumber domain (d) that clearly shows energy at particular wave frequencies in two directions. Spatial undersampling (b) of the waveform from (a), every line crossing marks a sample or sensor position. After FFT, this results in a repetitive wavenumber domain (e). The zero-padded, aliased wavenumber domain (f) results in a different waveform compared to the original in (a) after the inverse FFT is applied (c).

be suppressed, without interrupting the acoustic properties of the field between source and hologram plane. A spatial anti-aliasing filter is in effect when a proper choice of the standoff distance is made, since the highest observable wavenumber depends on this distance. The proper choice of the standoff distance is in fact a natural anti-aliasing filter. In accordance with the Nyquist criterion, it is clear that half the sampling wavenumber, $\frac{1}{2}k_s$, is the maximum observable wavenumber in a noise free environment. A noise free environment implies that $SNR \rightarrow \infty$ and the R from (2.14), which considers the effect of measurement noise on the resolution only, becomes approximately zero. This effect is

limited by the SSR from (2.10) due to spatial sampling. When the inequality (47),

$$\sqrt{k^2 + \left(\frac{SNR \ln 10}{20(z_h - z_s)}\right)^2} > \frac{1}{2}k_s, \tag{2.22}$$

is true, aliasing is likely to occur. In other words, there exists a distance $z_h - z_s$ below which, at a certain dynamic range, aliasing is likely to occur at a chosen SSR, because from this distance on evanescent waves higher than the Nyquist wavenumber are observable. Note that this always depends on the actual source distribution, and it is also assumed that the propagating and evanescent parts at the source are equally strong (a required property for (2.10)). Inequality (2.22) couples spatial sampling, standoff distance and signal-to-noise ratio, which makes it possible to wisely set the measurement parameters. The dark line in Figure 2.6 illustrates inequality (2.22).

However, when the evanescent and propagating parts at the source are not in a one-to-one ratio ($EPR \neq 0$ dB) at the source, the inequality in (2.22) becomes

$$\sqrt{k^2 + \left(\frac{(SNR + EPR) \ln 10}{20(z_h - z_s)}\right)^2} > \frac{1}{2}k_s. \tag{2.23}$$

Especially when the evanescent part of the source is stronger than the propagating part ($EPR_{z_s} > 0$ dB), the aliasing probability increases significantly. Figure 2.6 displays three graphs that mark the border between a zone with possible spatial aliasing and an aliasing free zone. The graphs represent the standoff distance z_h against the SNR for a fixed
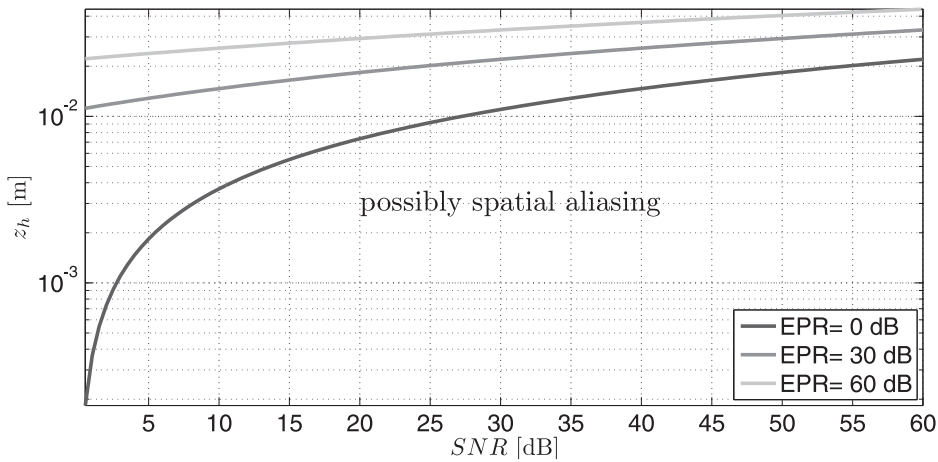
Figure 2.6: standoff distance z_h plotted against the SNR for $\delta = 1$ cm and $f_s = 1$ kHz; the graph separates the area with potential aliasing (below the lines) and the aliasing free zone (above the lines) for three given values of the EPR
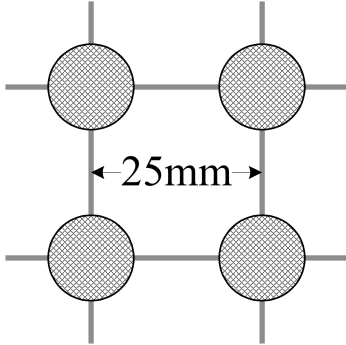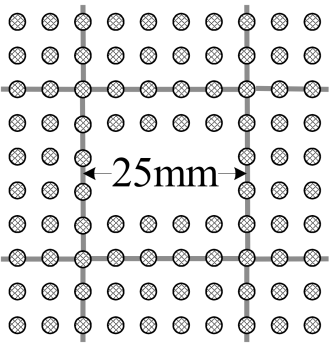
$\delta = 1$ cm, $f_s = 1$ kHz and three different values of the EPR. If $EPR = 0$ dB, which is also the case in (2.22), and $SNR = 20$ dB, the choice of $z_h = 5$ mm is below the aliasing graph, and is likely to cause spatial aliasing. However, when $z_h = 8$ mm, aliasing is avoided and a relatively good $SSIR$ is obtained. For $EPR > 0$ dB, the aliasing free standoff distance becomes much larger. For example, with $EPR = 30$ dB and $SNR = 20$ dB, a $z_h = 8$ mm would not suffice and at least a distance of $z_h = 2$ cm corresponds to an aliasing free measurement.

In practice, the EPR is very hard to determine in contrast to the other factors in (2.23), which are relatively easy to measure. However, given this framework, it is possible to investigate the influence of aliasing on the results obtained with NAH. Most likely, with additional information, either an estimate of the EPR or the detection of aliasing occurrence during a measurement can be made. Spatial aliasing can only be avoided by using a save standoff distance and a correct spatial sensor resolution, given a good estimate of the EPR.

2.3.3 choice of sensor, distance and sampling

Two types of array setups are considered here, in order to illustrate the consequences of sensor choice, distance and spatial sampling resolution on the sound image resolution and the possible effects of spatial aliasing. The parameters of both setups are listed in Table 2.1, including an illustration of the grid size of either setup.

Table 2.1: microphone sensor array setups

name	array one	array two
type	large size, few sensors	small size, many sensors
sensor diameter	$d_1 = 12.5$ mm	$d_2 = 2.5$ mm
sampling distances	$\delta_1 = 25$ mm	$\delta_2 = 5$ mm
sensor quality	$SNR_1 = 45$ dB	$SNR_2 = 25$ dB
grid setup	25mm	25mm

Consider two types of sensors in an array: array one contains a small number of high
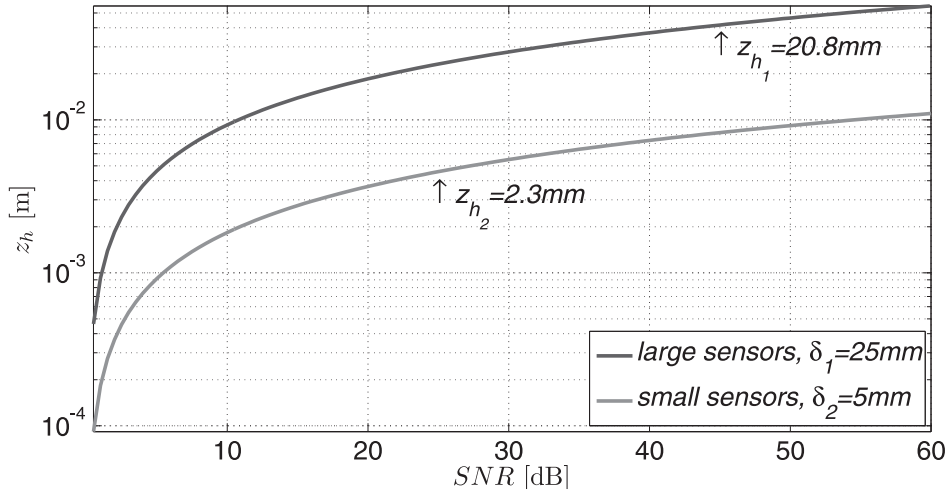
Figure 2.7: standoff distance z_h plotted as a function of SNR for $\delta_1 = 25$ mm in the array with large sensors and $\delta_2 = 5$ mm in the array with small sensors; $f_s = 1$ kHz

quality sensors, and array two holds a large number of low quality sensors that cover the same hologram area, the frequency of interest is $f_s = 1$ kHz. First, assume an $EPR = 0$ dB. The graphs in Figure 2.7 show the standoff distance as a function of SNR for both setups.

It follows that $z_{h_1} = 20.8$ mm for array one, which means the array should at least be placed at this standoff distance to avoid spatial aliasing and $SSIR \geq 25$ mm. Array two is safely applied at $z_{h_2} \geq 2.3$ mm, which grants a resolution of $SSIR \geq 5$ mm. This means that array two can be placed much closer to the source than array one.

The minimum obtainable $SSIR$ becomes larger when both arrays are moved away from z_h and the source (straight up in the graph), which results in less detail in the sound images with the same array. Obviously, when the arrays are moved closer to the source plane, which means z_h drops below the curves for both cases, spatial aliasing is very likely to occur. Also, when the EPR becomes larger than zero, the optimal z_h increases and the curves are followed to the right and upward (effectively, the EPR can be added to the SNR).

The fact that array one, with the high quality sensors, should be moved further away than array two, with the low quality sensors, is a nice paradox. Even when the high quality sensors have equal diameters and the same SSR compared to the lower quality sensors, this array should still be moved further away from the source to avoid spatial aliasing.

2.4 Sensor movement and size

A widely used construction for spatially sampling a sound field is a static array of microphones, capable of both observing stationary and non-stationary sound sources. Draw-

backs of this method are the spatial resolution restrictions, following the physical dimensions of the microphones, requirements of open space in between the individual sensors, and the high demands for parallel signal acquisition systems. An alternative for the static
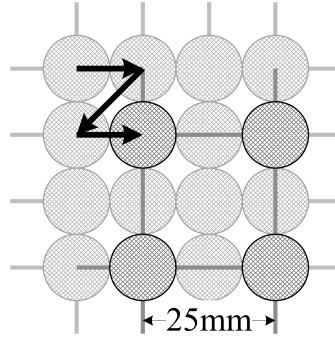
Figure 2.8: high resolution traverse measurement with an array; the arrows show the consecutive steps by the traverse system, $\delta = 12.5$ mm

array is the application of a traverse system with a scanning sensor or scanning sensor array, as is shown in Figure 2.8. The microphone is traversed over a predefined grid, measuring sound pressure at every single position. All positions combined make up the acoustic information of a certain area, stored in matrix form. A reference signal is used to correct phase differences over the full grid.

In order to measure and process acoustic information at a resolution higher than possible with a static array it is required to use a different strategy; in this case the traverse system is used to increase the spatial sampling rate of the sensor array and move the array or sensor in small steps to cover the measurement aperture. Important factors herein are the choice for the minimum step size and the sensor size, which provides the average sound pressure over the pressure sensitive area of the microphone membrane. The effective sensor area determines the maximum resolution possible with conventional NAH methods. This is due to the fact that the sensor size acts as a kind of k-space low-pass filter.

Ideally, the sensor membrane should be infinitely small, so it would sample an infinitely small part of the pressure field when the sensor is placed in that position. In that case, the spatial sampling rate of the traverse system could be chosen infinitely high. In practice, this is not the case and the consequences of finite sensor membrane sizes are illustrated in Figure 2.9, and explained here. In order to easily illustrate the spatial sampling and sensor size trade-off, a one-dimensional case is considered. The sensor membranes are equally sensitive over their full length and detect the average sound pressure over this length. Now, the first case is a wave with wavelength $\lambda = 25$ mm, which is shown in Figure 2.9a. Sensor one is $\frac{1}{2}\lambda$ wide and the traverse system step size is only $\delta = 2.5$ mm, which results in a pressure image that is slightly smoothed and stretched (a lower value in k-space). On the other hand, sensor two is small enough to nicely image the pressure
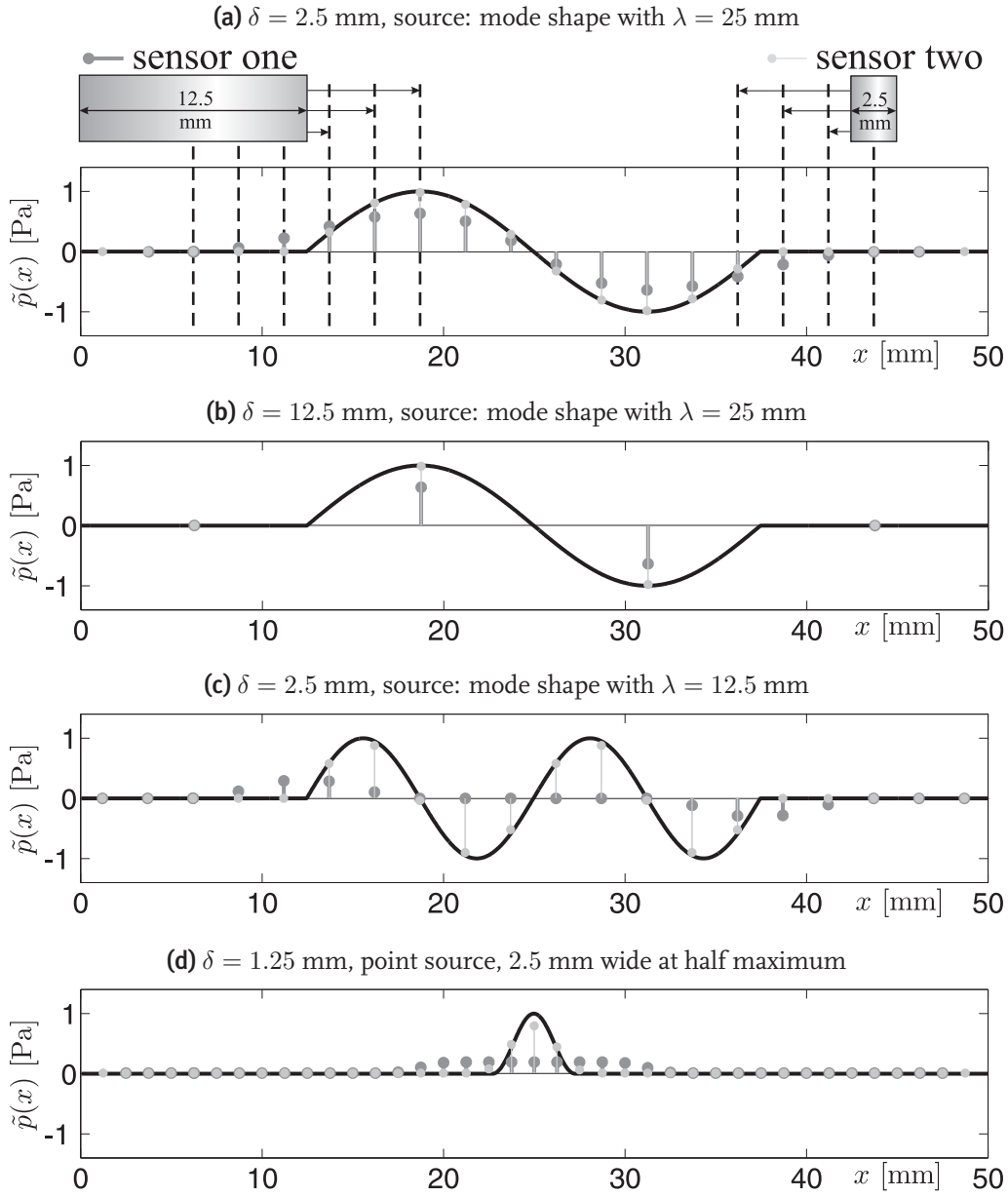
Figure 2.9: influence of step size δ and sensor size on resulting pressure values (gray dotted samples) of various high wavenumber source distributions (black graphs); sensor one is relatively large with $d_1 = 12.5$ mm and sensor two is small with $d_2 = 2.5$ mm

distribution, without any smoothing and including the correct values along the aperture. Secondly, the same wave pattern is used in Figure 2.9b as in the previous case, however, now the spatial step size, $\delta = 25$ mm, is a factor ten larger. This results in a correct detection of the wavenumber by both sensors, although sensor one still underestimates the sound pressure. A slight movement of either the source or sensor one results in a smoothed result again.

Figure 2.9c shows what happens when the sensor diameter $d_{sensor} > \frac{1}{2}\lambda$: much smooth-

ing, underestimation of the pressure and even parts that show a blind spot for sensor one. Still, sensor two manages to correctly represent the sound pressure distribution, because $d_1 < \frac{1}{2}\lambda$

Finally, a point-like source with a width of 2.5 mm at half maximum is plotted in Figure 2.9d. Here, sensor two starts to show some smoothing and a slight underestimation of the pressure, which is expected at a low step size of only $\delta = 1.25$ mm. On the other hand, the result based on sensor two is completely smeared out over d_1 plus the source width. This shows that great care should be taken in the choice of sensor size and the step size of the traverse system, when no additional measures are taken. Preferably, the sensor membrane is as small and sensitive as possible, with a low noise floor.

2.5 Numerical example

From the above sections, it is clear that the best spatial sampling results are obtained with the smallest sensor membranes that are still of good quality (high SNR), preferably with $d_{sensor} \leq \delta$ and a standoff distance that fulfills (2.23). Here, a numerical test is presented that aims to incorporate all these aspects of spatial sampling in the acoustic near-field of a sound source, and illustrate the consequences of good and bad spatial settings of a hologram measurement.

First, the applied sensors and other hologram measurement parameters are listed in

Table 2.2: parameters numerical example of spatial properties in NAH

sensor diameters	d_1	12.5 mm	d_2	2.5 mm
sampling distances	δ_1	2 mm	δ_2	8 mm
hologram size	X	12 cm	Y	12 cm
standoff distances	z_{h_1}	5 mm	z_{h_2}	10 mm
evanescent propagating ratios	EPR_1	0 dB	EPR_2	10 dB
frequency of interest			f_s	5 kHz
signal-to-noise ratio			SNR	30 dB

Table 2.2. Again, the small and the relatively large sensor that are known from the previous sections are used here, for comparison reasons, both sensors have the same quality which results in an equal SNR of the propagating wave amplitude. This measurement is only possible with a moving sensor or moving array, because the step sizes are small. The sources of interest are shown in Figure 2.10b and c; source one with $EPR = 0$ dB (equal wave amplitudes for the propagating and evanescent parts) and source two with $EPR = 10$ dB (maximum evanescent wave amplitude is larger than the maximum propagating wave amplitude) respectively. The sources contain three modes; the first mode is a (1,1)-mode ($\lambda_1 = 12$ cm) that almost fully covers the aperture, the second mode is a (3,3)-

(a) standoff distance graph

(b) source one $EPR = 0$ dB

(c) source two $EPR = 10$ dB
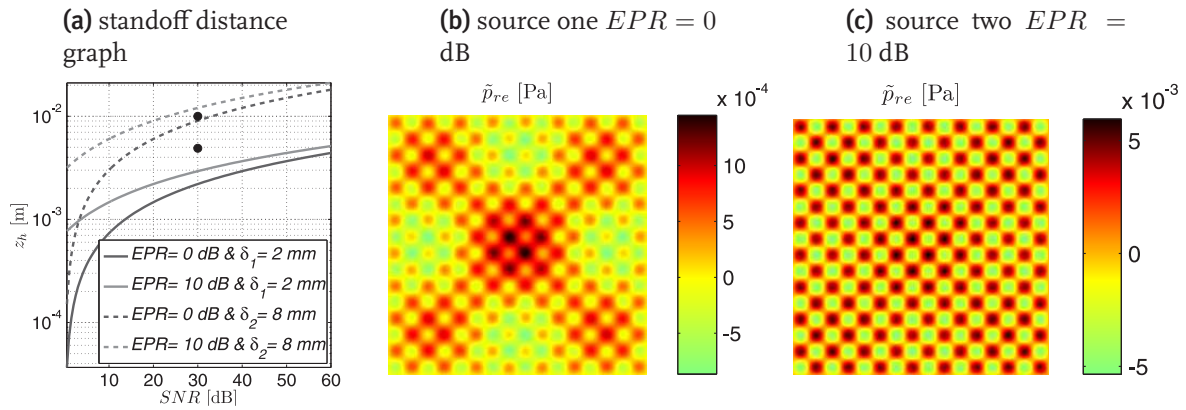
Figure 2.10: sensor one is relatively large with $d_1 = 12.5$ mm and sensor two is small with $d_2 = 2.5$ mm

mode ($\lambda_2 = 7$ cm) that lies just within the radiation circle in k-space, whereas mode three ($\lambda_3 = 1.5$ cm) is evanescent. The modes are super-positioned on top of one another and the frequency of interest is $f_s = 5$ kHz. Figure 2.10a shows the standoff distance graphs for EPR_1, EPR_2, δ_1 and δ_2 combined, the two black dots mark $z_{h_1} = 5$ mm (lower) and $z_{h_2} = 10$ mm (upper) at $SNR = 30$ dB.

The sound pressure distributions at z_{h_1} and z_{h_2} as a result of forward propagation of the two source planes are calculated on a fine grid of 512 by 512 points, then the fine grid is sampled with δ_1 and δ_2 for both the sensor diameters. White noise is added to the hologram apertures to simulate noise of the measurement system ($SNR = 30$ dB). These holograms are shown in Figure 2.11 and 2.12, paired with the solutions after PNAH.

The results of PNAH on source one in Figure 2.11 comply with the graphs for $EPR = 0$ dB in Figure 2.10a, the k-space filter cut-offs are determined with (2.21). As expected, the sensor with d_1 and δ_1 used at z_{h_1} gives the best result after PNAH (Figure 2.11a), which is almost equal to the original source image (Figure 2.10b). Further away from the source, at z_{h_2}, the evanescent waves are lost in the noise and the result is smoothed by the filter. Also, from Figure 2.11b, it is clear that the large sensor membrane acts as a low-pass filter; the result from δ_1 and z_{h_1} shows some detail of the evanescent pattern, however, it is heavily distorted and smoothed.

From Figure 2.11c, it is clear that $\delta_2 = 8$ mm is likely to result in spatial aliasing when $z_{h_1} = 5$ mm is used. The spatial aliasing is especially clear in Figure 2.11c, where parts of the image look like a checkerboard; the wavenumber of $\lambda_3 = 1.5$ cm folds back around $k = \frac{2\pi}{0.016}$. This behavior corresponds to the spatial aliasing analysis in Figure 2.5, where the higher wavenumbers are projected on lower wavenumbers, which results in a faulty pattern. The large sensor partly smoothes the spatial aliasing, yet it is still visible in Figure 2.11d. At $z_{h_2} = 10$ mm, the $SSIR$ of the results is low, yet spatial aliasing is not visible.

Now, the evanescent pattern is amplified at the source, such that $EPR = 10$ dB, which
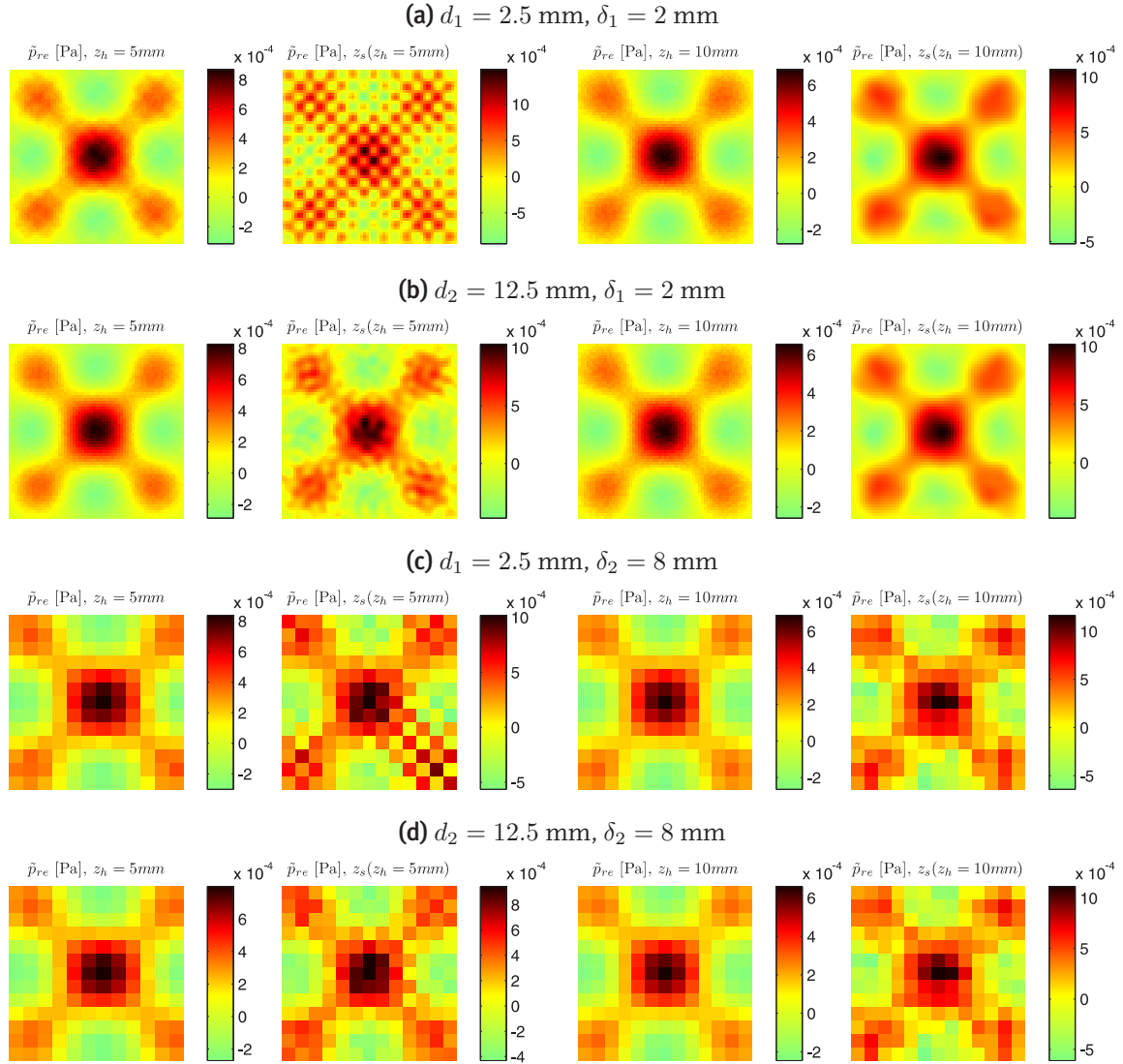
Figure 2.11: results of sampling and PNAH of source one for $SNR = 30$ dB and $EPR = 0$ dB; left pairs show hologram at $z_{h_1} = 5$ mm and source (after PNAH), right pairs show hologram at $z_{h_2} = 10$ mm and source (after PNAH)

results in the fine sound pressure source image in Figure 2.10c. Again, the results that follow from the minimum spatial sampling distance $\delta_1 = 2$ mm do not suffer from spatial aliasing, which is illustrated in Figure 2.12a and b. Also, the difference between the small sensor and the smoothing sensor with diameter $d_1 = 12.5$ mm is very clear; again, the results with δ_1 at z_{h_1} with the small sensor are superior, both qualitatively and quantitatively. Spatial aliasing is now clearly visible in the results following from the holograms with $\delta_2 = 8$ mm at $z_{h_1} = 5$ mm in Figure 2.12c and d. Especially the difference between Figure 2.11c and Figure 2.12c is clear for $z_{h_1} = 5$ mm; the lower black dot in Figure 2.10a lies further below the curve of $EPR = 10$ dB than the curve of $EPR = 0$ dB, and thus causes more aliasing disturbance in the results. The black dot for δ_2 and z_{h_2} is right in be-
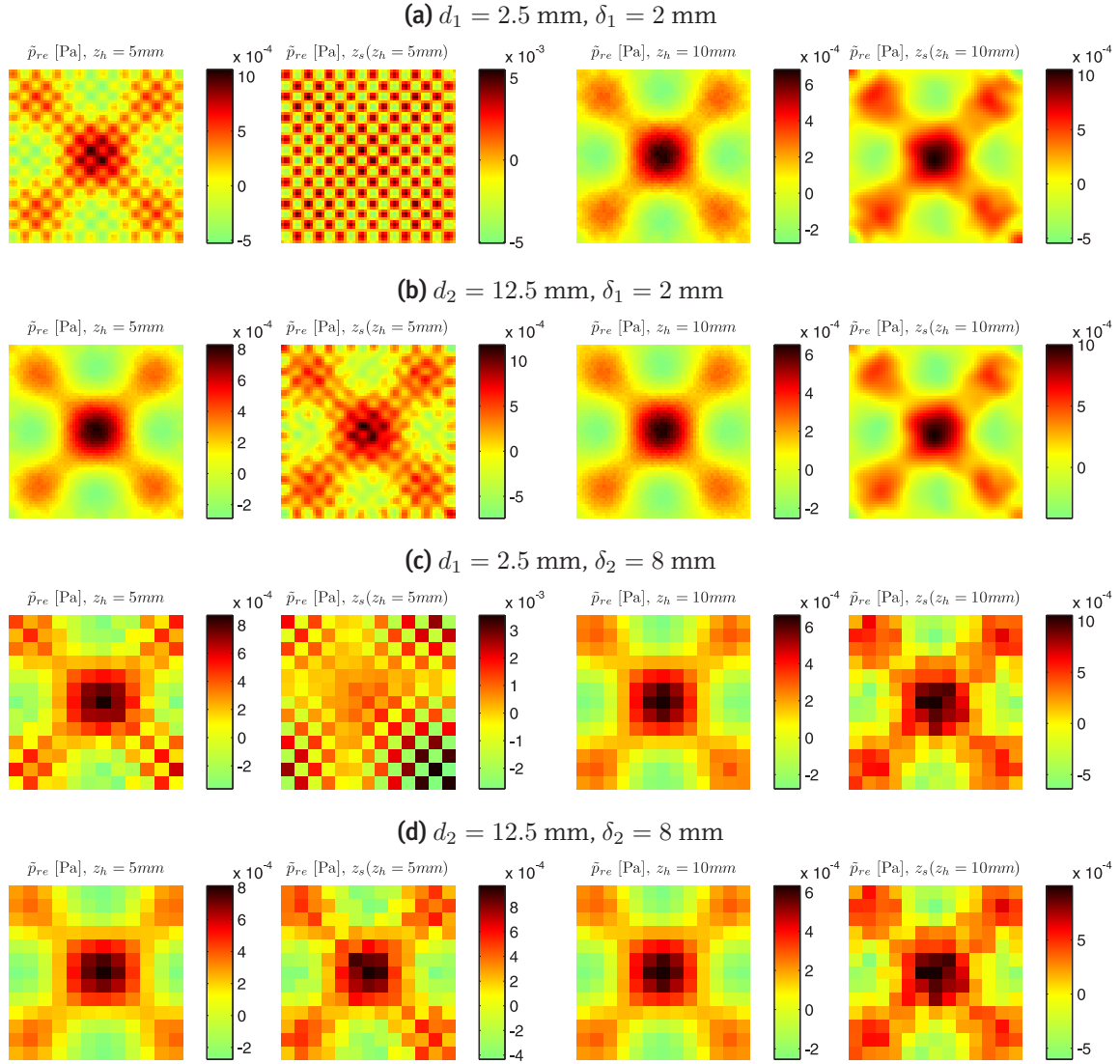
Figure 2.12: results of sampling and PNAH of source two for $SNR = 30$ dB and $EPR = 10$ dB; left pairs show hologram at $z_{h_1} = 5$ mm and source (after PNAH), right pairs show hologram at $z_{h_2} = 10$ mm and source (after PNAH)

tween the dashed curves that represent $EPR = 0$ dB and $EPR = 10$ dB in Figure 2.10a, which means spatial aliasing is likely to occur in Figure 2.12c and d (the right pairs of images). There are indeed disturbances and differences compared to the results in Figure 2.12a and b, but it is hard to validate in this case.

This numerical example clearly shows the influence of sensor size, spatial sampling rate, standoff distance, and the evanescent-to-propagating wave ratio that was introduced in this chapter. A small sensor is capable of obtaining higher spatial resolutions when the measurements are performed as close to the source as possible, however, the spatial aliasing criterion should be respected carefully. Also, the best spatial sampling results are obtained with the smallest sensor membranes of good quality (high SNR), preferably with

$d_{sensor} \leq \delta$ and a standoff distance that fulfills (2.23).

2.6 Discussion

The correct setup of the spatial properties in NAH is the first essential step in the sound imaging process. Major sources of error are spatial aliasing and a wrong choice of sensor size and spatial sensor resolution. Spatial aliasing is caused by either incorrect spatial sampling, small standoff distance, high signal-to-noise ratio (SNR) of the measurement system, high evanescent-to-propagating ratio (EPR), or a combination of these. The standoff distance acts as a natural anti-aliasing filter when the spatial sensor resolution is fixed, a criterion is provided that helps determine aliasing free standoff distances. This criterion, see (2.23), characterizes in one inequality the standoff distance, SNR and EPR for which aliasing will (likely) occur. Also, the spatial sound image resolution is defined, and the influence of noise on the results is quantified. Most of the presented work is directly applicable to other forms of NAH, including cylindrical and spherical apertures. Also non-Fourier based inverse acoustic near-field methods benefit from these considerations, since these are also bound to the Nyquist sampling theory. Local variations in the sound-field, which prove necessary for a correct representation of the source image, might be overlooked if a too coarse spatial sampling is used, which results in false conclusions with respect to the source location and identification.

Truncated aperture extrapolation

In conventional PNAH there are two impediments when a proper implementation of inverse near-field acoustic imaging is concerned: first, the anti-leakage and anti-signal-deterioration measures on spatial data before Discrete or Fast Fourier Transformation (DFT and FFT respectively) and, secondly, regularization of inversely propagated k-space data before inverse DFT or FFT. The focus of this chapter is on the first mentioned subject, while the latter topic is extensively discussed in (57), (45) and chapter 4.

Here, the relative simplicity, accuracy, and processing speed of FFT-based NAH is acknowledged, thus a method is introduced that makes the application of NAH possible, also outside carefully regulated surroundings on well-defined sources. The general idea is to extend the finite aperture before the FFT is applied, while ensuring minimal deterioration near the edges of the hologram, and maintaining maximum leakage reduction in k-space. This is achieved by extrapolating the finite aperture by a newly introduced method called border-padding, which is in fact a method that pads the acoustic data from the borders of the hologram outward.

This chapter is organized as follows: First, in Section 3.1, the use of windows and zero-padding in PNAH is discussed. The discrete planar inverse solution in k-space is given and the significant influence of leakage on this process is illustrated. Leakage is generally reduced by application of spatial windows (17), yet the exponential character of increasingly higher wavenumbers possibly causes problems for the inverse solution. Zero-padding the windowed hologram improves the solution of the FFT, thus resulting in an interpolated and smoothed k-space spectrum. Section 3.2 first introduces the basic border-padding operation, followed by a more thorough introduction of linear predictive border-padding. Linear predictive border-padding is based on a physical model of the measured data, written in impulse responses of a given order. These impulse responses are then fed into a Infinite Impulse Response (IIR) filter together with data at the aperture border and zero-valued extrapolation points, which results in filtered extrapolation

points that naturally fit the aperture border. Alternatively, a border-padding algorithm based on (non-physical) spline extrapolation is derived. These border-padded apertures are processed by FFT, with considerably less leakage and signal deterioration as a result. To illustrate and compare the proposed methods, the different implementations of border-padding and the basic windowing followed by zero-padding, as a reference, are compared in two numerical cases in section 3.3. Finally, some concluding remarks are given in section 3.4.

3.1 The use of windows and zero-padding in PNAH

3.1.1 two-dimensional spatial anti-leakage windows

The finite aperture of a sensor array measurement is observed spatially as a truncation window. Outside the measured aperture there exists no directly sampled knowledge of the sound field, thus the two-dimensional k-space is determined from a coarse, spatially sampled and finite aperture. The application of a window is a procedure to reduce the order of the discontinuity at the border of the periodic extension of the aperture in the FFT processing. This is realized by smoothly attenuating the data near the edges to zero. If, from another point of view, a basis set of wavenumbers for a given interval N is defined, and there exists a signal in this set with a wavenumber not exactly fitting on one of these basis wavenumbers, then, the window application transforms this signal to the basis wavenumber, which is closest to the original wavenumber of the signal. In other words, the wavenumber or k-space resolution of the spectrum is too low.

In order to illustrate these projections on a set of basis wavenumbers, an example is given. Assume a one-dimensional spatial pressure measurement with $N = 10$ samples in a finite aperture. The normalized sampling wavenumber is $k_s = 2\pi$, and the sampling interval or wavenumber resolution of $\Delta k = \frac{1}{5}\pi$. The first sine function that exactly fits one period on the basis wavenumbers is $k = \frac{1}{5}\pi$, the second one exactly fits two periods in the aperture, i.e., $k = \frac{2}{5}\pi$, and so on. Leakage is caused by processing finite aperture data, not by spatial sampling. A discontinuous edge at the aperture indicates the presence of non-fitting periodic signals, and thus causes leakage to a large number of wavenumbers. A large number of one-dimensional windows, suitable for harmonic analysis, are discussed in (17), which are also applicable to two-dimensional spatial aperture processing. Unlike digital audio processing and spectral analysis, which often includes many thousands of samples, acoustic array measurements generally exhibit several tens of sensors in one direction at most. This means only coarse aperture data is available, which requires a careful process to determine the proper k-space with as much preserved spatial information as possible. Often, this implies a trade-off between k-space leakage and loss of acoustic information, especially near the edges of the aperture. A good compromise is

often made by the application of a Tukey window (17), which is defined as:

$$w(n) = \begin{cases} \frac{1}{2}\left[1 + \cos\left(\frac{2\pi}{\alpha}\frac{(n-1)}{(N-1)} - \pi\right)\right], & n < \frac{\alpha}{2}(N-1) + 1, \\ 1, & \frac{\alpha}{2}(N-1) + 1 \leq n \leq N - \frac{\alpha}{2}(N-1), \\ \frac{1}{2}\left[1 + \cos\left(\frac{2\pi}{\alpha} - \frac{2\pi}{\alpha}\frac{(n-1)}{(N-1)} - \pi\right)\right], & N - \frac{\alpha}{2}(N-1) < n, \end{cases} \quad (3.1)$$

where $n = 1$ to N and α between 0 and 1. In the lower limit of $\alpha = 0$ the Tukey window equals the rectangular window, while it evolves to the Hanning window as α increases to become $\alpha = 1$. In between these extremes, the Tukey window is a combination of a cosine tapering near the edges and a non-attenuated area near the center of the aperture. Application of this window is a compromise between attenuation of acoustic data near the aperture border and the amount of leakage in k-space. The two-dimensional Tukey window follows from the transpose vector of the window from (4.2) in y-direction multiplied with the row vector of the window in the x-direction:

$$w(n, m) = w(m)^T * w(n). \quad (3.2)$$

In Figure 3.1, a comparison is made between a number of settings for α in the Tukey window, including the rectangular and Hanning window settings, to determine the influence of leakage on the inverse process of PNAH. From Figure 3.1, it is clear that decreasing α causes the leakage sidelobes to become higher. When the exponential inverse propagation curve for k-space is multiplied with the window transform, the threat of leakage becomes visible, since the sidelobes are attenuated by the inverse propagator.

Window compensation after the complete inverse propagation process is an option, yet, due to the applied window, the wavenumbers have shifted and results near the edges are heavily affected. The inverse propagation and the discrimination of strengths between individual wavenumber bins is too varied to compensate with an inverse window. A promising alternative is to pre-process the data before the FFT is applied.

3.1.2 zero-padding

By zero-padding it is possible to interpolate between the basis wavenumbers within the spectrum. If a finite aperture is considered, with edge values and all orders of the derivative near the edge equal to zero, and an FFT is applied on the spatially sampled data, then the resulting k-space spectrum is free of spectral leakage as discussed in the previous section. However, due to the finite number of sampling points in this perfect aperture, only a discrete number of wavenumber bins are available to map the data on. The discrete k-space is only a representation or mapping of the continuous spectrum on the set of basis wavenumbers. Wavenumbers present in the spatial data remain hidden in k-space if their periods do not exactly match the discrete wavenumbers. This finite resolution in k-space is due to the finite length of the spatial aperture, which is visible in the DFT of

(a) Tukey windows applied to the signal (left) and the FFT result in k-space (right)

(b) inverse propagator in k-space applied to the k-space data (left) and the resulting signal at $z_s = 0$
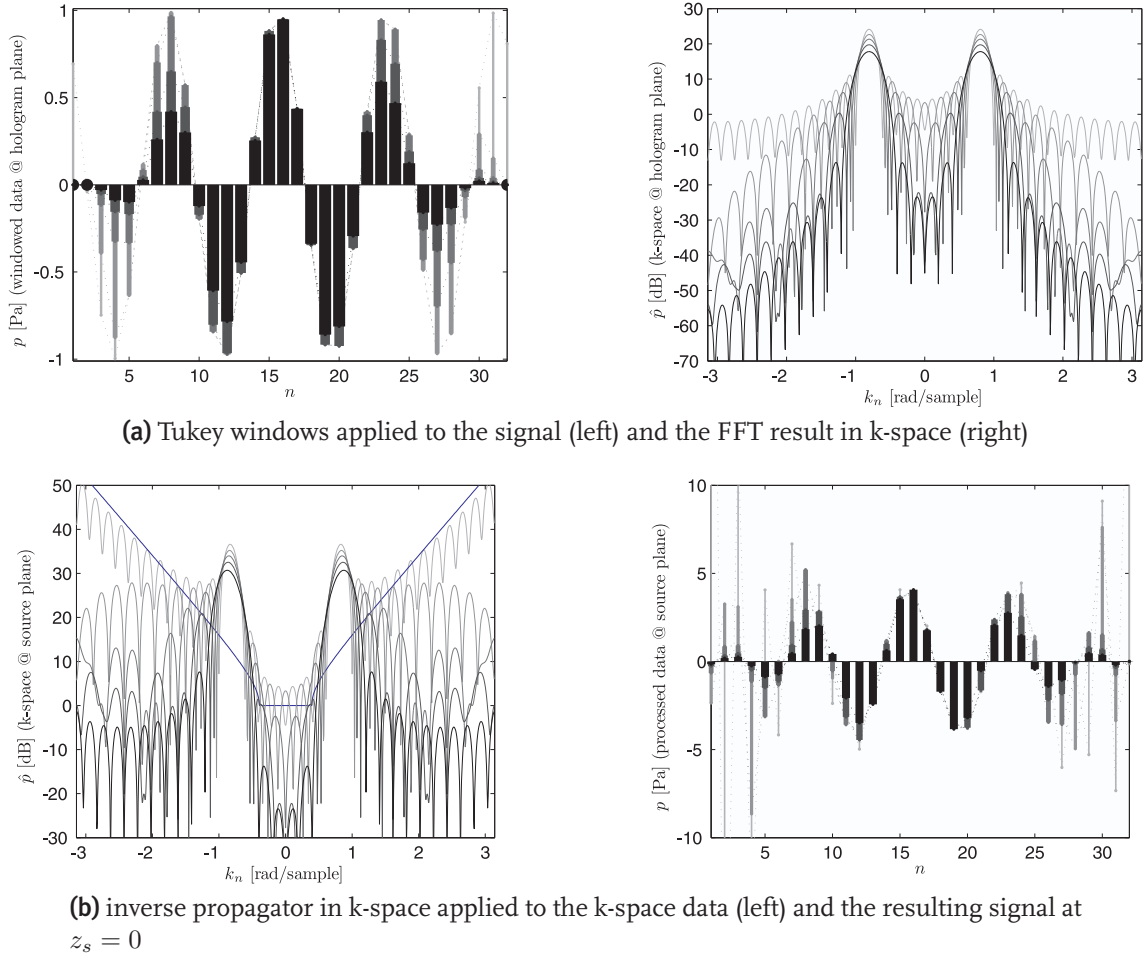
Figure 3.1: signal leakage and influence on spatial data due to Tukey windowing with $\alpha = 0, 0.25, ..., 1$ (ranging from light to dark grey respectively) on a cosine with $k_n = \frac{8.2}{N}\pi$ at $z_h = 0.02$ m sampled at $N = 32$ points with 0.01 m spacing in between and a radiation wavenumber at $k_r = \frac{1}{4}\pi$

such an aperture.

If the spatial aperture is increased while padding the new samples with zero value, the solution power of the DFT increases, resulting in an optimal interpolation in k-space. Now, a larger number of wavenumbers is distinguished in the spectrum. Every single bin increase above the aperture size increases the number of bins in k-space: $\Delta k = \frac{2\pi}{N+v}, v = 0, 1, 2, \cdots$. In order to maintain the original wavenumber bins, the aperture size is expanded by an integer number of the original aperture size: $\Delta k = \frac{2\pi}{wN}, w = 1, 2, 3, \cdots$. Zero-padding does not increase spectral resolution in k-space.

Another practical consideration for zero-padding is the calculation speed advantage that is accomplished by expanding the total number of samples in either direction to a power of two, resulting in $N \log N$ operations (3). Careful investigation of the characteristics of windowing and zero-padding leads to the development of border-padding, which includes the good characteristics of these methods, and largely discards the negative aspects.

3.2 Truncated aperture expansion

3.2.1 border-padding

The main idea of border-padding is to keep the original aperture intact and use the information at the border to pad or extrapolate unknown data outward. Due to the above-described windowing methods, a significant part of the edges of the data get affected and large errors are introduced. In practise, when using these windowing methods, it is necessary to enlarge the measured aperture and make sure the interesting sources are not situated near the border. An alternative to windowing is the application of a direct method without using the Fourier transform, like SONAH (49), HELS (54), or ESM (51). Border-padding deals with these problems as follows. Instead of padding the added samples with zeros, the values of the samples at the edge or border of the signal are padded, filling up the added samples. After spatial extrapolation, a spatial window on the complete set of data, including the border-padded part, is applied. The Tukey window is especially fitted for this purpose since the constant part of the window is placed exactly over the original aperture, while the cosine-tapered part covers the border-padded region. In this way, the spatial window does not affect the acoustic information and leakage will be reduced as well. This one-dimensional operation is expressed as

$$
\tilde{p}_b(n_b) = \begin{cases} \frac{1}{2}\tilde{p}(1)\left[1 + \cos(2\pi\frac{(n_b-1)}{(\frac{N_b-N}{2}-1)} - \pi)\right], & n_b \leq \frac{N_b-N}{2}, \\ \tilde{p}(n), & \frac{N_b-N}{2} < n_b \leq N_b - \frac{N_b-N}{2}, \\ \frac{1}{2}\tilde{p}(N)\left[1 + \cos(\pi - 2\pi\frac{(n_b-1)}{(\frac{N_b-N}{2}-1)})\right], & n_b > N_b - \frac{N_b-N}{2}, \end{cases} \tag{3.3}
$$

where $\tilde{p}_b(n_b)$ is the border-padded aperture, for $n_b = 1, ..., N_b$ with N_b the border-padding length. The fully border-padded aperture includes the original aperture $\tilde{p}(n)$, which is placed in the center of the border-padded aperture, with $n = 1, ..., N$ and $N_b > N$. The two-dimensional aperture is naturally border-padded by first applying (3.3) to every row, followed by the resulting columns, or vice versa.

Still, this form of border-padding causes leakage, which is due to the used Tukey window and the cross-over area between aperture and padded area where the first derivative function is often discontinuous. Especially a discontinuous derivative at the border introduces errors near this point, leaking back into the original aperture, and thus causing errors in the determined acoustic source strengths and shapes.

3.2.2 linear predictive border-padding

Linear predictive filtering is a method that extrapolates a signal outside the known area by an approximation based on a chosen number of previous samples. For a finite spatial aperture, first, one row or column of data is used to calculate the impulse response

coefficients. Secondly, a digital filter is initialized by the impulse response coefficient. Finally, a zero-valued vector is fed into the filter which spans the eventual border-padded width to this side of the aperture. Both ends of the finite aperture are extrapolated by this procedure. After every row or column is padded, the same sequence is applied in the other direction, including the border-padded parts. This results in a fully border-padded hologram, which is fit for two-dimensional FFT. To make sure no leakage from the outer edges is generated, a wide Tukey window is applied that applies a cosine tapering far from the measured hologram, thus leaving the measurement data unchanged.

linear predictive filter

Take a measured acoustic pressure series $\tilde{p}(x_n)$ over a single line of the holographic aperture, which is N samples in size and situated in a source-free half-space. The vector $\tilde{\mathbf{p}}(x_n) = [\tilde{p}(x_1), \tilde{p}(x_2), \tilde{p}(x_3), \dots, \tilde{p}(x_N)]$ is expanded outside this interval, creating border-padded samples to the right or to the left of the aperture, $[\tilde{p}(x_{N+1}), \tilde{p}(x_{N+2}), \tilde{p}(x_{N+3}), \dots]$ and $[\dots, \tilde{p}(x_{-2}), \tilde{p}(x_{-1}), \tilde{p}(x_0)]$ respectively. Ideally, a number of prediction filter coefficients predicts these samples perfectly, i.e., with zero prediction error, based on Q previous samples. The newly acquired sample is denoted as $p(x_s)$, a linear description of such a filter is written as

$$\tilde{p}(x_s) = \sum_{i=1}^{Q} h_i \tilde{p}(x_{s-i}), \tag{3.4}$$

where h_i are the prediction filter coefficients.
The measured, noisy data used for practical NAH is far from perfect, and the analytical solution for $\mathbf{h}$ ($h_{-\infty} \dots h_{\infty}$) only exists in theory. The real world requires an iterative method based on the determination of a linear prediction error coefficients, $\mathbf{a} = [1, a_1, a_2, \dots, a_v]$, which are converted to impulse response coefficients by

$$\mathbf{h} = [h_1, h_2, \dots, h_Q] = [-a_1, -a_2, \dots, -a_v]. \tag{3.5}$$

Several methods exist to determine a fitting model to the signal, yet, the Burg method (2) is both minimum-phase (i.e., all roots of the corresponding transfer function polynomials of the filter remain within the unit circle in the complex plane), and suitable for few observed samples (which is often the case in NAH measurements). The Burg method was initially introduced for estimating power density spectra of stationary time series, and provides good practical results in digital time series audio processing and extrapolation (23; 19). Additionally, the spatial domain is a viable area for implemen-

tation, since time-frequency processing is in many respects correspondent to space-wavenumber processing. The Burg method is used to fit an autoregressive model (AR) on $\tilde{p}(x_n), n = 1, 2, \cdots N$, which is then used in the implementation of the filter.

physical basis for spatial domain

Before the actual implementation of border-padding by means of a linear prediction filter is discussed, the viability of this procedure with respect to spatial acoustic fields is assessed here.

Generally, in NAH, an unknown, steady state pressure distribution $\tilde{p}(x, y, z)$ in a source-free half-space, $z > 0$, is considered. In (56), it is shown that this pressure in k-space $\hat{\tilde{p}}(k_x, k_y, z)$ is completely and uniquely expressed by a sum of planar and evanescent waves, or a sum of cosines as a function of wavenumbers k_x and k_y, as

$$\hat{\tilde{p}}(k_x, k_y, z) = \sum_{k_x} \sum_{k_y} \hat{\tilde{p}}(k_x, k_y) e^{j(k_x x + k_y y + k_z z)}. \tag{3.6}$$

A plane wave in the x-direction can be described by a cosine function, which is a superposition of two phasors according to Euler's formula:

$$\cos k_x x = \frac{e^{jk_x x} + e^{-jk_x x}}{2}. \tag{3.7}$$

The wavenumber spectrum of this cosine, which is represented by two phasors, is represented by two Dirac delta functions. For extrapolation of this cosine function two impulse response coefficients are required. A single phasor is naturally extrapolated by

$$e^{jk_x n\Delta x} = h_1 e^{jk_x (n-1)\Delta x}, \quad with \ h_1 = e^{jk_x \Delta x}, \tag{3.8}$$

and the cosine extrapolation is a sum of two phasors:

$$\begin{aligned} cos(k_x n\Delta x) = \ & h_1 \frac{e^{jk_x(n-1)\Delta x} + e^{-jk_x(n-1)\Delta x}}{2} \\ & + \ h_2 \frac{e^{jk_x(n-2)\Delta x} + e^{-jk_x(n-2)\Delta x}}{2}, \end{aligned} \tag{3.9}$$

with $h_1 = 2\cos(k_x \Delta x)$ and $h_2 = -1$. From (56) and the above descriptions, it follows that the discrete acoustic spatial information at the hologram plane is Fourier transformable and completely and uniquely represented by a finite sum of impulse responses.

implementation

The general form difference function for a direct form IIR filter (32) is defined for spatial sound pressure as

$$\sum_{i=0}^{v} a_i \tilde{p}_b(x_{s-i}) = \sum_{i=0}^{w} b_i \tilde{p}(x_{s-i}),$$
(3.10)

where a_i and b_i represent the filter coefficients, which are part of the coefficient vectors with lengths $v+1$ and $w+1$ respectively, $\tilde{p}_b(x_s)$ is the unknown sound pressure outside the aperture, and $\tilde{p}(x_s)$ the initializing value that serves as input to the IIR filter. The direct form II realization of this filter is illustrated in Figure 3.2.
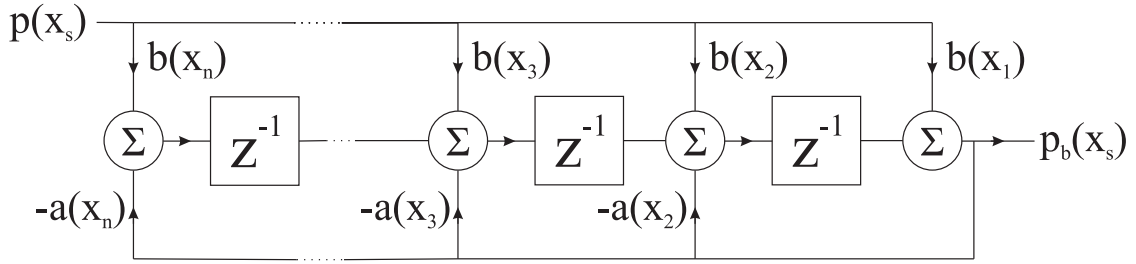
Figure 3.2: infinite impulse response filter direct form II realization, $p(x_s)$ is the unknown pressure one sample outside the original aperture and $p_b(x_s)$ the border-padded prediction of the pressure on this position

The initial value is $\tilde{p}(x_s) = 0$ for all s, thus the output in (3.10) becomes

$$\tilde{p}_b(x_s) = -\frac{1}{a_0} \sum_{i=1}^{v} b_i \tilde{p}_b(x_{s-i}).$$
(3.11)

This implementation for the IIR filter based interpolation equals the convolution product from (3.4), when $a_0 = 1$, $a_i = -h_i$, $b_i = 1$ and $w = 0$, and results in the final IIR difference equation:

$$\tilde{p}_b(x_s) = \sum_{i=1}^{v} b_i \tilde{p}_b(x_{s-i}) + \tilde{p}(x_s).$$
(3.12)

The filter order is bounded by the number of available samples in the finite aperture, yet the choice of the optimal order is not entirely straight forward. The presence of high

wavenumbers in the aperture data requires a higher order description, yet also noise is present at these higher wavenumbers, which potentially causes problems for the inverse solution of a finite, discrete aperture. The k-space low-pass filter is also of influence, since an applied filter with a significantly lower cut-off than half the sampling wavenumber already lowers the relevant order of the linear predictive filter.
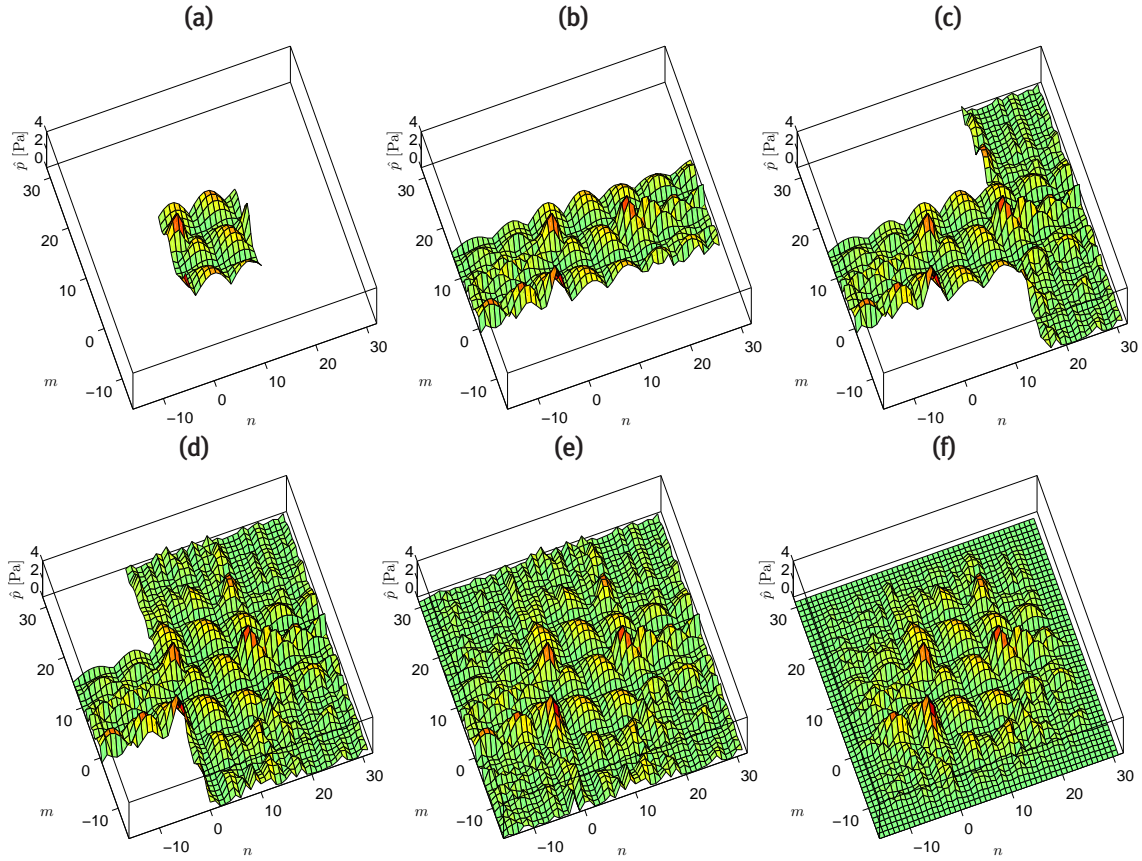
Figure 3.3: border-padding a truncated holographic aperture in two dimensions: start with the original aperture (a), followed by x-direction expansion (b), y-direction expansion (c&d), resulting in a fully padded aperture (e) and finalized by a spatial window (f)

The implementation provided above extrapolates only one row to the right of a hologram aperture, thus an extended, two-dimensional implementation is required. First, the two-dimensional hologram measurement data $\tilde{p}_h(x_n, y_m)$ is border-padded in the positive and negative x-direction, as illustrated in Figure 3.3a. Subsequently, the partly border-padded data is extrapolated in the positive and negative y-direction, also including the previously non-existing, border-padded parts. The illustrations from Figures 3.3b to 3.3e show that this process fills up a full array of data, consisting of originally measured signals and fully border-padded data around it.

From windowing theory, it is clear that data near the edges of the extended aperture should go to zero for a number of derivatives. This is also the case for border-padded

data, and thus a certain type of windowing or tapering is required. There are two clear options for border-padding: the first option is the application of a standard type window and, secondly, the connection of the negative with the positive aperture end of the data. The implemented version discussed in this work includes a 2D Tukey window, with a cosine tapering applied to one-third of the extrapolated data, as shown in Figure 3.3f.

3.3 Numerical analysis of border-padding

3.3.1 source reconstruction errors
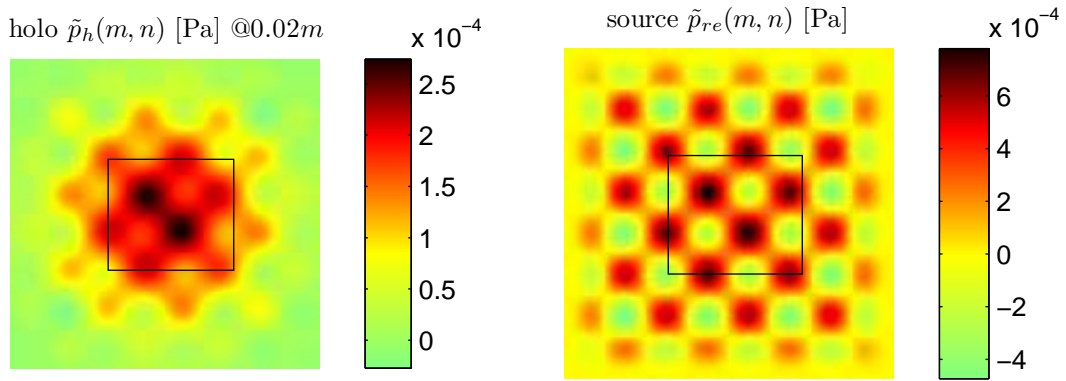
(a) modal source hologram plane (left) at 0.02 m away from the source plane (right)
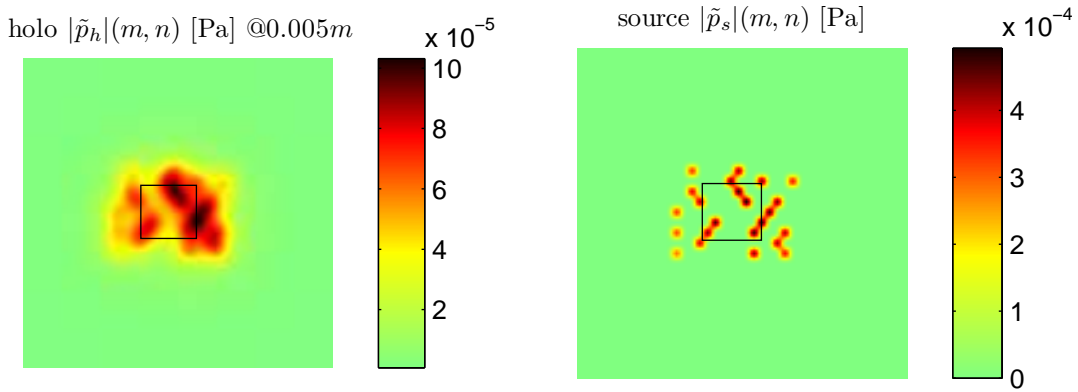
(b) point source hologram plane (left) at 0.005 m away from the source plane (right) with a total of 23 in-phase point sources

Figure 3.4: modal source (a) with a combined 1×1 and 8×8 mode, the height and width of the aperture measures 0.3 m with 128 spatial samples at a sound frequency of $f = 1$ kHz; random pattern of point sources (b), the height and width of the aperture measures 0.3 m with 128 spatial samples at a sound frequency of $f = 1$ kHz

In a numerical analysis on extrapolation of a limited aperture for an inverse method, con-

sideration of a wide wavenumber band is useful. Naturally, discussion of modal wave-forms is relevant, yet, considering point sources or sharp edges in the hologram provides more information on the quality of inverse data-processing methods. The point sources contain energy over a broader k-space band, which causes more problems for the FFT. Therefore, not only modal or sine-shaped sources are considered in this numerical analysis, but also point sources. Influence of noise is not considered here, since purely the influence of windowing or extrapolation is investigated. The two full-sized apertures for the numerical analysis are shown in Figure 3.4a and Figure 3.4b.

In order to test windowing and border-padding, a small portion of a large hologram aperture is selected. The small selection is then border-padded and both holograms are inversely propagated to the source. The border-padded inverse is truncated and compared with a selection of the fully inverse calculated source, which corresponds to the selected area. These results provide much insight into the quality of the method. Besides this qualitative comparison, a quantitative measure is calculated in the form of a root mean squared reconstruction error (RMSRE):

$$RMSRE = 100\% \cdot \sqrt{\frac{1}{MN} \sum_{n=1}^{N} \sum_{m=1}^{M} \frac{(|\tilde{p}_{ex}(m,n)| - |\tilde{p}_{re}(m,n)|)^2}{|\tilde{p}_{ex}(m,n)|^2}}, \qquad (3.13)$$

where $\tilde{p}_{ex}(m,n)$ is the exact pressure on the source, and $\tilde{p}_{re}(m,n)$ is the reconstructed pressure over the selected small aperture.

Different padding areas are illustrated in Figure 3.5 and Figure 3.6 for three types of border-padding and basic spatial windowing. The third border-padding form is based on cubic spline extrapolation, which is implemented as a (non-physical) reference to the linear predictive extrapolation. Here, a number of piecewise polynomials based on the measured data are determined to extrapolate the field with. The selected finite aperture is marked by the rectangle in the hologram images. Two different filter orders are used to illustrate the influence of the order in linear prediction border-padding. For every case, the left-most image is the hologram generated by the extrapolation method, which is easily compared to the exact holograms in Figure 3.5 and Figure 3.6. The center image is the exact solution and the right-most image is the resulting solution at the source for the extrapolated case.

From the results of the modal case it is clear that linear predictive border-padding out-performs the other three methods. The windowed case shows, as expected, very high quantitative as well as qualitative errors, introducing higher wavenumbers near the aperture edge due to the window slope. The field near the aperture edge in Figure 3.5.1 is over-estimated, since the higher wavenumbers are amplified more by the inverse propagator than the original modal content. Both the basic (Figure 3.5.2) and spline (Figure 3.5.5) border-padding show equal results, which are far better than the windowed version, both in RMSRE and qualitatively. However, the linear predictive border-padding results both show an optically flawless comparison to the exact source distribution (Fig-

1) windowing & zero-padding: hologram, exact source and result: RMSRE=1.5%

2) basic border-padding: hologram, exact source and result: RMSRE=0.1%

3) order 4 lin. pred. border-padding: hologram, exact source and result: RMSRE=0%

4) order 15 lin. pred. border-padding: hologram, exact source and result: RMSRE=0%

5) spline border-padding: hologram, exact source and result: RMSRE=0.1%
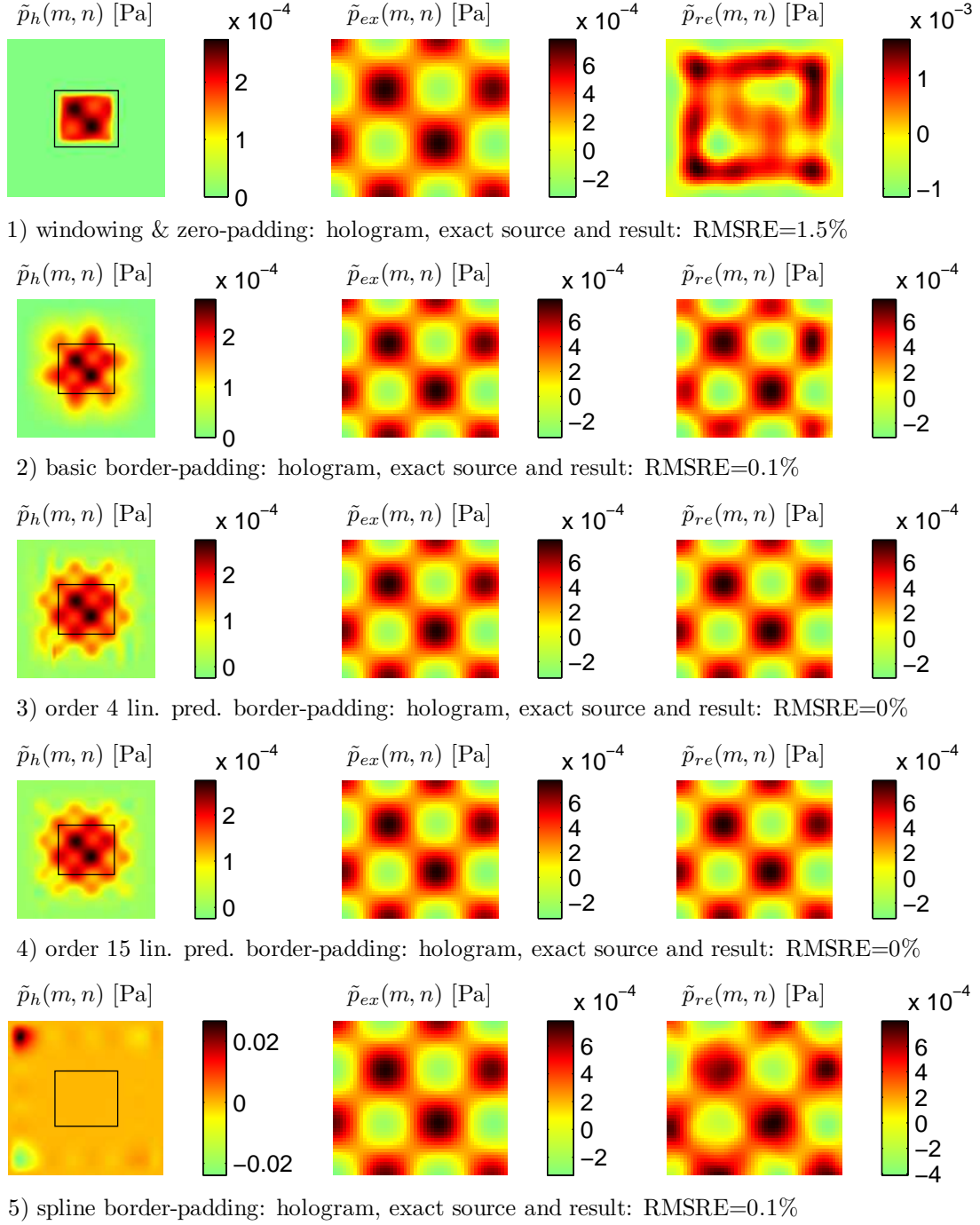
Figure 3.5: results of five types of data extrapolation in combination with PNAH processing for the modal source under test

ure 3.5.3 and 3.5.4), while the RMSREs are between one and two percent.

For the point sources case, the difference between linear predictive border-padding and the other three methods increases drastically. The windowed (Figure 3.6.1), basic border-padded (Figure 3.6.2) and spline border-padding (Figure 3.6.5) reconstructions of the

1) windowing & zero-padding: hologram, exact source and result: RMSRE=2548.1%

2) basic border-padding: hologram, exact source and result: RMSRE=186.9%

3) order 4 lin. pred. border-padding: hologram, exact source and result: RMSRE=9.5%

4) order 15 lin. pred. border-padding: hologram, exact source and result: RMSRE=20.6%

5) spline border-padding: hologram, exact source and result: RMSRE=4141.2%
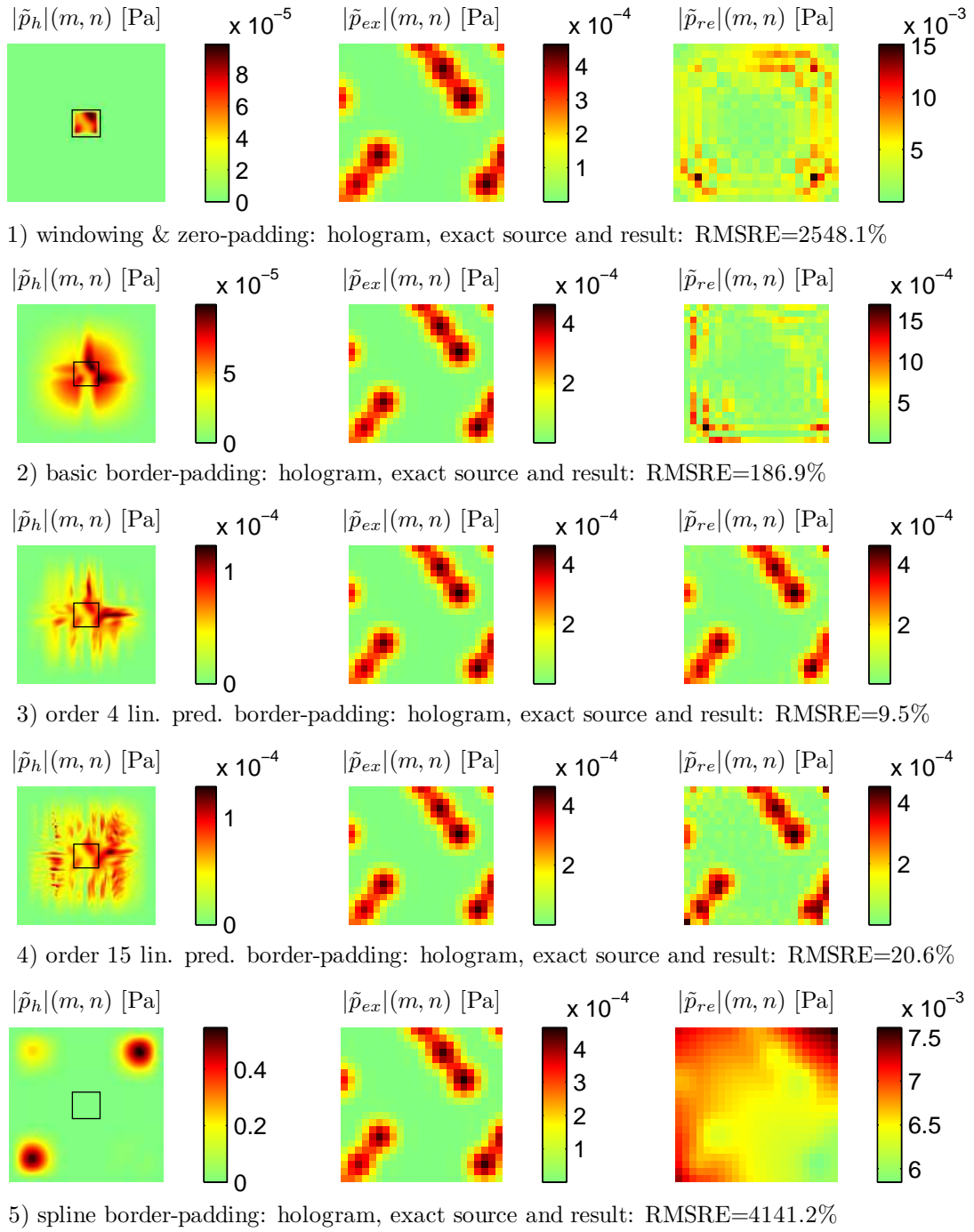
Figure 3.6: results of five types of data extrapolation in combination with PNAH processing for the point sources under test

source pattern are unrecognizable and also quantitatively incorrect. Although basic border-padding results in a fair RMSRE, the large errors near the aperture edges are not satisfying. The difference between the low and higher order linear predictive border-padding is interesting in comparison with the modal case. Order 4 linear predictive

border-padding in Figure 3.6.3 is clearly better, both qualitatively and quantitatively, compared to order 15 linear predictive border-padding in Figure 3.6.4.

From the above, it is clear that the point sources case is much more challenging for the finite aperture extrapolation algorithms. The linear predictive border-padding is the only tested method capable of handling both cases well. One drawback of the higher order algorithm, compared to a lower order one, is the increased processing time. Also, higher order border-padding, for cases with high wavenumber content, possibly causes numerical errors due to the finite and discrete character of the data. This behavior is not exactly clear, yet errors occur when data consisting of high wavenumbers close to the Nyquist wavenumber are processed with a high order of the linear predictive filter. The next section discusses the trade-off between processing speed, RMSRE and order.

3.3.2   comparison of processing speeds

Besides accuracy considerations, another important factor is processing speed. Especially in situations where large numbers of frequencies are processed, or in-stationary sources are observed with an array. In these cases, many different spatial apertures are required to determine inverse solutions from. Thus, limiting the processing time of the border-padding algorithm is necessary.

In order to illustrate the processing speed in comparison with the accuracy, a range of linear predictive border-padding applications varying in order from 1 to 20 are applied to the modal and point sources introduced in the previous section. The processing speed test for the linear predictive border-padding algorithm is implemented in a $Matlab^{\text{TM}}$ 7 environment on an average speed PC system (Pentium IV 2.8 GHz, with 1 GByte of memory).

From the results for the modal sources in Figure 3.7a and 3.8a it is clear that the order has a small influence on the error from order 5 onwards. However, the speed linearly increases as we improve the order. For the modal case an order 5 linear predictive filter would suffice. When observing the results for the point sources in Figure 3.7b and 3.8b, it shows minimum errors between order 4 and 10. The processing speed of the practicable order between order 4 and 10 is hardly an issue, since this average system shows speeds of a few tens of a second for a full 16.384 point aperture.

3.4   Discussion

Border-padding is a fast, efficient and accurate extrapolation method that adds practical relevance to the standard NAH methods based on k-space inverse propagation of the sound-field. The strategy to pre-process the spatial acoustic data before the FFT is applied is robust and minimizes leakage and distortion of the acoustic field. By decoupling

(a)

O1 $\tilde{p}_{re}$ [Pa]   ×10⁻⁴   O2 $\tilde{p}_{re}$ [Pa]   ×10⁻⁴   O3 $\tilde{p}_{re}$ [Pa]   ×10⁻⁴   O4 $\tilde{p}_{re}$ [Pa]   ×10⁻⁴

RMSRE: 19.9%   RMSRE: 11.2%   RMSRE: 3.2%   RMSRE: 1.8%

O5 $\tilde{p}_{re}$ [Pa]   ×10⁻⁴   O10 $\tilde{p}_{re}$ [Pa]   ×10⁻⁴   O15 $\tilde{p}_{re}$ [Pa]   ×10⁻⁴   O20 $\tilde{p}_{re}$ [Pa]   ×10⁻⁴

RMSRE: 1.2%   RMSRE: 1.2%   RMSRE: 1.1%   RMSRE: 1.1%

(b)

O1 $|\tilde{p}_{re}|$ [Pa]   ×10⁻⁴   O2 $|\tilde{p}_{re}|$ [Pa]   ×10⁻⁴   O3 $|\tilde{p}_{re}|$ [Pa]   ×10⁻⁴   O4 $|\tilde{p}_{re}|$ [Pa]   ×10⁻⁴

RMSRE: 199.6%   RMSRE: 47.4%   RMSRE: 18.1%   RMSRE: 9.5%

O5 $|\tilde{p}_{re}|$ [Pa]   ×10⁻⁴   O10 $|\tilde{p}_{re}|$ [Pa]   ×10⁻⁴   O15 $|\tilde{p}_{re}|$ [Pa]   ×10⁻⁴   O20 $|\tilde{p}_{re}|$ [Pa]   ×10⁻⁴

RMSRE: 8.5%   RMSRE: 10.5%   RMSRE: 20.6%   RMSRE: 30.7%
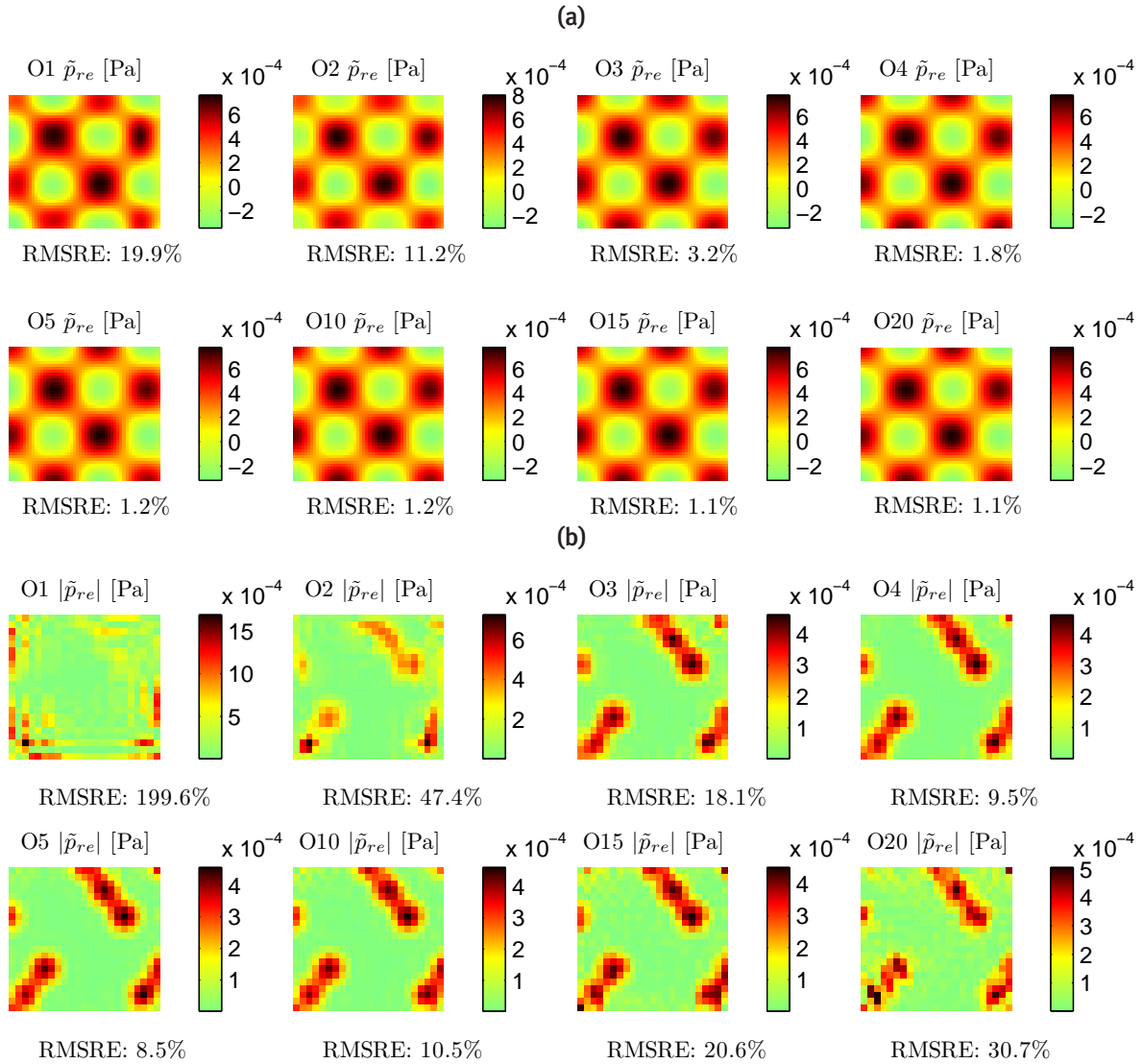
Figure 3.7: influence of linear predictive border-padding order on resulting error of the modal (a) and the point sources (b) case, both after PNAH

the spatial pre-processing from inverse propagation and regularization, a highly versatile method, without any pre-knowledge of noise color and variance, results. The use of measured data to form a physically relevant filter implementation to extrapolate the finite aperture shows great improvements compared to standard windowing and other forms of data extrapolation.

The numerical experiments on the modal source show very good results for filter orders of 5 and higher, yet the lower orders still show reasonably good results in comparison with basic border-padding, windowing and spline extrapolation. The numerical point sources case shows equal results for low orders, although for high orders the RMSRE is steadily increasing, also resulting in qualitatively decreasing results. In a practical situation, where sources are unknown, a filter order between orders 5 and 10 suffices. Also,
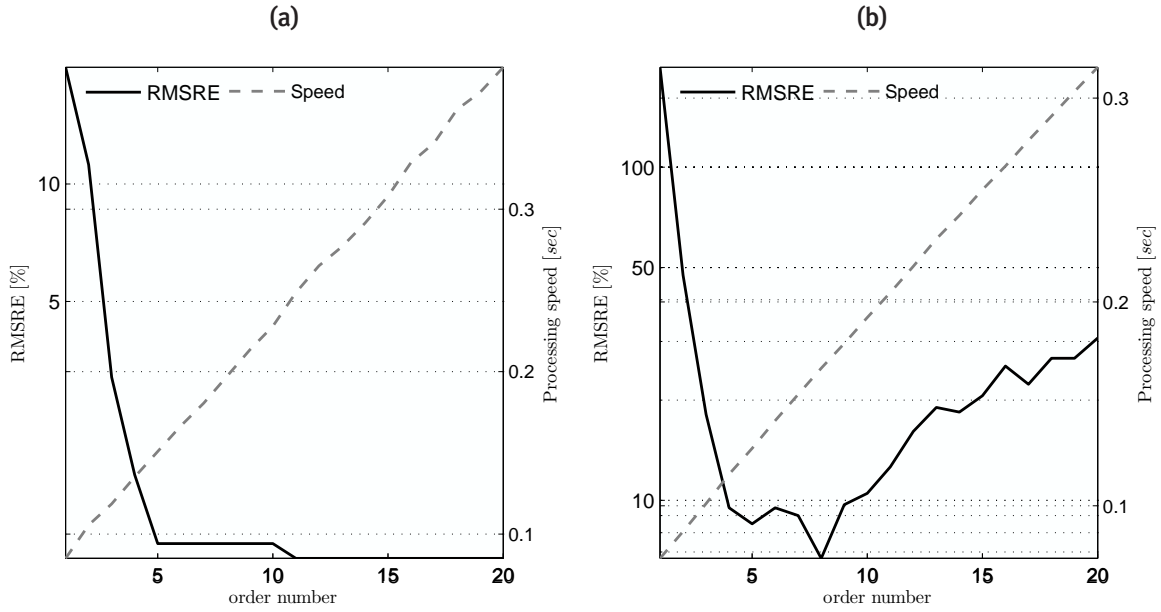
Figure 3.8: processing speed and error versus border-padding order for the modal (a) and point sources (b) case after linear predictive border-padding and PNAH

in the presence of noise in the actual measured cases, it is shown that border-padding is a well-applicable method in real-life cases.

Besides extrapolation of the aperture edges outward, border-padding is also applicable to fill gaps in the hologram aperture. This allows the use of several patches along the area of interest without equidistant rectangular measurement grids, since border-padding permits coupling of the separate patches to form a rectangular grid.

The applied algorithm first treats the data in one dimension completely, followed by the other dimension, which probably results in sharp edges and thus high wavenumbers. This possibly poses a problem when the border-padded aperture is inversely propagated, yet this phenomenon only emerges relatively far away from the measured aperture, not causing any problems in the truncated result. Yet, a fully two-dimensional method could further increase the possibilities of border-padding.

Near-field Wavenumber Regularization

4.1 Introduction

Evanescent acoustic waves attenuate with an exponential power as a function of the distance from the sound source. One of the major problems with the corresponding inverse solutions from a near-field acoustic hologram is their ill-posedness, primarily caused by noise in the measurements. Noise tends to blow up in the inverse solution, resulting in highly inaccurate sound source information. Over the years, many books and articles (15; 31) have discussed a wide variety of methods to regularize ill-posed inverse problems and minimize the errors due to noise, yet remaining at an acceptable level of accuracy of the acoustic image.

This chapter introduces a modified exponential and modified Tikhonov low-pass k-space filters, and compares improvements on computational efficiency, insights and accuracy of a number of regularization methods discussed in recent publications (31; 57). The focus lies on (low-pass) filter functions and stopping rules for parameter selection, specifically applicable in the wavenumber domain or k-space. This point of view provides a number of interesting insights into the importance of measurement conditions and set-up parameters.

The chapter is organized as follows: Regularization in k-space is split into two parts: low-pass filter functions and stopping rules for selection of low-pass filter parameters. Low-pass filters for k-space are discussed in Section 4.2; herein, the newly developed modified exponential and modified Tikhonov filters are introduced, also the widely used classical exponential filter, Tikhonov and the truncation low-pass filter are discussed. In Section 4.3 the L-curve criterion and Generalized Cross-validation (GCV) stopping rules are adapted specifically for k-space application. Also, the newly developed automated and accurate Cut-Off and Slope (COS) iteration for k-space is introduced. All possible

combinations of filter functions with the three discussed stopping rules are applied and compared in section 4.4, using simulations with different types of realistic sound sources for holographic input.

4.2 Low-pass Filter Functions

A well-known issue with inverse problems is the blow-up of noise after processing the inverse solution of the measured data, this is an example of an ill-posed problem. Ill-posed problem studies go back as far as the first quarter of last century (9), while more recently discrete ill-posed problems were broadly discussed by Hansen (15). This work will not attempt to cover the topics of discrete ill-posed problems and regularization in detail, yet it will make use of previous work in order to split up regularization procedures for near-field acoustic holography in filter functions and stopping rules. The filter functions and stopping rules are specifically derived and defined for k-space processing in order to speed up the process. Modified versions of both the exponential and Tikhonov filter are introduced that are specifically applicable for NAH problems. Complementary to the modified filter types, three main type low-pass filters, namely the exponential, Tikhonov and truncation filter, are discussed in this section. Also, consequences of the selection of extremely steep and smooth sloped filters are shown.

4.2.1 Modified Exponential filter

A way to discriminate between high wavenumbers polluted with noise, and useful information at somewhat lower evanescent and propagating waves, is to apply a low-pass, cosine tapered filter. The cut-off wavenumber k_{co} determines the characteristic point in k-space where the low-pass filter has dropped in magnitude by half. The slope that connects the all-stop and all-pass regions of the filter function can be defined in various ways. The attenuation of propagating waves is countered by a new filter function, which is a modified version of the general form exponential filter, which is given below. A modified version of the exponential filter takes the $k_{xy} = k_r$ limit into account, which means no propagating data within the radiation circle is altered. Below $k_{xy} = k_r$, waves are propagating in nature and remain unaltered in magnitude by the inverse procedure, thus there exists no possibility of noise blow-up, and therefore the low-pass filter will only introduce unnecessary errors if the taper starts in this area. Only wavenumbers at $k_{xy} > k_r$ are interesting in terms of spatial resolution improvements, however, they also cause noise blow-up problems. The new definition of the modified exponential filter makes it impossible to alter propagating waves, while the cut-off and slope are easily and independently

modified. The modified exponential filter is defined by

$$
H_f^{k_{co},\phi} = \begin{cases} 1, & k_{xy} < k_{co} - k_{ev}\phi, \\ \frac{1}{2} + \frac{1}{2}\cos\left(\frac{k_{xy}-(k_{co}-k_{ev}\phi)}{2k_{ev}\phi}\pi\right), \\ & k_{co} - k_{ev}\phi \leq k_{xy} \leq k_{co} + k_{ev}\phi, \\ 0, & k_{xy} > k_{co} + k_{ev}\phi, \end{cases} \tag{4.1}
$$

where $k_{ev} = k_{co} - k_r$ (> 0) is the useful evanescent k-space content and ϕ the taper ratio between 0 and 1. At $\phi = 0$, the filter slope is infinitely steep, equal to a truncation filter that is discussed below. With increasing ϕ, the slope becomes less steep, and with $\phi = 1$, the slope is zero. From $k_{xy} = 0$ up to at least $k_{xy} = k_r$, the filter passes all energy. The area directly outside the radiation circle up to $k_{xy} = k_{co}$, and the ϕ dependent tapering area outside determine the height of the spatial resolution improvement of NAH compared to beam-forming. Outside this region, the data is flawed with measurement and numerical noise.

The differences between the modified and the general form exponential filter function are easily observed by comparison of (4.1) with the general form exponential filter (1), which is defined by

$$
H_f^{k_{co},\gamma} = \begin{cases} 1 - \frac{1}{2}e^{-(1-k_{xy}/k_{co})/\gamma}, & 0 < k_{xy} < k_{co}, \\ \frac{1}{2}e^{(1-k_{xy}/k_{co})/\gamma}, & k_{xy} \geq k_{co}, \end{cases} \tag{4.2}
$$

where the slope is determined by the chosen factor γ. Although this is an elegant definition of an exponential low-pass filter, there is an important drawback for its utilization in NAH: It is possible to choose a γ that will cause propagating waves to get filtered out at low values of k_{co}. It remains questionable if a minor attenuation influences the resulting error of the full inverse process, but it is important to describe and investigate possible consequences.

4.2.2 Modified Tikhonov filter

Tikhonov regularization is a widely discussed statistical method, also known as ridge regression, which was developed by Phillips (33) and Tikhonov (50) in the same period, yet independently of one another. Equal to the exponential filter, the result after Tikhonov regularization is also a low-pass k-space filter, which will become clear from the following. To derive the low-pass Tikhonov filter function in its general form for a sound pressure hologram and desired sound pressure at the source plane, the forward problem is written as (57)

$$
\tilde{p}_h = \mathbf{F}^{-1}\mathbf{G}\mathbf{F}\tilde{p}_s. \tag{4.3}
$$

Notice that $\tilde{p}_h$ and $\tilde{p}_s$ represent the spatial sound pressure information at the hologram plane and source plane respectively, written in vector form. The discrete spatial Fourier

transforms are represented by the matrix operators $\mathbf{F}$ and $\mathbf{F}^{-1}$, the inverse of $\mathbf{F}$, while $\mathbf{G}$ is a diagonal matrix containing the forward propagators for the pressure to pressure problem. The standard Tikhonov minimization for the forward problem is written as

$$\min\{\|\mathbf{Q}\tilde{p}_s - \tilde{p}_h\|_2^2 + \lambda^2\|L\tilde{p}_s\|_2^2\}, \tag{4.4}$$

with λ the regularization parameter, L the Tikhonov filter weight function and

$$\mathbf{Q} = \mathbf{F}^{-1}\mathbf{G}\mathbf{F}. \tag{4.5}$$

The regularized solution for $\tilde{p}_{s,\lambda}$ in k-space is written as

$$\hat{\tilde{p}}_{s,\lambda} = \frac{\mathbf{G}^T\mathbf{G}}{\mathbf{G}^T\mathbf{G} + \lambda^2\mathbf{L}^T\mathbf{L}}\mathbf{G}^{-1}\hat{\tilde{p}}_h = \mathbf{H}_\lambda^f\mathbf{G}^{-1}\hat{\tilde{p}}_h. \tag{4.6}$$

The case where the matrix $\mathbf{L} = \mathbf{I}_n$, with $\mathbf{I}_n$ the identity matrix, is known as the general or standard form Tikhonov function. The general form Tikhonov filter function is written as a function of k_{xy} as

$$H_f^\lambda(k_{xy}) = \frac{g(k_{xy})^2}{g(k_{xy})^2 + \lambda^2}. \tag{4.7}$$

For the case where the inverse solution is the sound pressure obtained from a sound pressure hologram, it follows that

$$g(k_{xy}) = e^{-j\sqrt{k^2-k_{xy}^2}(z-z_h)}, \tag{4.8}$$

and the resulting low-pass filter function for $\mathbf{L} = \mathbf{I}_n$ becomes

$$H_f^\lambda(k_{xy}) = \frac{1}{1 + \lambda^2 e^{2j\sqrt{k^2-k_{xy}^2}(z-z_h)}}. \tag{4.9}$$

A relationship between the filter cut-off and the regularization parameter λ is easily obtained from the fact that by definition $H_f^\lambda(k_{co}) = \frac{1}{2}$ at the filter cut-off, which results in

$$\lambda = e^{-j\sqrt{k^2-k_{co}^2}(z-z_h)}. \tag{4.10}$$

The deciding factor in the quality of the Tikhonov filter is the choice of $\mathbf{L}$. The Fourier representation of $\mathbf{L}$ in k-space is a weight function that connects a certain importance to the wavenumbers in the spectrum. For $\mathbf{L} = \mathbf{I}_n$ all wavenumbers are equally weighted, but the inverse solution of the acoustic wave equation might require a different approach. Wavenumbers within the radiation circle ($k_{xy} = k$) are propagating waves that are unaffected by the noise blow-up effects of the inverse solution. However, with increasing wavenumber from the radiation circle outward, the sensitivity to noise blow-up increases. As a consequence, it seems natural to choose a weight function L with the characteristic of a high-pass filter, such that the higher wavenumbers are more heavily weighted than
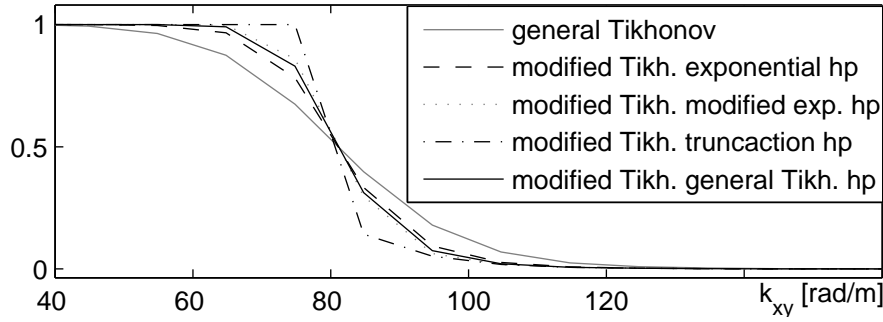
Figure 4.1: difference between general form and improved Tikhonov filters for equal regularization parameter λ

the lower ones.

It is suggested in (57) to use the complementary of the general form Tikhonov, which results in a high-pass filter function for L,

$$\hat{\bar{p}}_{s,\lambda} = \frac{\mathbf{G}^T\mathbf{G}}{\mathbf{G}^T\mathbf{G} + \lambda^2(\mathbf{H_{f,hp}^{\lambda}})^2}\mathbf{G}^{-1}\hat{\bar{p}}_h. \tag{4.11}$$

This results in a k-space low-pass filter function

$$H_f^{\lambda}(k_{xy}) = \frac{g(k_{xy})^2}{g(k_{xy})^2 + \lambda^2((g(k_{xy})^2 + \lambda^2)/g(k_{xy})^2)}, \tag{4.12}$$

It is obvious that this method would potentially produce an unlimited number of Tikhonov filters by substituting the complementary of (4.12) into (4.11) again, and so on.

A very computationally efficient method is introduced in (45) in order to find a suitable low-pass filter and use the complementary for the weight function L. Any high pass filter function is possible here, although obvious choices are the complementary values of the filter functions given in (4.1), (4.2), and (4.9), since these are especially fit for NAH problems. The resulting high-pass function $H_{f,hp}(k_{xy})$ is inserted into the modified Tikhonov function

$$H_f^{\lambda}(k_{xy}) = \frac{g(k_{xy})^2}{g(k_{xy})^2 + \lambda^2(H_{f,hp}(k_{xy}))^2}, \tag{4.13}$$

The plots for the general form Tikhonov and four different modified Tikhonov functions versus k_{xy} are shown in Fig. 4.1. For a fixed $k_{co} = 80\frac{rad}{m}$, it is clear that the general form produces a smooth sloped filter, while the stronger weight functions produce steeper slopes, with the steepest filter produced by the truncation function. In the regularization process, both λ and $H_{f,hp}(k_{xy})$ are determined with identical k_{co}, although $H_{f,hp}(k_{xy})$ could also be determined independently.

4.2.3 Low-pass Truncation filter

The low-pass truncation filter is simple and straightforward. The result of its application is twofold: First, it passes the band up to k_{co} and, secondly, stops all wavenumbers higher than k_{co}. The slope is infinitely steep and the filter function (1) is defined by

$$H_f^{k_{co}} = \begin{cases} 1, & k_{xy} < k_{co}, \\ \frac{1}{2}, & k_{xy} = k_{co}, \\ 0, & k_{xy} > k_{co}, \end{cases} \tag{4.14}$$

It appears to be the ideal discrimination between useful and useless evanescent waves, however, the infinite slope introduces errors that are highly dependent on the presented data. The choice of the complementary of (4.14) for $H_{f,hp}(k_{xy})$, in (4.13), generally results in very steep modified Tikhonov filters. The next section will address this problem and the influence of the slopes in the filters discussed above.

4.2.4 Consequences of extreme filter slopes

Ideally, a low-pass filter passes all wavenumbers below k_{co}, and halts all wavenumbers above. In very specific situations, like modal patterns in plates, a low-pass truncation filter results in a good reconstruction, on the other hand, in practice, this type of filter will mostly result in distortion of the result.

The problem is caused by the Fourier Transform of the rectangular function, $\sqcap(x)$, which is written in continuous form as

$$\int_{-\infty}^{\infty} \sqcap(x) e^{-jkx} dx = \text{sinc}(\frac{k}{2\pi}). \tag{4.15}$$

This expression illustrates the effect that emerges when the k-space source data, before inverse FFT, has a rectangular shape. A possible situation is wide-band k-space data combined with a truncation low-pass filter, for example, a wide-band k-space spectrum that emerges from point-like source behavior. The FFT of a point-like source contains energy over a wide k-space band, a sudden interruption of this pattern will result in a ringing- or "sinc"-effect emerging from the original position of the point-like source after the inverse FFT.

Finite slopes tend to suppress the ringing effect and smoothen the result. A possible drawback of a smoother slope is the suppression of useful information at wavenumbers below k_{co}, and blow-up of noise at wavenumbers above k_{co}; both effects are due to the tapering of the filter. On the other hand, sources with more discrete wavenumber content, like, for example, sine shaped disturbances, benefit from a steep slope and ringing effects are minimized. In this particular case, a steep sloped filter possibly results in a better reconstruction compared to a smooth sloped filter. One of the goals of stopping

rules is to determine the correct filter settings given the source distribution and noise circumstances.

4.3 Stopping Rules

The general purpose of regularization is to stabilize an ill-posed problem and pick out a stable solution with useful, or spatially detailed information. This approach requires additional information about the solution, and, although there are many ways to gather such information, the general method is to define a residual of the acquired solution. The idea is to find a trade-off between a sufficiently detailed regularized solution and a small residual norm. In filter terms, the noise at high wavenumbers should be suppressed, whereas the propagating waves should remain unaltered. The interesting information for the inverse solution is located outside the radiation circle. It is essential that evanescent waves with a good dynamic range pass through the filter, and on the other hand noisy wavenumbers are attenuated or stopped. The minimization process of the solution and residual term tries to find the proper filter function settings.

The previously discussed filter functions and regularization schemes show clear differences, nevertheless, they all share the same requirement of a stopping rule. This section will discuss three main types of stopping rule methods, two of which are applicable to all previously discussed filter functions; the L-curve and generalized cross-validation (GCV). The third stopping-rule, Cut-Off and Slope (COS) iteration, is specifically designed for the modified exponential filter. All stopping rules discussed in this chapter share the property of not requiring an estimate of the noise variance, which is beneficial for flexibility and speed of the holography system.

4.3.1 L-curve

The L-curve criterion is based on a parametric plot of the norm of the regularized solution versus the residual norm after filtering. The residual norm of the regularized solution, $\mathbf{x}_{reg}$, given by

$$\rho(\lambda) = \log \|\mathbf{A}\mathbf{x}_{reg} - \mathbf{b}\|_2, \tag{4.16}$$

in the general form, is large when k_{co} is small and λ is large. This is due to the fact that the applied low-pass filter suppresses a wide band of $\mathbf{x}$, leaving a large residu. By increasing k_{co} (decreasing λ), the residu becomes smaller. To find the trade-off value for k_{co} between the filter errors (over-smoothing) and perturbation errors (blow-up) in the inverse solution, the perturbation norm is required and defined as

$$\eta(\lambda) = \log \|\mathbf{x}_{reg}\|_2. \tag{4.17}$$

The perturbation norm behaves opposite to the residual norm, hence the perturbation norm increases with increasing k_{co}. After a series of increasing k_{co} and plotting $\eta(k_{co})$ versus $\rho(k_{co})$ in a log-log scale, an L-shaped curve results which is shown in Figure 4.2. The
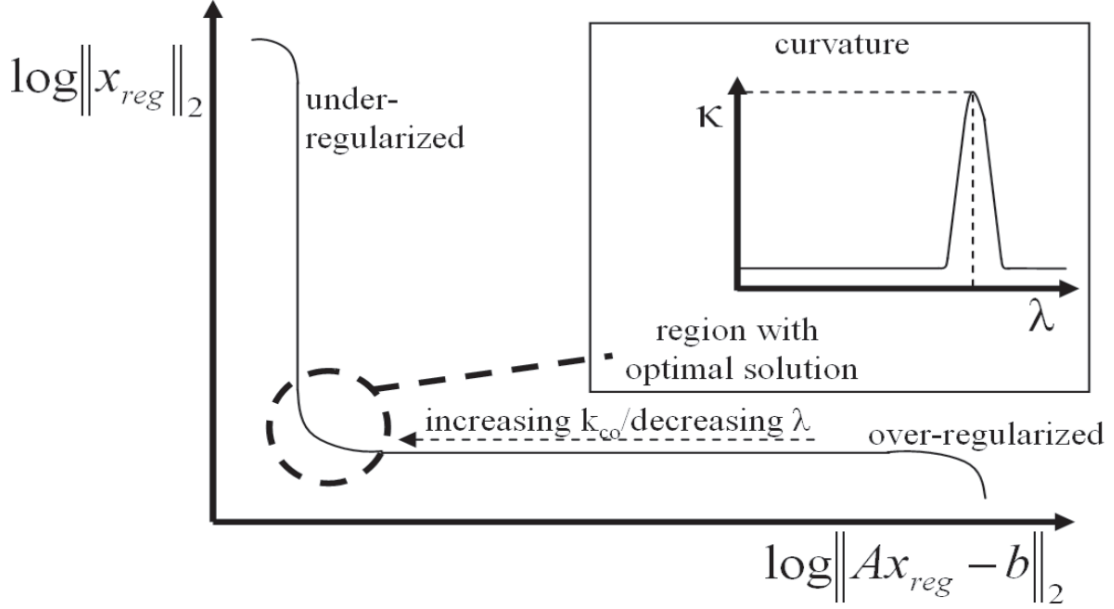

Figure 4.2: L-curve with the residual norm on the horizontal axis, and the perturbation norm on the vertical axis; the inlay shows the curvature

point on the L-curve with maximum curvature, which corresponds to the near-optimal solution, is determined by $\max\{\kappa(\lambda)\}$ with

$$\kappa(\lambda) = \frac{\rho'\eta'' - \rho''\eta'}{((\rho')^2 + (\eta')^2)^{\frac{3}{2}}}, \tag{4.18}$$

where the dash represents the first derivative and the double dash the second derivative with respect to the running variable λ, see the inlay of Figure 4.2 for a visualization. The expression for the L-curvature from (4.18) is impracticable, and a discrete algorithm is required for proper determination of the corner when only a limited number of filter cut-offs is available. For the simulations presented in this chapter, an adaptive pruning algorithm (16) was implemented.

The filter norm (residual norm) in the L-curve criterion in k-space can be determined from hologram and filter information only (46). To prove this, the filtered hologram data in k-space is defined for measured sound pressure as

$$\hat{\tilde{p}}_{hf} = \mathbf{H}_f \hat{\tilde{p}}_h, \tag{4.19}$$

where $\mathbf{H}_f$ is the filter function matrix operator for any of the previously discussed filter functions. The filtered sound pressure $\hat{\tilde{p}}_f$ at the source plane is written as

$$\hat{\tilde{p}}_f = \mathbf{G}^{-1}\mathbf{H}_f \hat{\tilde{p}}_h. \tag{4.20}$$

Both the inverse propagator $\mathbf{G}^{-1}$ and the filter matrix $\mathbf{H}_f$ are diagonal. The forward problem with input signal $\hat{\tilde{p}}_{sf}$ can be written as

$$\hat{\tilde{p}}_{h(\hat{\tilde{p}}_{sf})} = \mathbf{G}\mathbf{G}^{-1}\mathbf{H}_f\hat{\tilde{p}}_h = \mathbf{H}_f\hat{\tilde{p}}_h = \hat{\tilde{p}}_{hf}, \tag{4.21}$$

which results in an effectively calculable filter norm,

$$\rho(k_{co}) = \left\|\mathbf{G}\hat{\tilde{p}}_{sf} - \hat{\tilde{p}}_h\right\|_2 = \left\|(\mathbf{H}_f - I_n)\hat{\tilde{p}}_h\right\|_2. \tag{4.22}$$

It follows that the inverse propagator is not required to determine the residual norm of the applied filter.

The perturbation norm obviously does require the inverse propagator and the filter operator together with the hologram data, because the blow-up of noise is due to incorrect filtering and a high exponential power. In k-space the perturbation norm is

$$\eta(k_{co}) = \|\mathbf{G}^{-1}\hat{\tilde{p}}_{hf}\|_2 = \|\hat{\tilde{p}}_{sf}\|_2. \tag{4.23}$$

Since all discussed filter functions are valid for the above stated norms, this is the general form L-curve criterion for application in k-space.

4.3.2 Generalized cross-validation

Generalized Cross-Validation (GCV) is the second error-estimate-free stopping rule for estimating the filter parameters discussed in this chapter. GCV is in fact a modified version of the Ordinary Cross-Validation (OCV), which is a systematic way of determining the filter parameters from the measured data (4). The important modification to the OCV in GCV is the addition of a weighting function, which makes the method invariant to orthonormal transformations. In the NAH inverse method, orthonormal transformations are key factors, and application of OCV would make the filter function dependent on the inverse propagator.

Ideally, the Mean Squared Error (MSE) of the regularized solution and the exact solution would result in the average of the noise present in the measured data, which can be written as

$$\frac{1}{n}\sum_{j=1}^{n}(\hat{\tilde{p}}_{sf_j} - \hat{\tilde{p}}_{s,exact_j})^2 = \sigma^2. \tag{4.24}$$

Since the noise average and the exact solution are unknown in the NAH case, an estimation of this MSE is required in order to find a good estimate of the filter parameters. The GCV function for NAH is written as

$$GCV(k_{co}) = \frac{1}{n}\sum_{j=1}^{n}(\hat{\tilde{p}}_{sf_j} - \hat{\tilde{p}}_{s,exact_j})^2 w_j(k_{co}), \tag{4.25}$$

where the weights w_j are primarily determined by the filter factors as a function of k_{co} and defined as

$$w_j(k_{co}) = \left(\frac{[1 - h_{f,j}]}{(1 - \frac{1}{n}\text{Tr}\,[\mathbf{GH}_f])} \right)^2. \tag{4.26}$$

The resulting minimizing function has a numerator that is dominated by the mean squared regularization error (comparable to the horizontal axis in the L-curve), while the denominator represents the perturbation error (vertical axis in the L-curve). Equation (4.25) is rewritten as

$$GCV(k_{co}) = \frac{\|(\mathbf{I} - \mathbf{H}_f^{k_{co}})\|\hat{\tilde{p}}_h}{\text{Tr}\left[(\mathbf{I} - \mathbf{H}_f^{k_{co}})\mathbf{G}\right]}. \tag{4.27}$$

$GCV(k_{co})$ has a global minimum value for k_{co}, which represents a trade-off between over-smoothing and blow-up of noise, based on statistical analysis of noise properties.

4.3.3 Cut-off and slope iteration

For both L-curve and GCV, either the cut-off or slope of the filter is set, while inherently fixing the other filter parameter. This phenomenon limits the number of possible solutions to choose from. Often only the cut-off is adapted, while the slope is ignored. A solution to this limitation in the filter parameters is an iterative process based on the modified exponential filter introduced earlier. In the modified exponential filter both k_{co} and ϕ are varied independently, and the resulting filter functions for all possible combinations of discrete values for k_{co} and ϕ within defined margins are weighed by an existing minimization criterion.

The GCV criterion in k-space defined in the previous section is possibly a good parameter selection for the cut-off and slope of the modified exponential filter, and is calculated in k-space. For a certain cut-off and slope the GCV function will show a global minimum, and the corresponding k_{co} and ϕ are chosen for the modified exponential low-pass filter function.

A second criterion that also searches the trade-off between perturbation and over-smoothing is based on the L-curve criterion. The perturbation norm, η, and residual norm, ρ, tend to zero for increasing and decreasing λ respectively. The ζ-criterion combines both the residual and the perturbation norm together and searches for a minimum in

$$\zeta(k_{co}, \phi) = \hat{\rho}(k_{co}, \phi)\hat{\eta}(k_{co}, \phi), \tag{4.28}$$

where $\hat{\rho}$ and $\hat{\eta}$ represent the normalized residual and perturbation norm respectively. The normalized residual norm is defined as

$$\hat{\rho}(k_{co}, \phi) = \frac{\rho(k_{co}, \phi)}{\max\limits_{k_{co}, \phi}\{\rho(k_{co}, \phi)\}}, \tag{4.29}$$

and the normalized perturbation norm as

$$\hat{\eta}(k_{co}, \phi) = \frac{\eta(k_{co}, \phi)}{\max_{k_{co}, \phi}\{\eta(k_{co}, \phi)\}}. \qquad (4.30)$$

The product in (4.28) has a global minimum as a function of k_{co} and ϕ, defined as $\min\{\zeta(k_{co}, \phi)\}$. In order to find the maximum values in (4.29) and (4.30) k_{co} is varied between k_r and $\frac{1}{2}k_s$ and ϕ is varied between 0 and 1. The cut-off k_{co} and slope ϕ corresponding to the minimum are picked as modified exponential filter parameters, which is referred to as the ζ-criterion. This criterion provides solutions that lie to the left in the L-curve compared to the solution resulting from the adaptive pruning algorithm, yet still in the elbow area of the curve. In terms of high resolution results, this behavior proves to be beneficial for high SNR cases.

4.4 Numerical Validation

In the numerical simulations it is important to produce test problems with a rich evanescent wave content, in order to illustrate and compare the influence of different filter functions and stopping-rules. For this matter, a flat surface with a number of point-like sources, a vibrating surface with modal behavior, and a mixture of both modal and point-like sources are chosen.
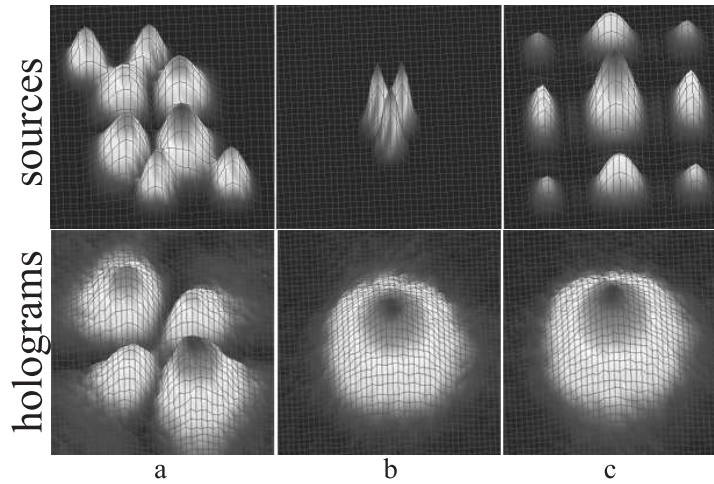

Figure 4.3: sound pressure at three source planes $z = z_s = 0$ m (upper images) and three hologram planes $z = z_h = 0.05$ m, from left to right: a) mixed source of (2,2)-mode combined with four point-like sources; b) three point-like sources; c) modal source in (3,3)-mode

4.4.1 set-up of the simulations

The artificial sources are defined as sound pressure distributions at $z = z_s = 0$, which are shown in Figure 4.3. The source and hologram plane grids measure 64 by 64 positions, further specifications are listed in Table 4.1.

 The mixed source (Figure 4.3a) contains both broadband k-space information caused by

Table 4.1: hologram measurement parameters of the three numerical sources

three sources: points, mode and mixed							
aperture height	Y	64	cm	aperture width	X	64	cm
vertical spacing	Δy	1	cm	horiz. spacing	Δx	1	cm
standoff dist.	z_h	5	cm				
signal freq. 1	f_{s1}	2	kHz	signal freq. 2	f_{s2}	6	kHz
SNR 1		15	dB	SNR 2		35	dB

the point-like source, as well as discrete wavenumber content introduced by the modal pattern. The point-like source (Figure 4.3b) has three point-like sources closely spaced together that introduce a broad k-space, which makes these type of sources very sensitive to ringing effects caused by the low-pass filter. The modal source (Figure 4.3c) contains discrete, small band wavenumber content, because the modes contain a low number of discrete sine waves, and for this reason a very steep or truncation low-pass filter is possibly a good solution.

The hologram is calculated from the source pressure distribution, random noise is then added to the sound pressure information at signal-to-noise ratios of 15 and 35 dB. By application of PNAH on the generated holograms the source distribution is back-calculated and compared to the known exact solution.

4.4.2 influence of parameter choice

low-pass filter slopes

As mentioned earlier, the slope of a low-pass filter is essential for successfully filtering noisy data of a specific source. Figure 4.4a illustrates the influence of the filter steepness in case of the modal source distribution. For the modified exponential filter with slope $\phi = slp = 0$ the exact solution is best estimated. The more gradual sloped filters filter part of the k-space source data, resulting in an underestimation of the peak-values in the signal. Consequently, some of the higher, noisy wavenumbers are passed through, while hardly any source information is present. This causes the noise to dominate the solution, which is most obvious at the outer edges of the mode shape sample. Figure 4.4b shows relative error information on the influence of the modified exponential filter slope com-
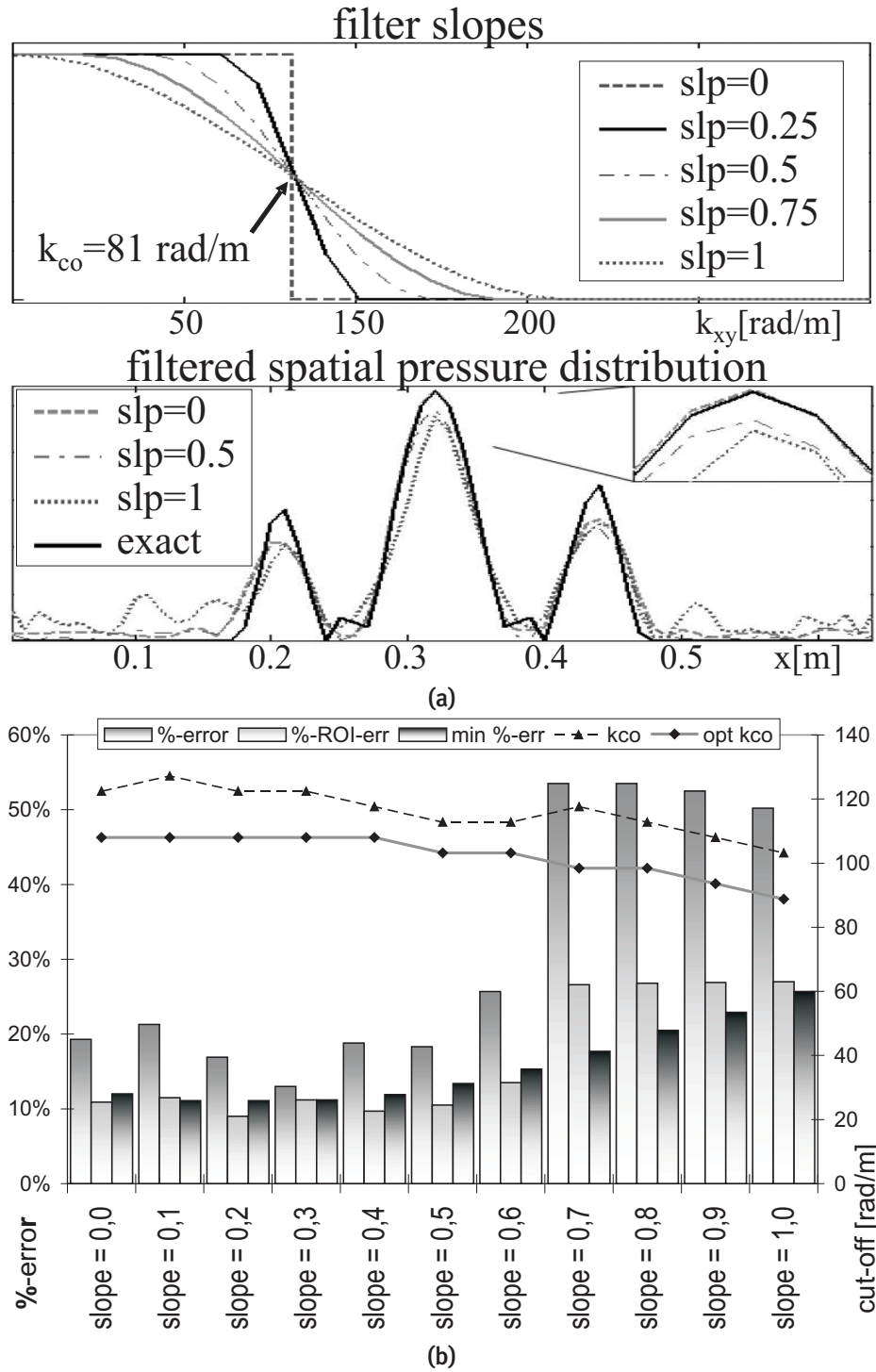
Figure 4.4: modal source, $f = 2$ kHz, $SNR = 15$ dB; modified exponential filter slopes between 0 and 1 and L-curve stopping rule. a: influence of different filter slopes on the resulting source spatial pressure distribution. b: influence of filter slopes on the %-error and cut-off resulting from L-curve stopping rule

bined with L-curve criterion in order to determine the proper k_{co}.

The bars represent forms of the mean-squared %-error over the total area. The first of every bar triplet is the general %-error found by the respective stopping rule and corresponding k_{co}. Secondly, the %-ROI-error is also resulting from the stopping rule, however, the error is taken from a region of interest (ROI) closely surrounding the source information. Thus, a large difference between these two means there exist large error differences between source and surrounding areas. The third bar represents the optimal or minimum %-error found after iteratively searching a large number of cut-offs and pick the optimal k_{co} with the minimum %-error. Since the optimal %-error is also taken over the complete spatial area, it is possible that the %-ROI-error turns out smaller. For this case, both the potentially best and the determined slope (by L-curve) are found at $\phi = 0.3$ and $k_{co} = 122\frac{rad}{m}$. This clearly shows a large influence of the filter slope on the end-result and, consequently, the %-error.
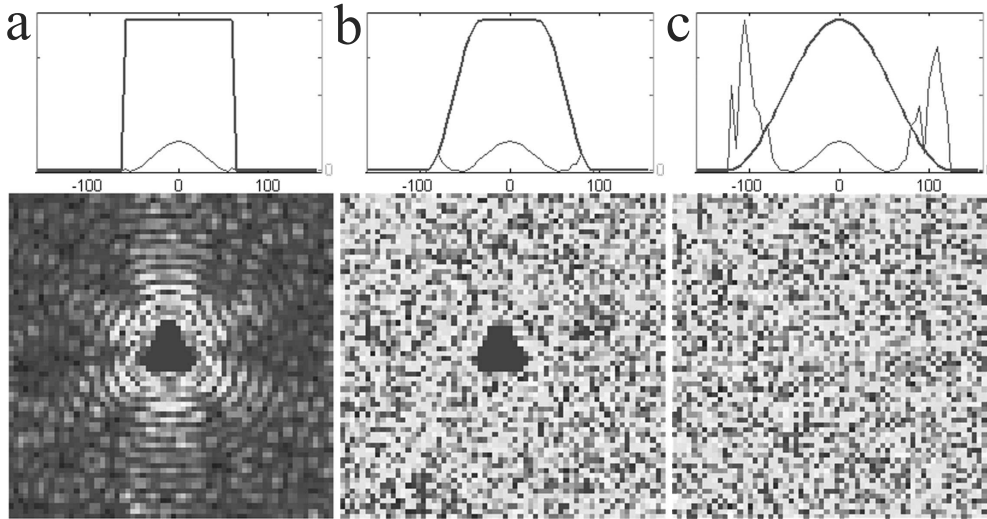

Figure 4.5: ringing effect of a steep slope (a) for the point-like sources case, while increasingly smoother slopes (b and c) suppress the ringing and pass more noise at a fixed k_{co}

Contrarily, a steep sloped filter will cause a ringing-effect to broadband k-space sources. An example of such a case is the sound pressure hologram with three point-like sources. The results of a truncation (a), steep- (b), and gradual-sloped (c) low-pass filter are shown in Figure 4.5, where the effect of the truncation filter is clear; it suppresses the blow-up of noise at higher wavenumbers, yet the abrupt cut-off produces a wave pattern moving radially outward. Again, an increasingly gradual slope causes the noise to expand disproportionately. Situation (b) is the best trade-off between noise and filter errors; the source information is still visible, and the noise remains at an acceptable level. The noise blow-up is obvious in situation (c), where the noise side lobes in the wavenumber domain overrule the source information in the center of the spectrum.

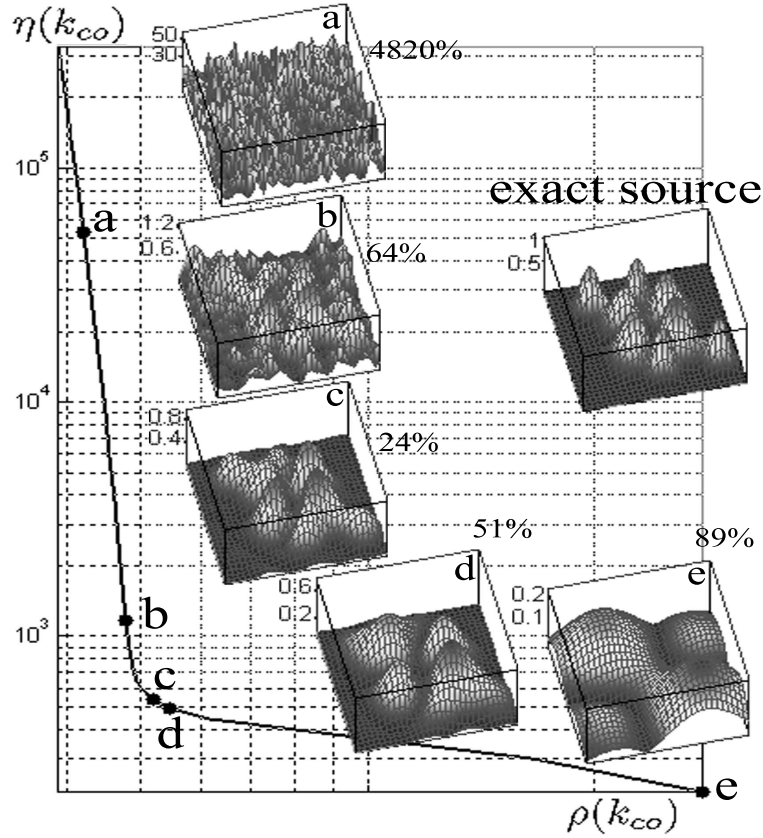## stopping rule for correct filter parameters

Figure 4.6: L-curve for mixed sources at different positions in the curve, the %-error is shown at the top-right of the resulting source planes for given L-curve values (black dots)

The stopping rule is used to determine the optimal filter parameters. In practice, it is of great value to get a good approximation of the optimal solution, which ensures that the resulting image shows real source information, instead of, for example, noisy artifacts. One of the discussed stopping rules is the L-curve criterion, which is illustrated in Figure 4.6 for the mixed case with four point-like sources and a (2,2)-mode in the center of the plane.

In this case, the resulting plot of $\log(\eta(k_{co}))$ versus $\log(\rho(k_{co}))$ is clearly L-shaped. Moving from right to left along the curve (with increasing k_{co}) causes the filter error to decrease. While at the horizontal part (point e to d) the perturbation error, caused by the blow up of noise, is zero until the "elbow" of the L is reached (point c). From this point onward, the filter error remains steady (point c, through b to a), while the perturbation error exponentially increases, causing the solution to become worthless.

The point of maximum curvature is approximated using a discrete algorithm, which, in this case, assigned point d as the best option. Compared to the exact solution, the filtered solution at d is clearly over-regularized as it is a smooth estimate of the exact source.

Close to point d lies point c, which gives the overall best solution given the applied low-pass modified exponential filter with $\phi = 0.2$. This image is clearly a better estimate with more spatial detail than solution d. It also illustrates how sensitive the regularized solution is as a function of the filter parameters. Following the path along the curve upwards results in an explosive increase of the %-error.

4.4.3 filter function and stopping rule comparison

In addition to the fundamental definitions, properties and some of the pit-falls concerning filter slopes and cut-offs of the filter functions and stopping rules that have been discussed, a number of graphs are used to compare all possible combinations for three stopping rules and five filter functions. All three earlier defined test-cases are used with either a 15 dB or a 35 dB signal-to-noise ratio (SNR), at either 2 or 6 kHz. A selection of four situations, concerning a combination of case, frequency and SNR, is picked and the results are shown in the charts of Figure 4.7. The first displayed case, the (3,3)-modal source at $f = 2$ kHz and $SNR = 35$ dB, in Figure 4.7a shows that the L-curve over-estimates k_{co}, while k_{co} is mainly under-estimated by the GCV. Although the truncation filter cut-off is best estimated with the lowest %-error, it should be noted that the COS iteration with the ζ-criterion nearly approximates this performance. The general exponential filter clearly performs worst. This case also shows that the %-ROI-errors for the L-curve-stopped filters are lower than the optimal %-errors, which could point out that a slightly higher k_{co} results in richer source information, although some noise in the surrounding areas is starting to blow up.

Secondly, the same case is observed at $f = 2$ kHz and $SNR = 15$ dB, which is shown in Figure 4.7b. This case is at a significantly lower SNR, and since the hologram distance is already rather large at $z_h = 0.05$ m, the inverse solution is very sensitive to noise. The average %-errors illustrate this sensitivity to noise in the hologram, and the GCV clearly out-performs the L-curve stopping rule, while both stopping rules under-estimate the optimal k_{co}. The fact that the COS iteration based on the GCV criterion out-performs the ζ-based one underlines the better performance of GCV under extreme noise conditions. Generally speaking, the modified exponential filter combined with COS iteration showed the best possible solution, which is based on visual comparison of source and result.

The results of point-like sources at $f = 6$ kHz and $SNR = 35$ dB is illustrated in Figure 4.8a, with clearly a very good performance of the L-curve stopping rule. All cut-offs found by the L-curve stopping criterion match, or nearly match, the optimal solution for any of the five tested filters. Especially the modified exponential and Tikhonov filter show very small errors, however, the COS iteration based on the ζ-criterion finds the best solution possible. The GCV stopping rule is another story; it heavily under-estimates the cut-offs resulting in large errors and incapability of differentiating between the independent sources, whereas the L-curve results clearly show all three.

(a) modal source: $f = 2$ kHz, $SNR = 35$ dB; COS ζ crit.: $\phi = 0.17$, $k_{co} = 121\frac{rad}{m}$, %err. $= 15,1\%$; COS GCV crit.: $\phi = 0$, $k_{co} = 90.9\frac{rad}{m}$, %err. $= 17,7\%$
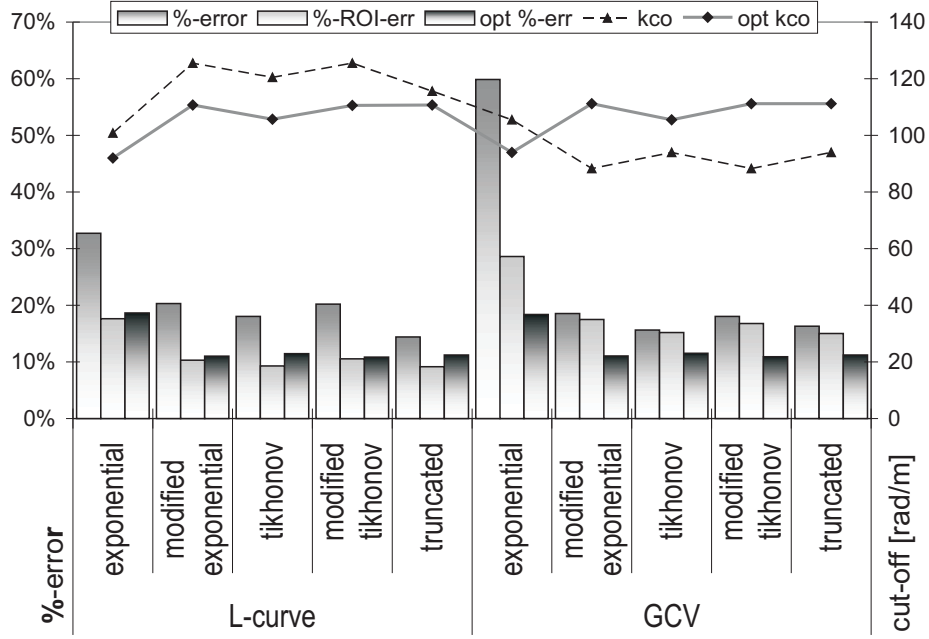
(b) modal source: $f = 2$ kHz, $SNR = 15$ dB; COS ζ crit.: $\phi = 0.29$, $k_{co} = 53.8\frac{rad}{m}$, %err. $= 60.0\%$; COS GCV crit.: $\phi = 0.13$, $k_{co} = 65.3\frac{rad}{m}$, %err. $= 44.8\%$

Figure 4.7: graphs with %-errors for two stopping rules and five filters for two different cases and the results from the COS iteration procedures; $z_h = 0.05$ m, $z_s = 0$ m, $\gamma = 0.2$, $\phi = 0.2$, and modified Tikhonov with a modified exponential filter with $\phi = 0.3$

(a) point sources: $f = 6$ kHz, $SNR = 35$ dB; COS ζ crit.: $\phi = 0.08$, $k_{co} = 158\frac{rad}{m}$, $\%err. = 7.90\%$; COS GCV crit.: $\phi = 0.04$, $k_{co} = 126\frac{rad}{m}$, $\%err. = 36.9\%$

(b) mixed sources: $f = 2$ kHz, $SNR = 35$ dB; COS ζ crit.: $\phi = 0.21$, $k_{co} = 111\frac{rad}{m}$, $\%err. = 9.54\%$; COS GCV crit.: $\phi = 0.21$, $k_{co} = 94.0\frac{rad}{m}$, $\%err. = 16.5\%$
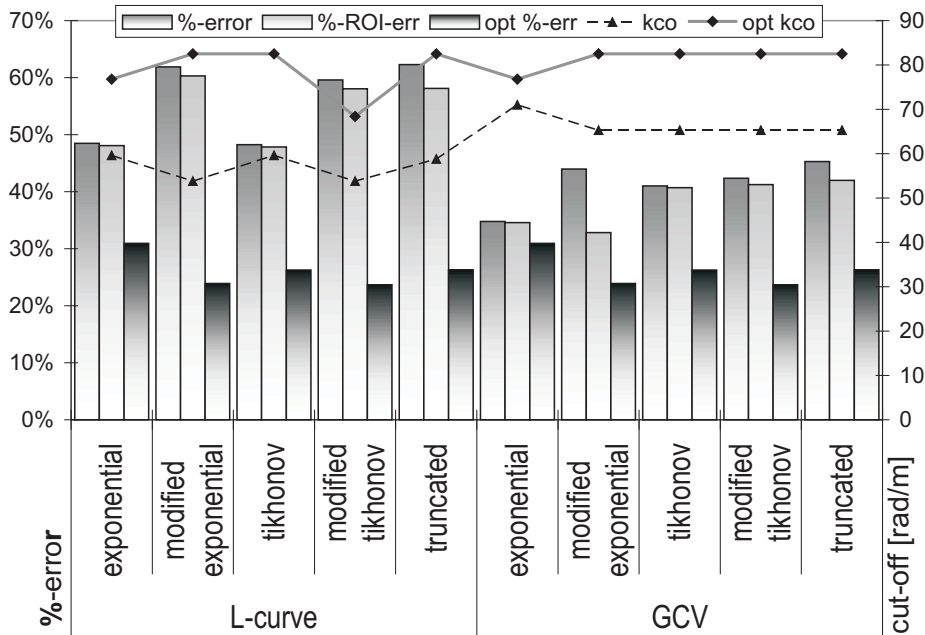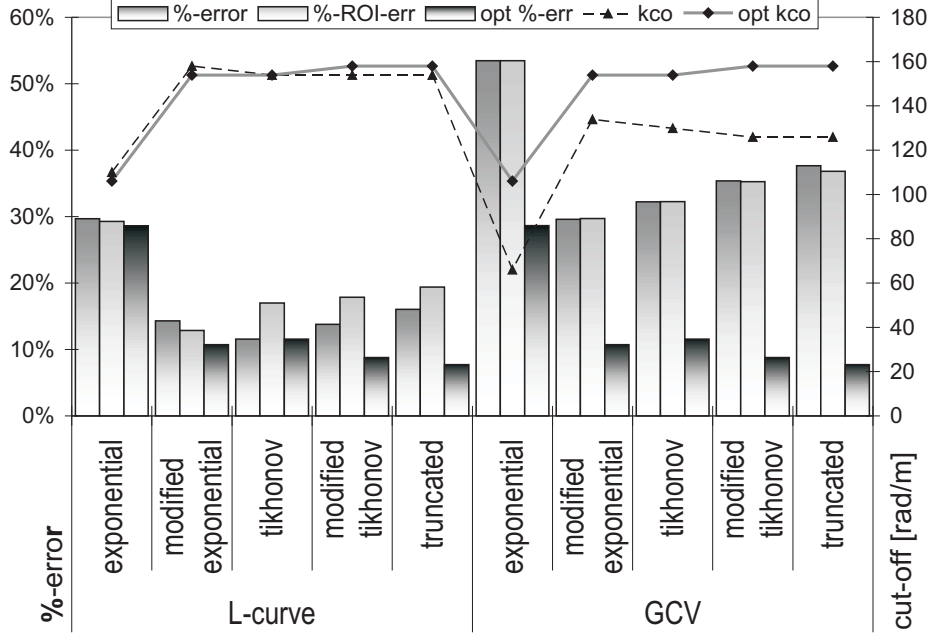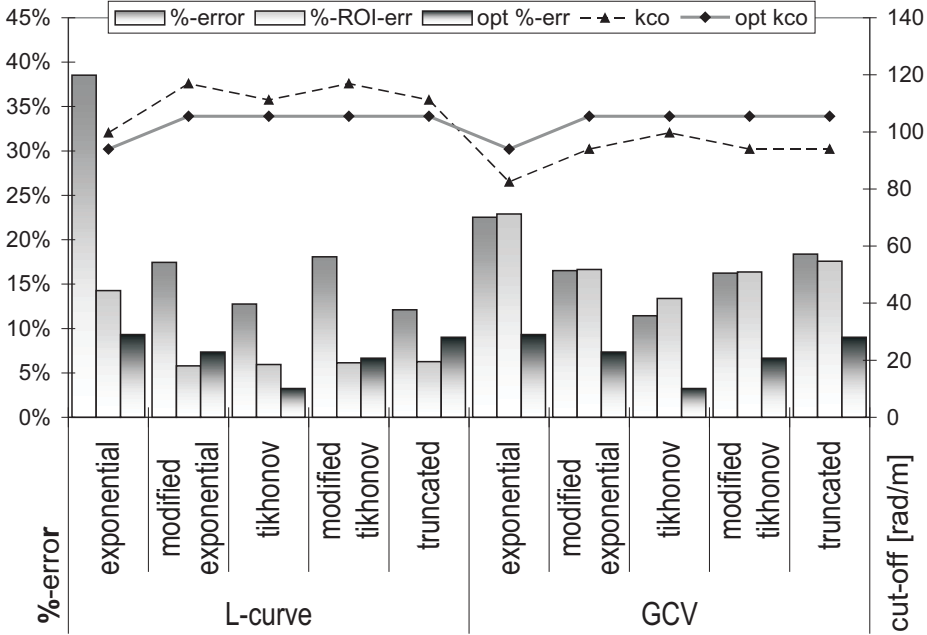

Figure 4.8: graphs with %-errors for two stopping rules and five filters for two different cases and the results from the COS iteration procedures; $z_h = 0.05$ m, $z_s = 0$ m, $\gamma = 0.2$, $\phi = 0.2$, and modified Tikhonov with a modified exponential filter with $\phi = 0.3$

Lastly, the graph of the mixed sources case at $f = 2$ kHz and $SNR = 35$ dB, given in Figure 4.8b, shows the bad performance of the general exponential filter. This underlines the sensitivity of the exponential filter for the cut-off k_{co}, since the cut-off resulting from both stopping rules nearly estimate the optimal k_{co}, yet the %-error is very large. Besides that, again, the L-curve criterion over-estimates k_{co} compared to the under-estimation by the GCV. The %-error for both L-curve and GCV are comparable, yet the %-ROI-errors and qualitative results are significantly better for the L-curve-stopped filters. The third stopping rule, COS iteration based on the ζ-criterion combined with the modified exponential filter, however, results in the lowest %-error and the best qualitative solution.

4.5 Discussion

The newly introduced modified exponential filter, combined with the Cut-Off and Slope (COS) iteration method and a ζ-criterion (based on the L-curve criterion) out-performs every tested filter function and stopping rule combination in case of medium to good noise conditions. Overall, the results show that the optimal regularization method depends heavily on the type of source, the spatial source distribution and the signal-to-noise ratios of the hologram data. The L-curve criterion performs best for cases with medium to high signal-to-noise ratios, while the GCV criterion over-regularizes the data resulting in low resolutions, yet better performance with noisy cases.

Five implemented filter functions are discussed and tested in simulations, these are combined with three different stopping rules for near-optimal parameter selection. L-curve application in k-space is shown to be an efficient parameter selection for (modified) exponential, (modified) Tikhonov and truncation filter functions. Generalized Cross-validation determines a single, near-optimal solution for the filter parameters, yet a more computationally intensive process is required for optimal implementation of the filter function. The modified versions of both the Tikhonov and exponential filters perform best overall. These also show the highest potential for future improvements of parameter selection criteria, because of the flexibility in altering their parameters.

A particular problem arises when steep sloped filters are applied to data with rich wavenumber content over a large bandwidth, which results in erroneous source information with a typical ringing effect emerging from the source areas. Taking this into account, steep sloped filters, such as the truncation filter, should generally be applied to sources with low, discrete wavenumber content, e.g. modal behavior in plates or large covers. On the contrary, sources with high, broad wavenumber content require more gradually sloped low-pass filters.

Finally, a general strategy for handling regularization in PNAH starts with the application of COS iteration based on the ζ-criterion combined with a modified exponential filter. This method delivers a near-optimal cut-off and slope to the low-pass filter, which will suffice for most practical cases under low to medium noise conditions. Under extreme

noise conditions, the COS iteration based on the GCV is preferred, since it mainly over-regularizes the solution. If the automated result from COS iteration is unsatisfactory, the L-curve is used with the resulting slope from COS iteration and the L-curve elbow is searched in order to manually find the proper filter cut-off.

Experimental Validation in an Anechoic Environment

The methods introduced and discussed in the previous three chapters were mostly illustrated with numerical experiments, however, the ultimate tests and verification of the near-field sound imaging techniques are real experiments. In this chapter, the practical relevance of the developed methods is shown and verified under anechoic conditions, in order to be able to focus on a certain aspect of the sound imaging process. The controlled environment is situated in the semi-anechoic chamber of the Mechanical Engineering Department of the Eindhoven University of Technology, where only the floor has a reflecting surface and the walls and ceiling are covered with sound absorbing materials. The measurement set-up and signal processing hardware is described and illustrated in section 5.1. The regularization for PNAH by means of filter functions and stopping rules is tested on a set-up with baffled point sources in section 5.2. Also, in a high-resolution case it is shown that the evanescent-to-propagating ratio is larger than zero. Section 5.3 primarily handles the comparison of linear predictive border-padding with basic border-padding and general form spatial windowing techniques. Parts of results shown in this chapter are published in (42; 43; 44; 45). Finally, this chapter is concluded in section 5.4.

5.1 Set-up of the controlled environment

The measurement set-up used for the practical cases shown in the next section is situated in a semi-anechoic room at the Department of Mechanical Engineering at the Eindhoven University of Technology (Figure 5.1). An automated traverse system that is shown in the front moves a microphone beam over a pre-defined grid in front of the source of interest. The used sensor is a low-noise, omni-directional, miniature Sonion 8002 mi-

crophone with a package diameter of 2.5 mm and a membrane with a diameter of only 0.7 mm. These small dimensions make the sensor very suitable for near-field measurements relatively close to a sound source, without disturbing the acoustic field due to its presence. Every grid measurement is carefully phase matched to the reference signal, which is either measured with one of the reference sensors, or directly determined from the excitation signal. The choice of reference signal depends on the specific case.

photograph by Bram Saeys

Figure 5.1: semi anechoic room with the measurement set-up in the fore-ground at the mechanical engineering department of the Eindhoven University of Technology

The signal from the microphone is transported over a shielded twisted pair cable to a low-noise pre-amplifier, which boosts the signal within the optimal range of the Siglab data-acquisition system with four inputs and two outputs at a maximum of 50 kHz sampling frequency. The Siglab system performs the A/D conversion and is connected to the post-processing PC system via a SCSI interface. All measurements at the independent hologram positions are stored in separate files on a hard disk drive. With the developed post-processing software, measured holograms are determined for the complete frequency range that was chosen in the Siglab software. From this point on, the PNAH software toolbox under $Matlab$™ is used to determine the required sound images. The control of the traverse system, excitation of the source (when required), measurement, vi-

sual source imaging and post-processing of all grid positions are fully integrated and automated in the developed NAH software package. The post-processing software contains a regularization toolbox that incorporates all previously mentioned filters and stopping rules.

5.1.1   point sources in a rigid baffle

Point sources are exceptionally well-suited source types for NAH verification purposes, because their source locations are well-defined and the wavenumber content is spread over a wide band, and up to the highest wavenumbers. This makes it relatively easy to make a qualitative analysis and test regularization methods. A rigid wooden baffle with a pattern of holes in an aluminum plate, as shown in Figure 5.2a and b, is used to approximate a point source pattern.
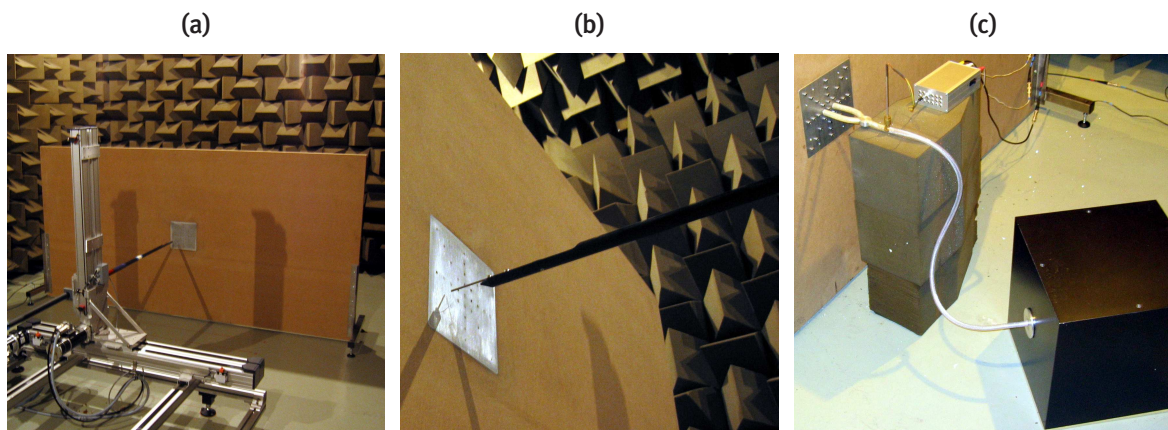
(a)	(b)	(c)

Figure 5.2: measurement setup of baffled point sources in a semi-anechoic room (a); the hologram is spatially sampled by a single miniature microphone mounted on a traversing beam (b), an isolated speaker connected to the backside of the baffle (c)

At the backside of the baffle (Figure 5.2c), it is possible to either connect a tube with an isolated speaker to one or more of the holes, or to fill up the holes and restore the baffle. It is possible to place the reference microphones at the back of the baffle, mounted in the tube that connects an isolated speaker to the back-plate of the aluminium baffle part. The speaker inside the black box is excited by a Siglab data acquisition system connected to an amplifier, the measured pressures are fed back into Siglab for post-processing.

5.2 Regularization comparisons and verification in practice

5.2.1 point source patterns

For the first measurement series, performed on the baffle containing two point-sources, the tube is split up and connected to two channels in the center of the aluminium source plate, creating two coherent point sources of 5 mm diameter with about 40 mm horizontal spacing between them. The front-side view of these two sources is depicted in Figure 5.3a.
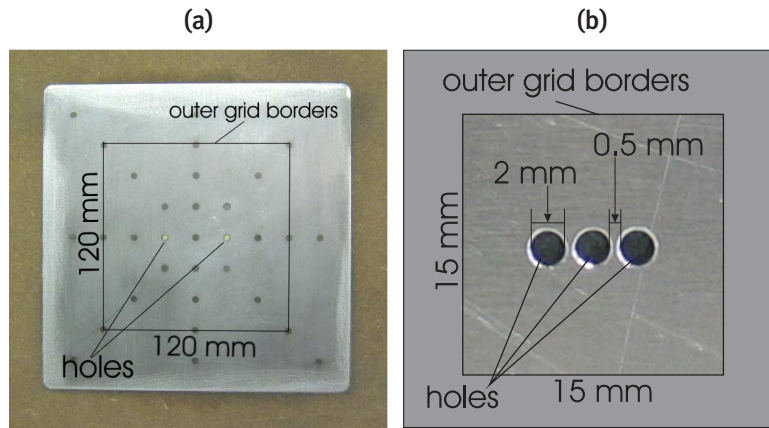

Figure 5.3: close-up of the aluminium plate with various pattern possibilities (a) and the separate, high-resolution plate with three small point sources (b)

In the second measurement series, the first plate is changed to the high-resolution source, which requires a much higher spatial sampling resolution in order to distinguish the three point sources shown in Figure 5.3b, which are 2 mm in diameter and 0.5 mm apart from one another. Note that all excited point sources are in phase on both set-ups.

5.2.2 results two point sources

The experimental results for the first measurement series are extracted from a large number of measurements, as described in the previous section. For the analysis conducted in this section, the measurement information concerning the processed holograms is given in Table 5.1.

The influence of the filter functions and the GCV and L-curve stopping rules, for a standoff distance $z_h = 15$ mm is observed in Figure 5.4 and 5.5. The differences in cut-offs that are found for the same filter function illustrate that the GCV generally over-regularizes the solution compared to the L-curve criterion. Also, since the L-curve consistently manages to find a higher appropriate cut-off, the resulting source images are sharper, of higher sound pressure level and closer to the spatial dimensions of the two

Table 5.1: hologram measurement parameters of the two point sources, medium resolution case

source: two point sources (40mm apart)							
aperture height	Y	12.5	cm	aperture width	X	12.5	cm
vertical spacing	Δy	5	mm	horiz. spacing	Δx	5	mm
standoff dist. 1	z_{h1}	20	mm				
standoff dist. 2	z_{h2}	15	mm	signal freq. 1	f_{s1}	1881	Hz
standoff dist. 3	z_{h3}	10	mm	signal freq. 2	f_{s2}	1428	Hz

point sources when compared to the GCV results. On the other hand, the L-curve results already show a high influence of noise in the result, which illustrates the trade-off between useful data and noise blow-up.

In all cases, the L-curve criterion creates clear L-shaped curves and the GCV functions show distinct global minima, thus regularization parameters are determined easily. Although most of the cut-offs of the respective stopping rules lie in the same range, the filter slopes differ considerably. The general form exponential and Tikhonov filters mainly show a very smooth slope, while the truncation filter ordinarily displays an infinitely steep slope. The modified exponential and Tikhonov filter slopes lie somewhere in between and are easily adjustable. Considering the qualitative comparison, both Tikhonov filters and the modified exponential filter perform best when combined with the L-curve. The general form exponential filter slope is too smooth to make a good trade-off between noise and high spatial changes (high wavenumbers), thus showing a large portion of noise blow-up and too little spatially important source information. The truncation filter is the opposite; it allows high spatial changes, however, ringing artifacts due to the infinite slope tend to distort the results too much.

The COS iteration with the GCV and ζ-criterion show clear differences in results at the source plane, as can be observed from the images in Figure 5.6. The results at 20 mm, 15 mm and 10 mm are either the measured holograms or results of ζ-criterion based, COS filtered forward or backward PNAH solution. If image a4 and b5 in Figure 5.6 are compared, it can be concluded that the ζ criterion results with a hologram plane 5 mm further away from the source than the hologram used as input for the GCV criterion based rule, show equal results at the source. This means that the ζ-criterion regularizes less and reveals more high spatial frequency information, without blowing up too much noise. Comparing image b4 and c5 leads to the same conclusion. Also, the ζ-criterion solution at the source is by far the sharpest display of the actual point source size and displays the highest sound pressure levels, without blowing up noise. Not only does the ζ-criterion based COS iteration perform well for this case, it has also shown to be the best choice for numerous other test cases that have been performed. Besides all the filter issues, this figure illustrates the importance of standoff distance and the exponential loss of near-field information over very short distances. This is obvious when the inverse
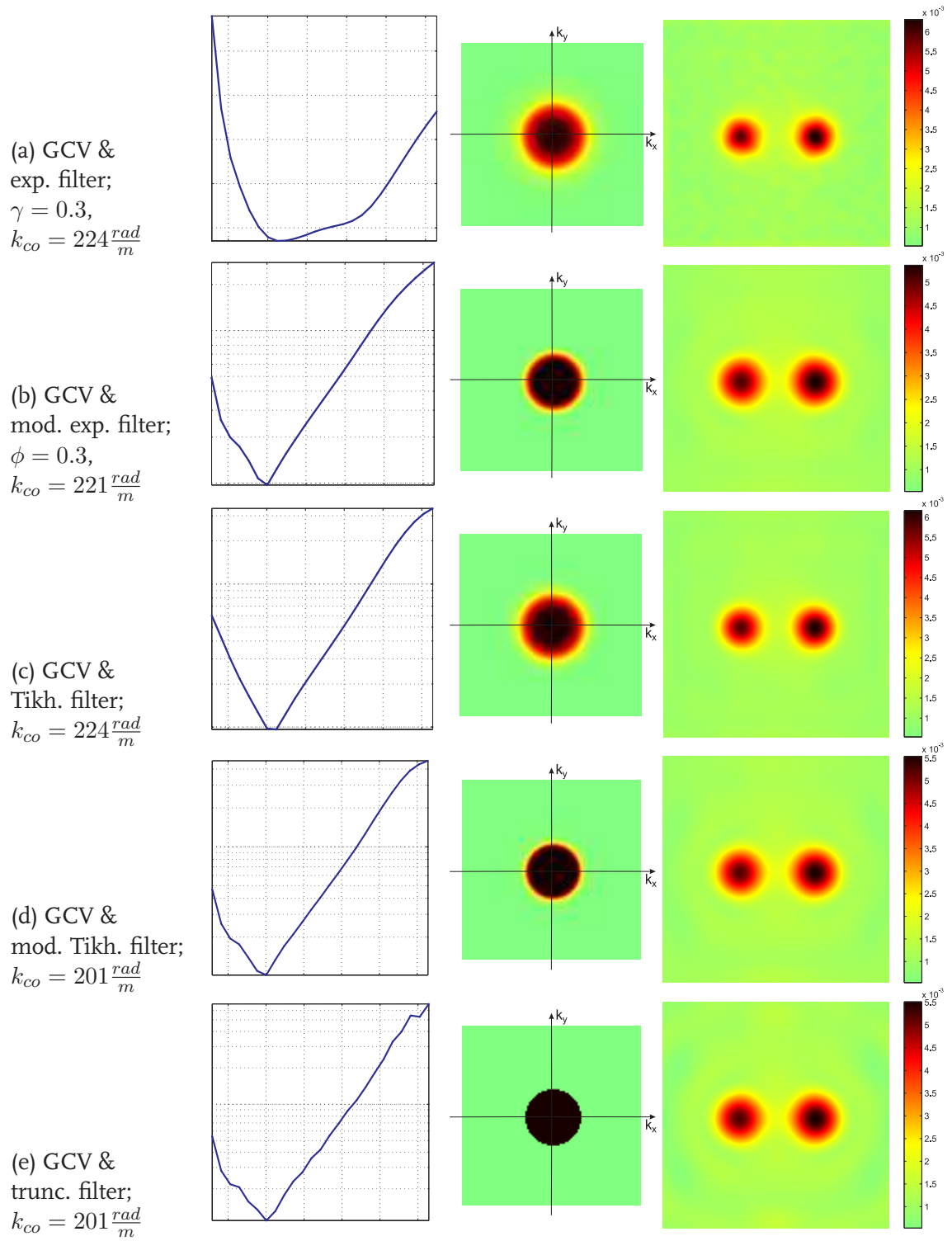
Figure 5.4: comparison of five filters and the GCV stopping rule; plots show the GCV (left), the resulting low-pass filter in k-space (center) and the filtered, absolute sound pressure reconstruction at $z = 0$ mm for $f_{s1} = 1881$ Hz and $z_{h2} = 15$ mm

(a) L-curve & exp. filter; $\gamma = 0.3$, $k_{co} = 248\frac{rad}{m}$

(b) L-curve & mod. exp. filter; $\phi = 0.3$, $k_{co} = 343\frac{rad}{m}$

(c) L-curve & Tikh. filter; $k_{co} = 343\frac{rad}{m}$

(d) L-curve & mod. Tikh. filter; $k_{co} = 367\frac{rad}{m}$

(e) L-curve & trunc. filter; $k_{co} = 343\frac{rad}{m}$

Figure 5.5: comparison of five filters and the L-curve stopping rule; plots show the L-curve (left), the resulting low-pass filter in k-space (center) and the filtered, absolute sound pressure reconstruction at $z = 0$ mm for $f_{s1} = 1881$ Hz and $z_{h2} = 15$ mm
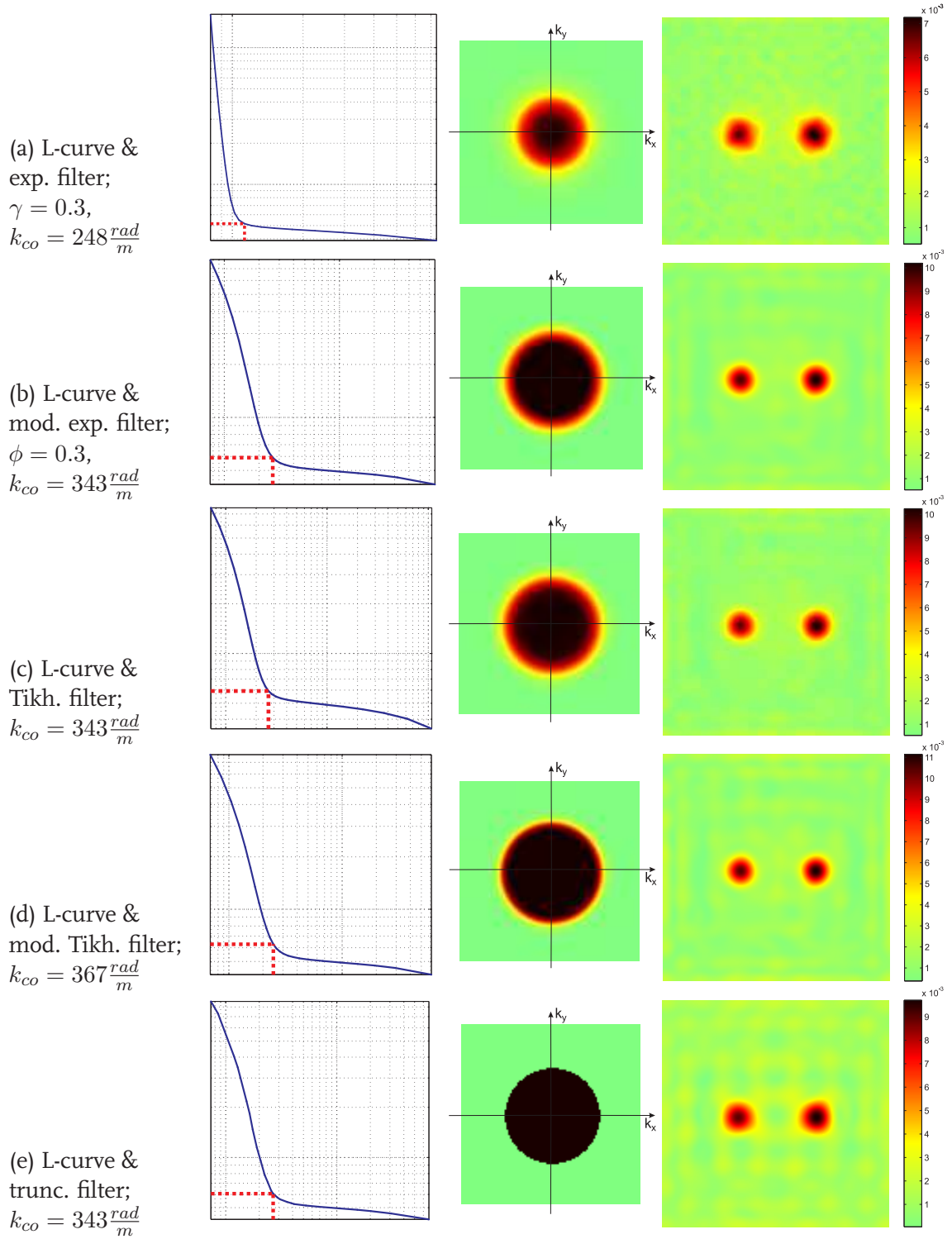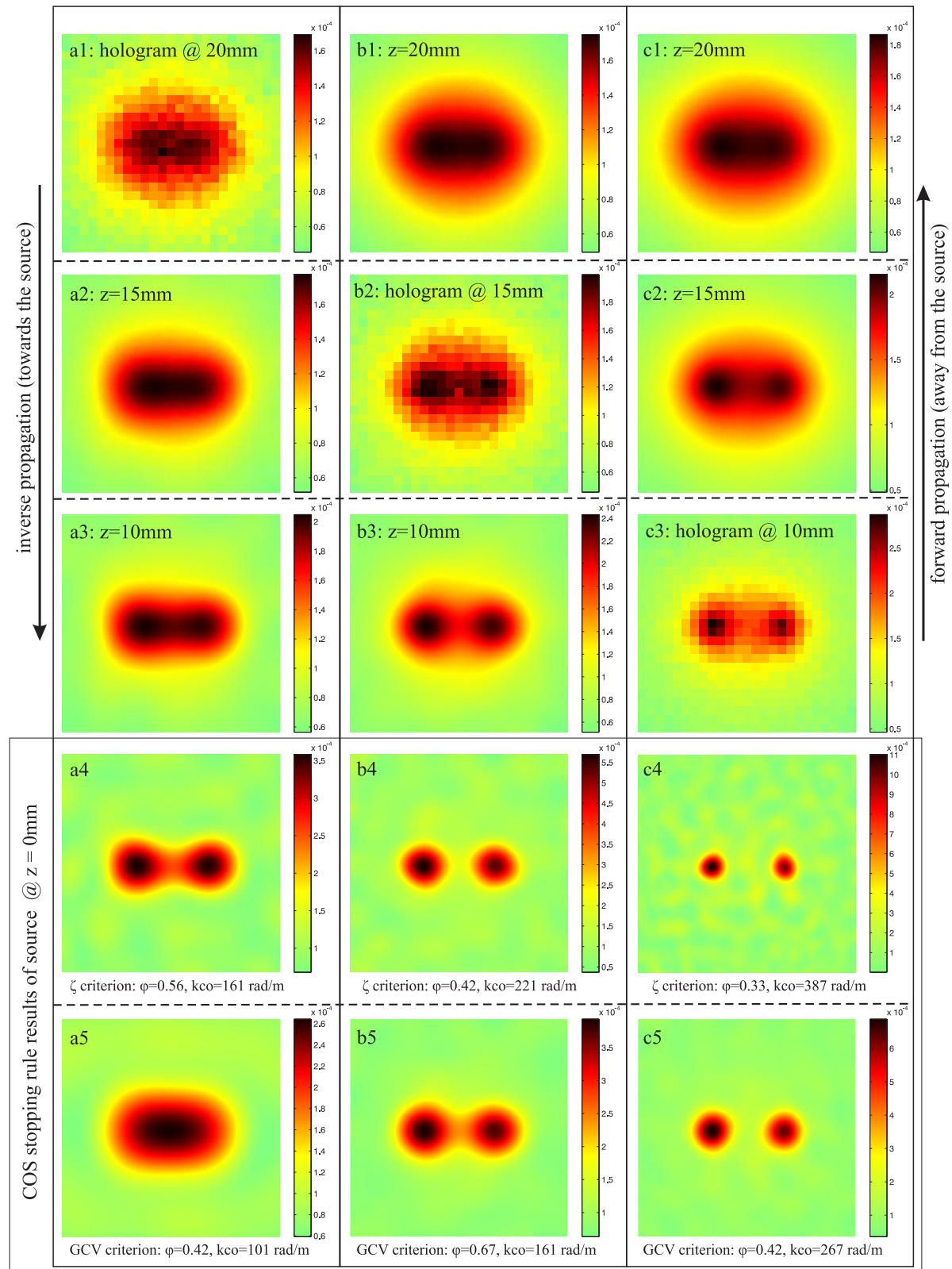
Figure 5.6: Cut-Off and Slope iteration results $|\tilde{p}(x,y)|$ $[Pa]$ at $f_{s2} = 1428$ Hz

solution of the pressure hologram at 20 mm, provided in Figure 5.6, is compared to the inverse solution of the hologram measured at $z_{h3} = 10$ mm for either the COS iteration with GCV or ζ-criterion (Figure 5.6 a4, a5 and c4, c5 respectively). With the GCV criterion for COS iteration and a standoff distance of 20 mm it is impossible to distinguish the two sources in a5.

5.2.3 results three point sources

Table 5.2: hologram measurement parameters of the three point sources, high resolution case

source: three point sources (0.5mm apart)							
aperture height	Y	15	mm	aperture width	X	15	mm
vertical spacing	Δy	0.3	mm	horiz. spacing	Δx	0.3	mm
standoff dist. 1	z_h	1	mm	signal freq.	f_s	1362.5	Hz

(a) spatial resolution
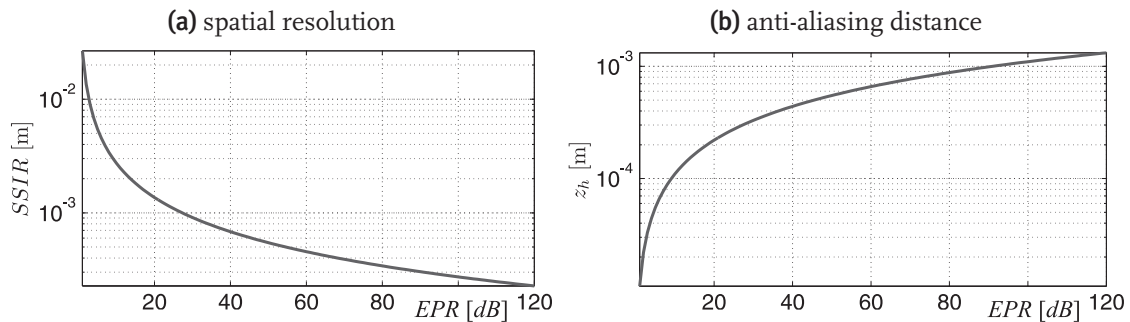
(b) anti-aliasing distance

Figure 5.7: spatial sound image resolution (a) and standoff distance (b) as a function of the evanescent-to-propagating ratio for the three point sources measurement with $\delta = 0.3$ mm and $z_h = 1$ mm

The second measurement series at high resolution are an even greater challenge for the regularization algorithms, since the sources are closer to each other (Figure 5.3b) and the noise conditions are of greater influence, because the near-field is shorter for these point sources of only 2 mm diameter. The maximum propagating wave amplitude is below the noise floor of the measurement system, because in the far-field, the source is inaudible and the noise floor for this specific case is around 45 dB, which results in $SNR = 0$ dB with (2.13). The possible $SSIR$ for a range of EPR, which follows from (2.21), is shown in Figure 5.7a. More important for the determination of the anti-aliasing standoff distance is Figure 5.7b, where (2.23) is used to plot the standoff distance against the EPR for $\delta = 0.3$ mm. It follows that it is save to consider a standoff distance of 1 mm. The complete hologram measurement parameters for this case are provided in Table 5.2. The

grid-size for this high-resolution measurement is 50 by 50 points in horizontal and vertical direction.

Figure 5.8 and 5.9 illustrate the results after regularization and PNAH post-processing for GCV and L-curve respectively. The acoustic images containing the calculated sound pressure, particle velocity in the normal direction, and the sound intensity in the normal direction at the source plane are given.

The exponential filter results shown in Figure 5.8a and 5.9a are poor with either the GCV or L-curve stopping rule; The GCV rule over-regularizes, while the L-curve under-regularizes and blows up too much noise. In this case, the reason of failure is mainly due to the filter function, since the slope is not steep enough to provide a cut-off that actually shows all three sources clearly, without blowing up too much noise. Generally speaking, the GCV is hardly able to perform well for this sensitive case, in all but one situation the data is over-regularized and only a single large source is distinguished. Only for the Tikhonov filter (Figure 5.8c) function a proper cut-off is found, resulting in the detection of three separate sources. However, the results after Tikhonov filtering combined with the L-curve criterion (Figure 5.9c) show too much noise blow-up, especially in the particle velocity and sound intensity images. The best results, showing a good compromise between the distinction of three sources and the minor blow-up of noise, follow from the L-curve criterion. The modified exponential, modified Tikhonov, truncation filter, and COS with the ζ-criterion provide comparably good solutions. With any of these methods it is possible to acquire high resolutions below 1 mm.

From the results in Figure 5.8 and 5.9, it is clear that the sound pressure images at the source are less detailed than the particle velocity and sound intensity counterparts in normal direction. The sound intensity shows the sharpest source images, while highly suppressing the noise blow-up compared to the particle velocity. For individual source recognition and highest possible resolution it is most beneficial to determine the normal sound intensity besides the sound pressure and particle velocity. For source behavior, however, all available sound field information should be investigated. For example, plotting the sound pressure changes over time and space within a single period of the transmitted sound is often very helpful in understanding the origins and behavior of certain sources. This information is obtained by an equal rotation of the phase over the whole source plane.

Another interesting observation from these results is the obtained $SSIR$. As mentioned in chapter 2, normally the $SSIR$ (2.21) is obtained under the assumption that the amplitudes of all waves (evanescent and propagating) are equal at the source ($EPR = 0$ dB). Here, the $SNR = 0$ dB, which theoretically results in $SSIR = 12.5$ cm when $EPR = 0$ dB is considered. However, the obtained $SSIR$ in this practical case is approximately $0.8 - 1.1$ mm, based on the Rayleigh resolution criterion and the width of the dips in between the three peaks. From (2.21) and Figure 5.7a, it follows that the evanescent-to-propagating ratio is at least $EPR = 30$ dB. These results indicate that the EPR is of
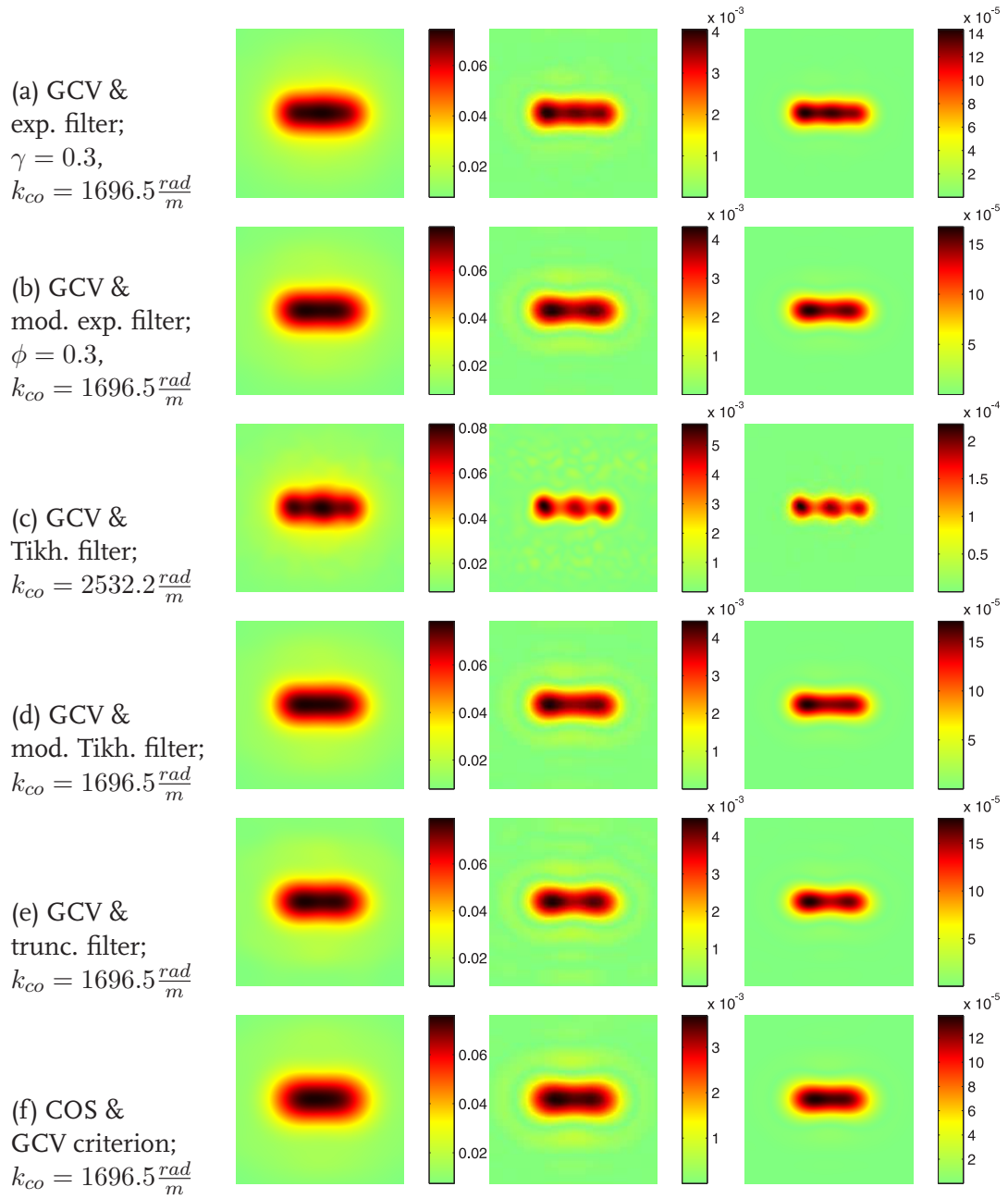
Figure 5.8: comparison of five filter types combined with GCV and COS iteration; For every regularization combination the sound pressure (left), particle velocity (center) and sound intensity (right) after PNAH and filtering at the source plane for $f_s = 1362.5$ Hz and $z_h = 1$ mm are provided

influence in the determination of the spatial sound image resolution, and also plays an important role in the aliasing criterion, especially in practice.
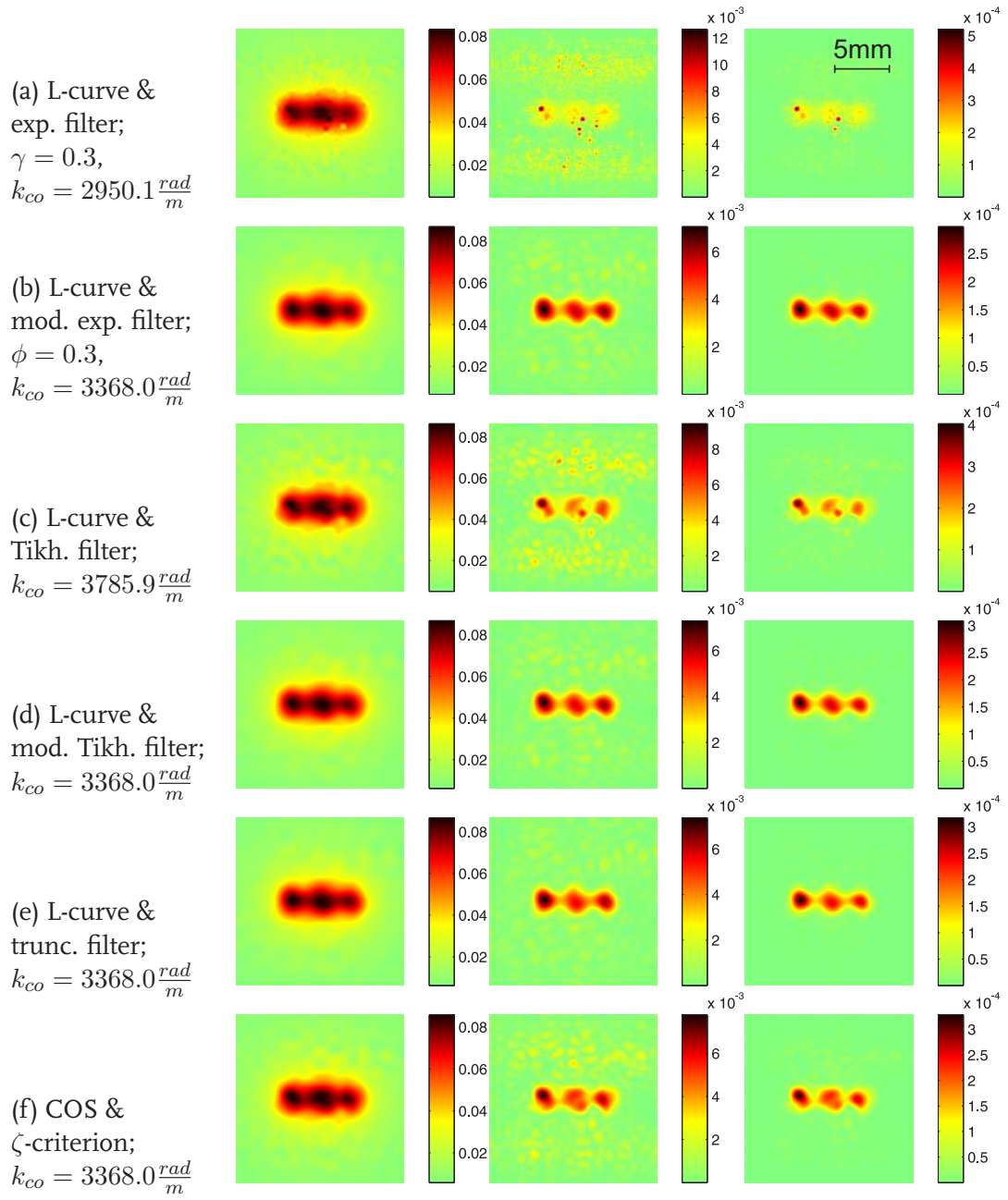
Figure 5.9: comparison of five filter types combined with L-curve and COS iteration; For every regularization combination the sound pressure (left), particle velocity (center) and sound intensity (right) after PNAH and filtering at the source plane for $f_s = 1362.5$ Hz and $z_h = 1$ mm are provided

5.3 Border-padding in practice

5.3.1 measurements

In a real-life situation, the source distribution is generally unknown, which requires a robust extrapolation method that is able to deal with many different circumstances, source distributions and noise. To illustrate the applicability of border-padding, two highly practical cases are considered: a hard disk drive and a cooling fan. In the case of the hard disk drive, a frequency is observed where the source distribution mainly contains lower wavenumbers lying just outside the radiation circle. On the other hand, the cooling fan is observed at the rotational frequency where the total number of blades (seven) is observed in the source image. In the latter case, the wavenumbers that contain source information are much higher than the hard disk drive case, and the sources originating from the blades are rotating in the aperture plane.

The hard disk drive under test is a Quantum Fireball LCT10, mounted in a vertical po-

Table 5.3: hologram measurement parameters of the real-life border-padding cases

a: hard disk drive Quantum Fireball LCT10 (idle spinning)							
aperture height	Y	21	cm	aperture width	X	17	cm
vertical spacing	Δy	1	cm	horiz. spacing	Δx	1	cm
standoff dist.	z_h	2	cm	signal freq.	f_s	1075	Hz
b: Cooling fan Sunion (43k4 rpm)							
aperture height	Y	6.4	cm	aperture width	X	6.4	cm
vertical spacing	Δy	2	mm	horiz. spacing	Δx	2	mm
standoff dist. 1	z_h	2	cm	signal freq.	f_s	722	Hz

sition with the top cover facing forward, driven in idle mode. The sensor is traversed to pre-defined measurement grid points, which results into a hologram of sound pressure when phase matched to a second, spatially static reference microphone. The measured equidistant grid counts 21 rows by 17 columns with 1 cm inter-sensor distance at 2 cm from the source plane, see Table 5.3a for all hologram information. The hologram at one of the peak-frequencies of $f_s = 1075$ Hz is shown in Figure 5.10a.

For the cooling fan, a grid of 32 by 32 is used at a standoff distance of 2 cm and an inter-sensor distance of 2 mm. The hologram at the peak-frequency of $f_s = 722$ Hz, which is equal to the rotational speed of the fan, is shown in Figure 5.10b. The air flow caused by the cooling fan rotation is directed to the back, away from the measurement plane, more hologram information is provided in Table 5.3b.

In both cases, the spatial sampling parameters are chosen, taking into account the considerations and aliasing criteria mentioned in chapter 2. Also, the modified exponential filter introduced in (45) is used, with an L-curve criterion to determine the filter cut-off.
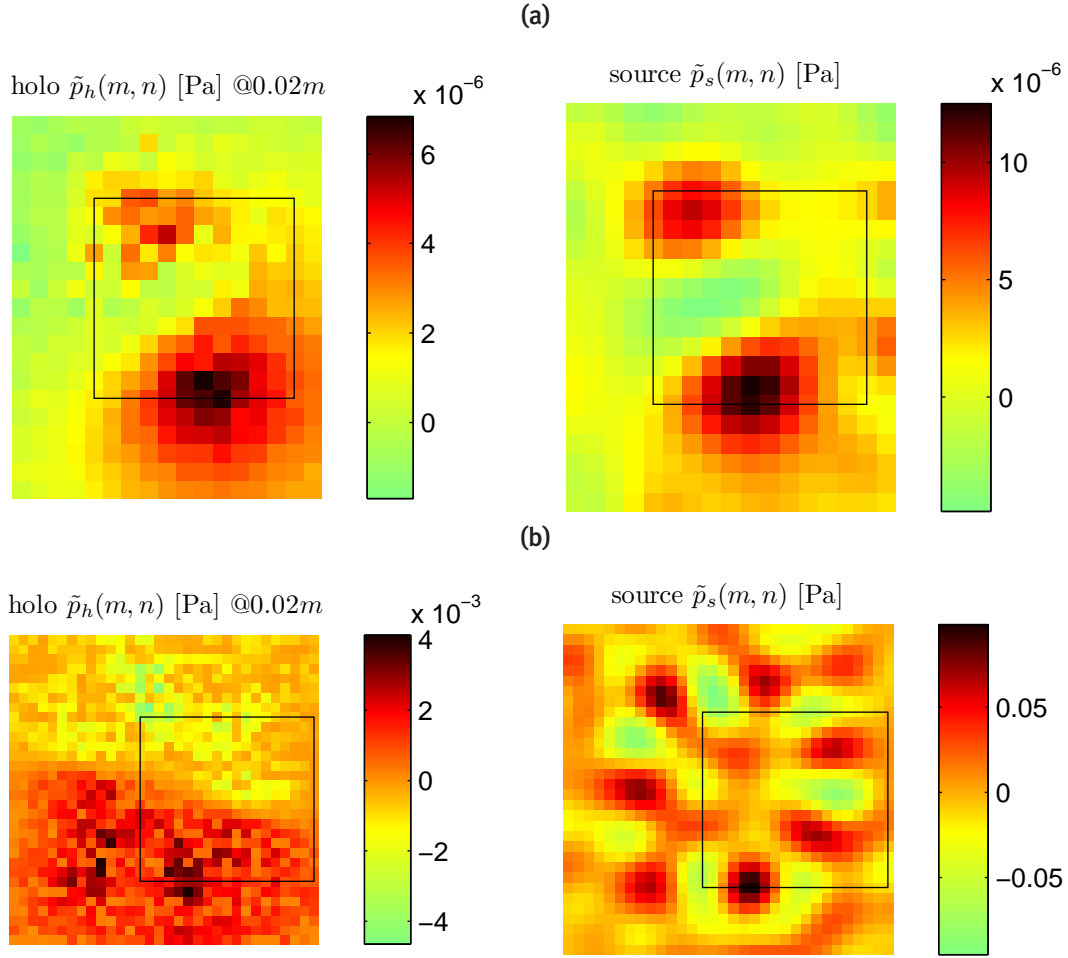
(a)

holo $\tilde{p}_h(m,n)$ [Pa] @0.02m x 10^{-6}

source $\tilde{p}_s(m,n)$ [Pa]   x 10^{-6}

(b)

holo $\tilde{p}_h(m,n)$ [Pa] @0.02m x 10^{-3}

source $\tilde{p}_s(m,n)$ [Pa]

Figure 5.10: acoustic images of (a) the measured hologram @ 1075 Hz (left) of the hard-disk drive and the PNAH result at the source plane (right) for a fully processed aperture and (b) the measured hologram @ 722 Hz (left) of the cooling fan and the PNAH result at the source plane (right) for a fully processed aperture

Obviously, in case of the hard disk drive, a different cut-off is chosen for the filter compared to the one used in the cooling fan case, yet once a cut-off is chosen for a single case, it is used for all applied border-padding methods in order to compare them under equal circumstances. At first, the total available aperture is used to process the entire source, then the selection from the hologram aperture is chosen and processed separately. Now, both the calculated inverse solutions of the sound source are compared with the full aperture as reference.

5.3.2 results

The practical results mainly show the same trend as the numerical analysis in chapter 3, although the errors are somewhat larger due to the presence of measurement noise in both holograms. The hard disk drive case shows the lowest errors due to the lower

wavenumber content and amount of measurement noise. The difference between linear predictive border-padding on one side and basic border-padding and windowing on the other side is significant, both qualitative and error-wise.

An interesting observation is the near equal RMSRE error of both the windowing (Figure 5.11.1) and the basic border-padding (Figure 5.11.2) results, and the clearly better qualitative result for basic border-padding. This difference illustrates the fact that low quantitative errors can occur, however, the usefulness for proper source identification is questionable. The cooling fan case shows much higher wavenumber content, especially along the borders of the chosen aperture. Here, all three types of border-padding perform well, even basic border-padding (Figure 5.12.2), which failed in the numerical high wavenumber case (Figure 5.12.2). The good performance of basic border-padding is very dependent on the aperture choice in this example, since the data near the border fits the cosine tapering very well, in the sense that the smooth wave pattern is more or less continued by the tapered border-padding. Overall, basic border-padding performs worse than linear predictive border-padding and at some point, at high wavenumber content, the numerical errors become too large and blow up the result after the inverse propagation.

In both cases, the higher order prediction filter is bound to extrapolate more noise near the border, resulting in more leakage. This is also the reason of the relatively good performance by the basic border-padding algorithm compared to the numerical simulations, since it is less sensitive to noisy behavior within the aperture itself. The other alternative, spline border-padding, is highly sensitive to noise and, although it shows reasonably good results in the numerical modal case, it fails in both practical applications, as shown in Figure 5.11.5 and 5.12.5. The standard windowing and zero-padding method shows fairly good RMSREs, yet the qualitative results in Figure 5.11.1 and Figure 5.12.1 are very poor, which makes this method inappropriate for this kind of source identification.

From these results on actual measured holograms of real-life cases, the practicability of border-padding is illustrated. Even in the presence of noise and only a very limited number of data points, still good and reliable results follow from applying either basic or linear predictive border-padding. A broader research on the influence of noise and the size of the border-padded aperture is required to give a distinct conclusion on a practically optimal choice of the filter order in linear predictive border-padding. However, based on these results both the $2nd$ and $8th$ order description provide the best qualitative and quantitative results in the test, and are both good standard orders to implement in practice.

5.4 Conclusions

In this chapter, the practical relevance of the methods introduced in the three previous chapters is illustrated by means of measurement set-ups in an acoustically controlled environment. The controlled environment is needed to reduce the number of factors
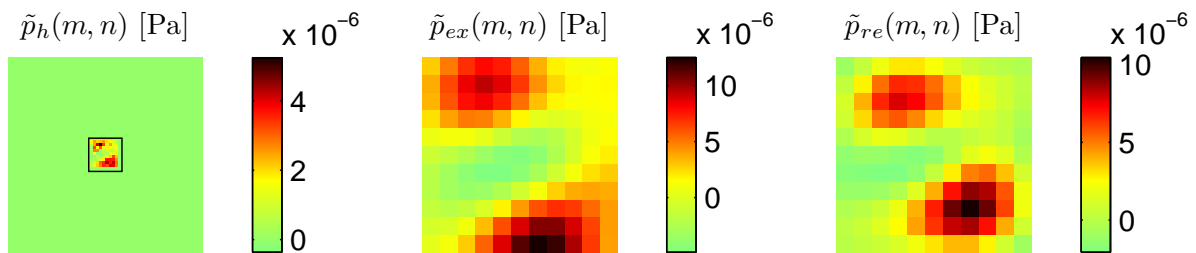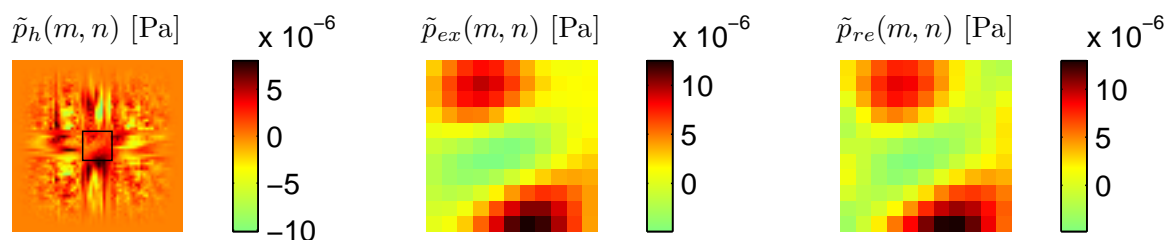
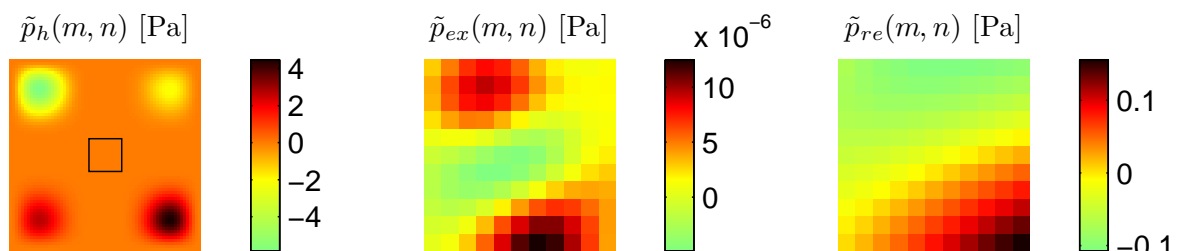1) windowing & zero-padding: hologram, exact source and result: RMSRE=44.6%
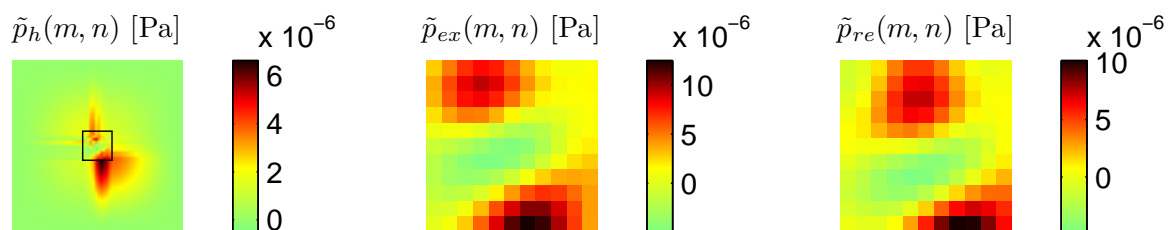
2) basic border-padding: hologram, exact source and result: RMSRE=44.2%
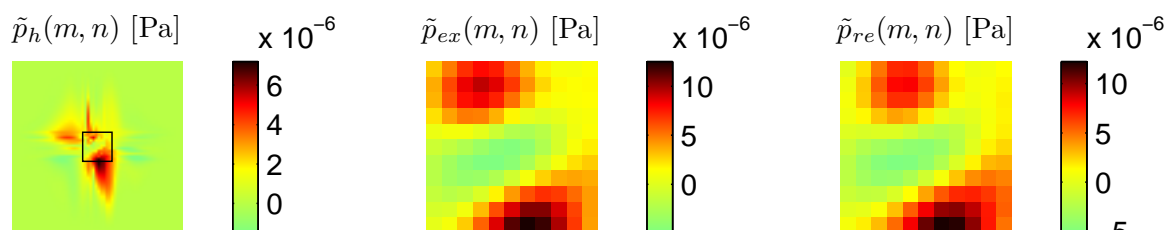
3) order 2 lin. pred. border-padding: hologram, exact source and result: RMSRE=8.6%

4) order 8 lin. pred. border-padding: hologram, exact source and result: RMSRE=13.8%

5) spline border-padding: hologram, exact source and result: RMSRE=1105783.8%

Figure 5.11: five types of data extrapolation on measurements of the hard-disk drive and processed with PNAH, the rectangles mark the selected, smaller aperture that is border-padded

1) windowing & zero-padding: hologram, exact source and result: RMSRE=55.2%

2) basic border-padding: hologram, exact source and result: RMSRE=29.1%

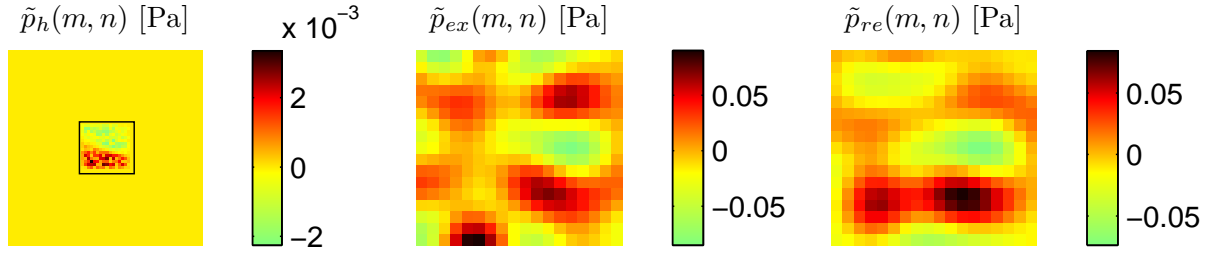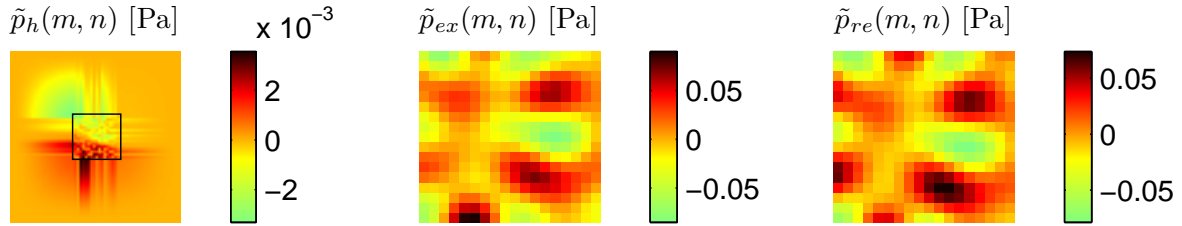3) order 2 lin. pred. border-padding: hologram, exact source and result: RMSRE=21%

4) order 8 lin. pred. border-padding: hologram, exact source and result: RMSRE=24%

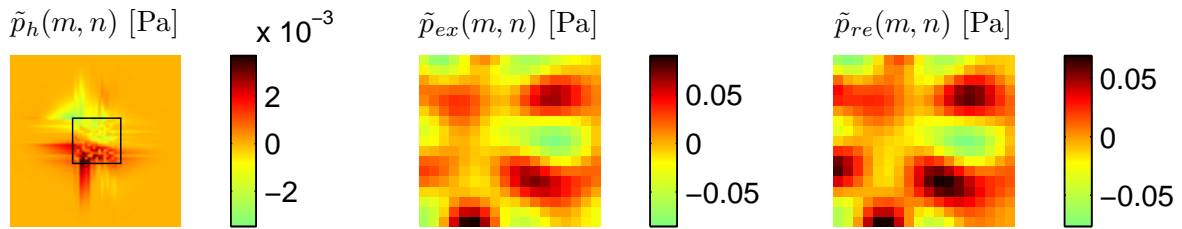5) spline border-padding: hologram, exact source and result: RMSRE=123770%

Figure 5.12: five types of data extrapolation on measurements of the cooling fan and processed with PNAH, the rectangles mark the selected, smaller aperture that is border-padded
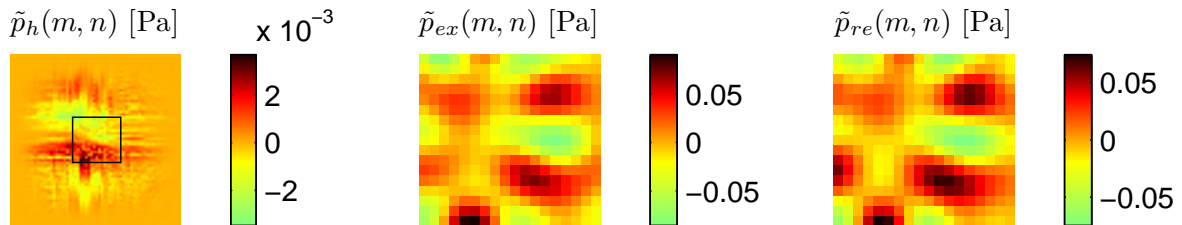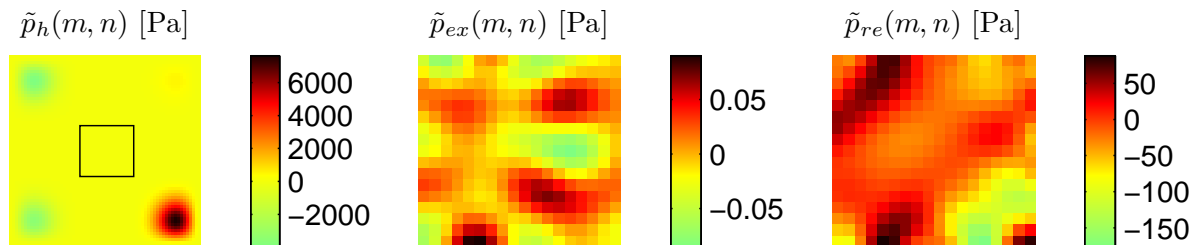
of influence to the individual methods that are tested. The practical results presented in section 5.2 lead to the same conclusions made in chapter 4, based on the numerical experiments. The best performance overall is made by the automated COS regularization method. Furthermore, the three point sources case illustrated a $SSIR$ of approximately 0.9 mm, which indicates the importance of the EPR in spatial resolution and aliasing analysis. The estimated evanescent-to-propagating ratio $EPR \geq 30$ dB, because the SNR of the propagating part is not measurable. Finally, linear predictive border-padding was compared to a number of other spatial anti-leakage and windowing methods for PNAH. Here, it appears that linear predictive border-padding is by far superior in all shown cases to spatial windowing and spline border-padding. The difference between linear predictive border-padding and basic border-padding is less in some cases and large in others, yet overall, linear predictive border-padding always manages to provide a high quality result for each case. These practical results are very similar to the results of the numerical experiments in chapter 3.

Automated Near-field Sound Imaging Technology Eindhoven

A fully automated near-field sound imaging system requires three main areas of automation that were previously manually controlled. First, the clamping of the object and, most importantly, the optimal positioning of the sensors and the spatial orientation of measurement plane with respect to the source of interest are key to the proper determination of the acoustic holograms. The spatial leakage and windowing problem for Fourier based NAH is minimized by the application of linear predictive border-padding, which is discussed in chapter 3. Noise regularization by the automated COS algorithm and modified low-pass filter functions is considered the third and final missing step to fully automate the NAH imaging process.

  The consecutive steps are given in Figure 6.1, the integration of these steps into the patent pending[1] automated near-field sound imaging technology Eindhoven (ANSITE) system is discussed in the following sections. Section 6.1 integrates steps 1 to 5 that involve (optimal) sensor and source positioning for FFT based systems. Here, a positioning strategy design is presented that minimizes errors due to, for example, spatial aliasing and determines the required sensor spacing given a requested resolution and frequency band of interest. Section 6.2 elaborates on steps 6 to 11, which are part of the inverse signal processing software. The signal processing software includes algorithms and theory discussed in previous chapters, concerning border-padding, COS regularization and inverse calculation in k-space. An often overlooked, yet very important, part for practical and industrial application is the visualization of the results. NAH is potentially very powerful for a large range of acoustic source identification and classification sub-

---

[1] R. Scholte, I. Lopez, N.B. Roozen, H. Nijmeijer, *Acoustic Holography*, Patent: EP08155162.4 (24 april 2008)
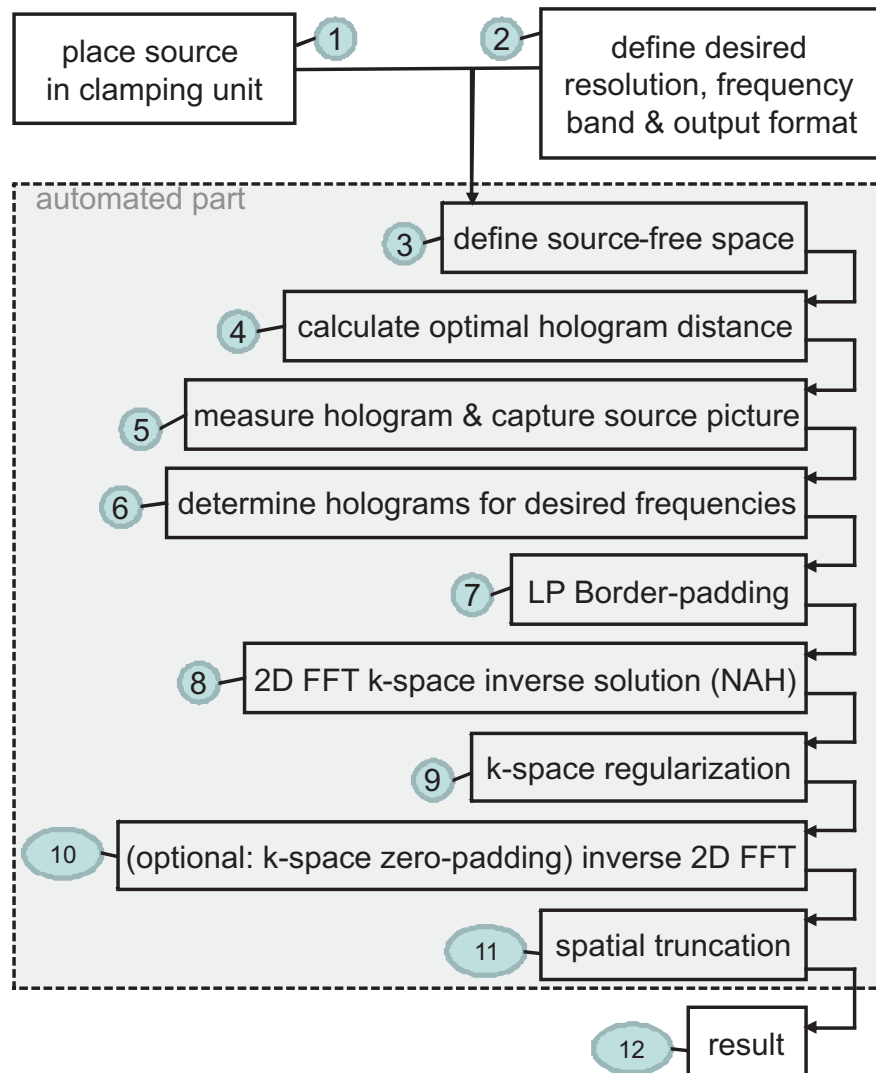
Figure 6.1: system diagram

jects with many applications still to be determined. Section 6.3 discusses a collection of visualization methods, which are suitable for correct integration in the ANSITE system. Finally, three different embodiments or representations of the ANSITE system are given in section 6.4, followed by conclusions in section 6.5.

6.1 Optimal sensor positioning

Proper use of the spatial domain properties is a key element for any acoustic imaging technology, and it is even more important for near-field acoustic imaging. The reason behind this is the sensitivity of the evanescent waves with respect to the exact position in the near-field of a sound source. This is easily observed from the exponential decay

of evanescent waves with respect to the distance from the source and the impact that a relative error in position has on the end result after back-propagation. However, for low resolutions on larger sources, the effects are less noticeable.

6.1.1   clamping unit small object

Step 1 (Figure 6.1) involves placement of the object of interest in front of the sensor system or placement of the sensor system in front of a source. The absolute area in between sensor(s) and source is defined. For small objects, this means placement in a clamping unit, a possible embodiment is schematically illustrated in Figure 6.2a, and the realized version is pictured in Figure 6.2b. Large objects are placed in front of the system and scanned with a distance measuring device (for example, a laser or an ultrasonic device). The clamping unit is fixed to the traverse unit of the measuring device that holds the acoustic sensory, by using a framework in which the object is clamped, the system "knows" where the object is located. This creates a space where the traverse system operates and the post-processing software calculates.
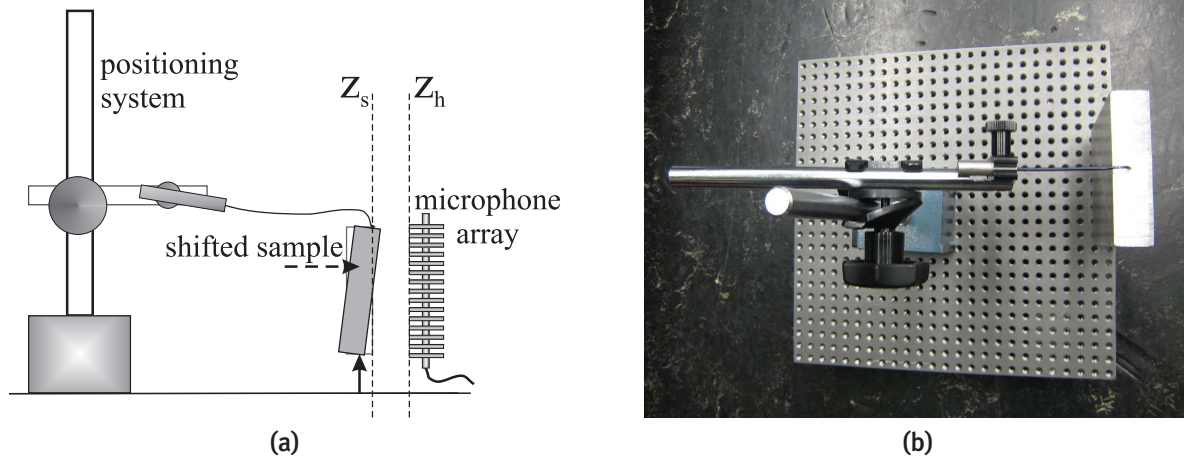
Figure 6.2: schematic drawing of a clamping unit for small objects (a) and a photograph of the realized clamping unit (b) with a steel base plate, positioning device with elastic element and an aluminum plate test sample at the right

6.1.2   hologram and source orientation

At first, the object placement with respect to the sensor array or traverse system may be fixed in order to define the absolute distance between the sensory system and the object. The orientation and exact distance of the sensory system may be used for accurate calculation of the NAH solutions. Figure 6.3a illustrates what happens when the object

is incorrectly oriented or placed with respect to the intended source plane. It is more problematic when the object enters the source free area, compared to a deflection of the source away from the source plane and further into the source half-space. The reason behind this is the over-estimation of the evanescent part, which is shown in Figure 6.3b.
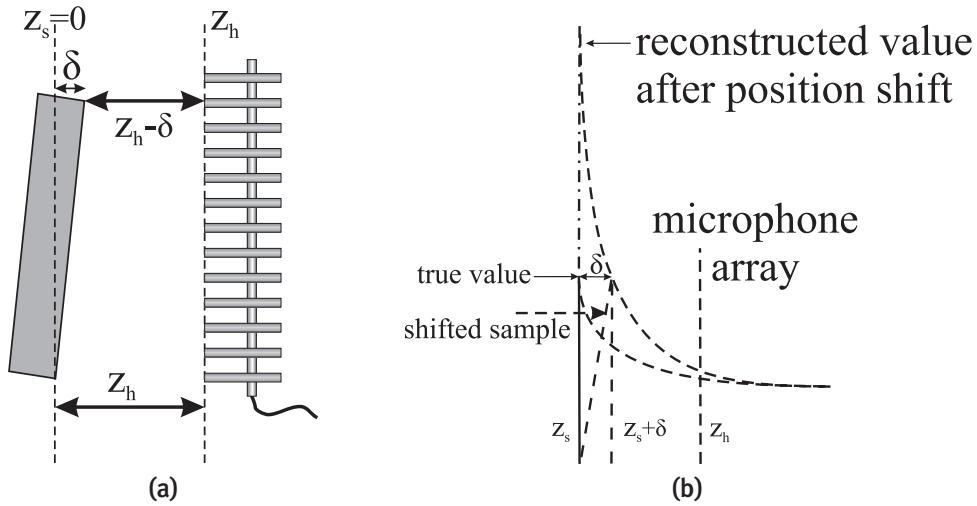
Figure 6.3: non-parallel orientation of sensor array with respect to the source plane (a) and an indication of the consequences with respect to the inverse propagator in an exponential manner (b)

After correct placement of the object with respect to the sensors, an area of interest and the required resolution of the acoustic images are selected. A built-in camera may be used to visualize the object, and the desired object-area selection is used to couple visual and acoustic information in an accurate manner, in order to identify acoustic sources.

6.1.3 optimal distance

In step 3 (Figure 6.1), a hologram (measurement) distance is determined through an automated process that provides an estimation of the signal-to-noise ratio (SNR) of the measurement. Based on this SNR figure, and the requested resolution by the user, an optimal hologram distance is calculated. The traverse system is automatically instructed to measure at this distance.

6.1.4 sensor positioning

In step 5, a traverse system automatically moves the sensor(s) over the desired measurement area. The traverse system is constructed in such a way that it minimizes acoustic

reflections, minimizes changes of acoustic impedance, etc. It is able to hold any type of sensor setting, for example single-point sensors, line arrays and full arrays of sensors. The resolution of the acoustic imaging system is highly dependent on the step-size of the traverse system and its accuracy. The sensory system may comprise acoustic sensors combined with optical sensors. The acoustic sensors include for example a microphone for sound pressure or a microflown for particle velocity measurements. The optical sensors are used to obtain a picture of the object of interest in order to couple acoustic radiation and sources to the visuals of the object. A CCD camera and a laser are able to provide this information.

6.2 Processing

In step 5, standard data-acquisition is used to properly transform all measured data into the digital domain (including anti-aliasing, A/D conversion, FFT, etc.). After the traverse system finished sampling all grid or hologram positions the resulting complex holograms, for a desired frequency band (step 6), are stored digitally.

In step 7, linear predictive border-padding, which is explained in chapter 3 in more detail, may be used to properly extrapolate the spatial data of the holograms in order to correctly transform into the wave-number domain where the inverse solution of NAH is determined. Linear predictive border-padding also enables the possibility to automatically drop out faulty measurement points and determine an optimal replacement based on surrounding data points. Besides that, various planes with multiple spatial sampling rates are combined, and missing areas are filled by means of border-padding. Lastly, border-padding makes NAH processing of sparse arrays practical and accurate, because the array data is extrapolated optimally, based on known data, and the process is extremely fast due to the use of FFT based methods. This method may also be used for real-time near-field sound imaging with hand-held and static arrays.

In step 8, the inverse solution is carried out in the wavenumber domain or k-space, as explained elsewhere in this description. This type of inverse solution is useful for accurate and very fast determination of the relevant information.

In step 9, regularization is automatically carried out in k-space by means of Cut-Off and Slope (COS) iteration or comparable methods, wherein the filter parameters may be determined without the need for extra information provided by the system operator.

In step 10, inverse two-dimensional FFT is performed. In step 11, the resulting spatial aperture is truncated, since the extrapolated parts, introduced with the border-padding procedure, are still attached to the outside borders of the calculated source aperture. In step 12, the resulting reconstructed sound information may be stored or displayed, optionally combined with the visual information.

6.3 Visualization

When the exact location of the source is known, the optical camera is used to automatically determine a picture of the source that exactly coincides with the measured acoustic aperture. Now, the resulting sound images are used to overlay the source picture in many different ways. From the inverse NAH processing calculation it is possible to visualize sound pressure, particle velocity and sound intensity in three dimensions between the source and hologram plane and also into parts of the far-field. Because the complex vectors are known on all these positions, it is possible to show auto spectra, real and imaginary parts of the three-dimensional sound field, and also the variations of the field over time. Visualization of the sound field over time is nicely shown in sound movies, which carefully capture the physical behavior of the acoustics in slow motion. These sound movies provide substantial insight for engineers into the behavior, origination and propagation of the sound sources.

6.4 Embodiments

A wide variety of add-ons and possibilities may be supported; the sensory system may include a combination of microphones, microflowns, lasers and/or cameras, these sensors may be operated as a single sensor, or in connected arrays with multiple sensors. When either the sensory system or the object is traversed over a pre-defined grid, one or more reference sensors or signals may be used to phase match all individual points. This helps to calculate a proper NAH solution and to visualize reconstructed acoustic data over time (may also be used in movies). Circumstances in an anechoic chamber may be optimal; on the other hand, measurements outside such a room are also possible thanks to the robustness of the post-processing methods. Besides passive measures, also active (background) noise cancelation may further improve the quality of the results in acoustically hazardous environments.

6.4.1 embodiment one: high-resolution robot controlled

Figure 6.4, along with Table 6.1 for a component listing, illustrates a single sensor, unbounded resolution system. Such a system often operates in an anechoic chamber for best results. However, due to the robustness of the system, measurements outside this room are also possible.

In the object area of the clamping unit an object of arbitrary size (given a large enough clamping unit) is placed. The clamping unit is specifically designed to fixate every sound emitting part of the object behind the source plane in order to fulfill the boundary conditions of the NAH method. The sensor body, which holds (in this case) a microphone

and a miniature CCD camera, is attached to a robot arm connected to the y-axis of the traverse system/robot that is able to move up and down. This construction is mounted on the x-axis of the traverse robot, which moves the system backward and forward in the x-direction, parallel to the hologram plane. The x-axis is connected to the z-axis, which moves the complete system in the z-direction, perpendicular to the hologram plane.
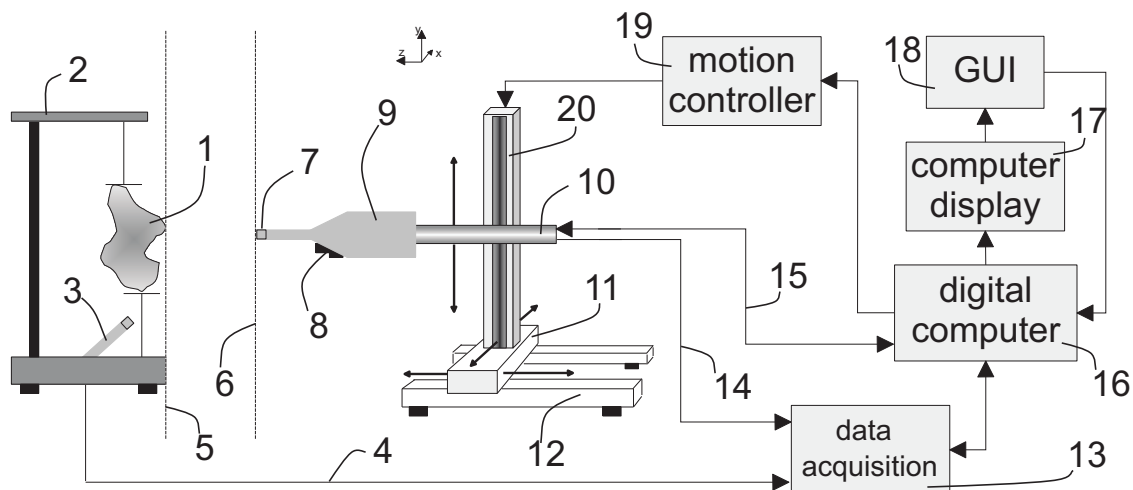

Figure 6.4: schematic overview of embodiment one: high-resolution robot controlled near-field sound imaging system

Table 6.1: list of components of embodiment one in Figure 6.4

1	object area	11	x-axis robot
2	clamping unit	12	z-axis robot
3	reference sensor	13	data-acquisition hardware
4	signal transport reference	14	control signal transport
5	source plane	15	signal transport hologram
6	hologram plane	16	computer
7	acoustic sensor	17	computer screen
8	camera	18	graphical user interface
9	sensor body	19	motion controller
10	robot arm	20	y-axis robot

The traverse robot is controlled by the software package in the computer and a motion control unit. The positioning algorithms are implemented in the software that controls motion and measurement simultaneously. The grid-size, desired spatial resolution and frequency band of interest are inserted by the user through interaction with the graphical user interface. Based on this information and noise conditions, the system automatically determines the optimal distance of the hologram plane, parallel to the source plane,

and calculates the positions the traverse robot moves the sensor in order to collect the required hologram data. The traverse robot may be arranged for traversing within an adaptive measurement plane, as set forth in the foregoing.

At a single hologram or grid position, the software in the computer collects sound pressure data from the microphone in the grid, image information from the camera and reference information from the reference sensor, in this case a microphone mounted on the clamping unit. The pressure signals are amplified and digitalized by the data-acquisition hardware, which sends the measured data to the computer. The computer also collects the image data through a wire connection and the system software processes all data as described earlier; results are displayed on the computer screen, which are editable by interaction with the graphical user-interface.

This embodiment is built and operational in the semi-anechoic room at the Mechanical Engineering Department of the Eindhoven University of Technology, also see the picture of the set-up provided earlier in Figure 5.1. This version is easily packed and is supported by wheels to allow for easy movement of the high-resolution system to other sites for outside measurements. The detailed properties of the system are provided in Table 6.2.

Table 6.2: high-resolution near-field sound imaging triple axis traverse system

high-resolution traverse system		
number of axis	3	
x-axis	range: 70 cm	resolution: 11 μm
y-axis	range: 70 cm	resolution: 11 μm
z-axis	range: 90 cm	resolution: 13 μm

6.4.2   embodiment two: portable line-array

Figure 6.5, along with Table 6.3 for a component listing, illustrates a portable line-array system for small objects. This system is comparable to the primary embodiment with a small number of significant changes. First of all, this embodiment is portable and focused on smaller objects (20 cm^3) for a frequency range between 600 Hz and 20 kHz. The system is placed in a small anechoic box and generally uses an array of sensors instead of a single sensor. This system is easily placed in a small laboratory or a production facility, where smaller objects are produced or investigated that require high resolution source identification.

 The object of interest is placed in a flexible clamping unit that holds a number of octopus arms capable of grabbing the object. The object is placed behind a glass plate that coincides with the source plane, after fixation of the octopus arms the glass plate is removed. The distance between source and hologram plane is now defined and is only changed by moving the clamping unit base backward and forward. The sensor line-array, with
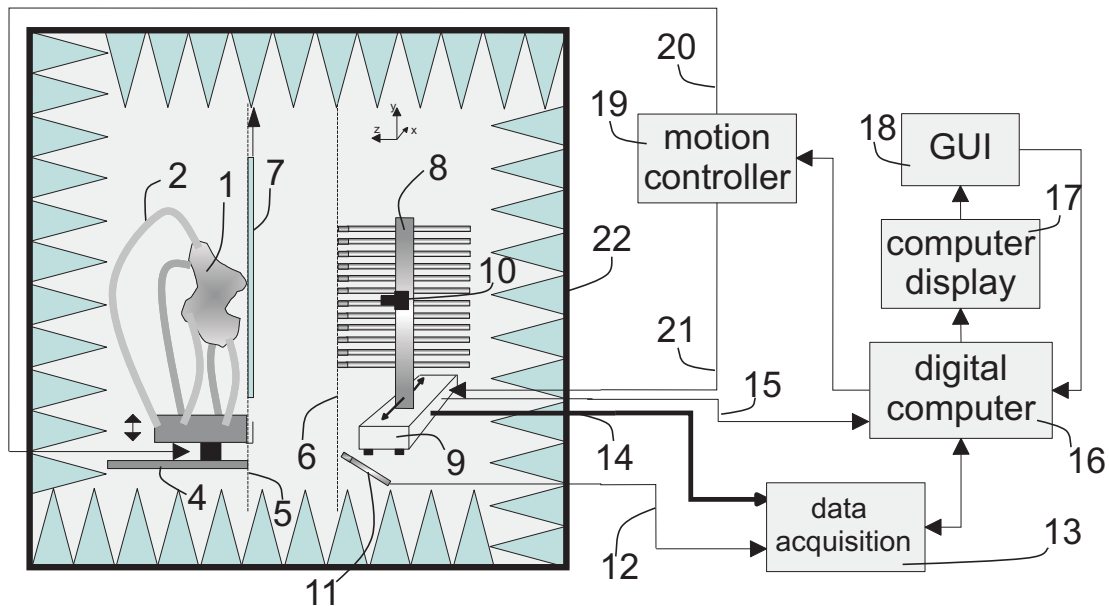
Figure 6.5: schematic overview of embodiment two: portable line array near-field sound imaging system

Table 6.3: list of components of embodiment two in Figure 6.5

1	object of interest	12	signal transport reference
2	flexible clamping unit	13	data-acquisition hardware
3	vertical movement frame	14	multi-channel signal transport
4	mounting base	15	video signal transport
5	source plane	16	computer
6	hologram plane	17	computer screen
7	reference plate	18	graphical user interface
8	line sensor array	19	motion controller
9	x-axis motion system	20	control signal transport
10	camera	21	control signal transport
11	reference sensor	22	portable anechoic chamber

microphones placed in vertical direction, is mounted on a traverse system that moves in the x-direction, parallel to the hologram plane. The CCD camera that is mounted on the line-array is used to capture the image of the measured object. The clamping unit is moved in vertical direction with respect to the base, parallel to the source plane. To capture the correct phase as the array moves to different hologram positions, a reference signal is measured from the static microphone mounted in the box. The measurement and processing procedure is similar to the system described as the primary embodiment of Section 6.4.1, only the motion control is different. The motion controller moves the line-array over the x-axis to collect all grid measurements in a single row of the hologram. To access the next row, the motion controller operates the clamping unit up or down,
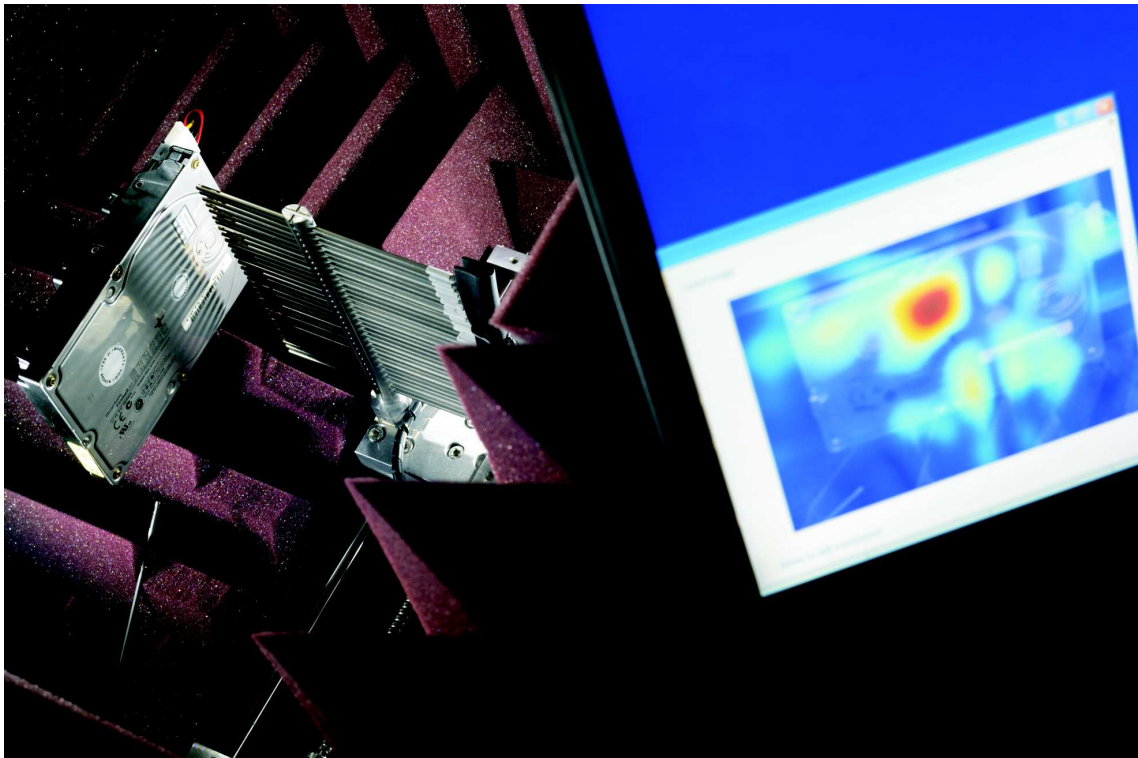
photograph by Bart van Overbeeke

Figure 6.6: picture of realized portable line array near-field sound imaging system in an anechoic box

again a complete row is covered by controlling the x-axis movement as described.

The second embodiment is also realized in real-life, which is shown in the photograph given in Figure 6.6. This particular system is capable of providing near-field sound images within a few minutes time, which depends on the object size and desired resolution, and fully automatically. The system is easily moveable and aimed at small objects within a 20 by 20 cm hologram or aperture size and, currently, a maximum spatial sound image resolution of $SSIR = 5$ mm. The line array contains 31 Sonion 8002 microphones and one reference microphone, but it is also possible to increase the number of reference microphones, which will lower the number of microphones in the line array consequently. Two 11-wire shielded cables are used to transport the signals to a 32 channel pre-amplifier, which is connected to four Soundscape iBox 8-line A/D converters. The A/D converters are coupled to two Soundscape Mixtreme 192 PCI cards in the post-processing PC system by TDIF cabling. The ANSITE processing software is used to process the holograms and it also controls the traverse system, which is mounted in the anechoic box and driven by a Maxon spindle motor system.

6.4.3   embodiment three: double-layered full array

Figure 6.7, along with Table 6.4 for a component listing, illustrates a portable double-layered array, which is suitable for use in acoustically hazardous areas. The portable double-layered array is a hand-held array that is possibly used in acoustically hazardous areas, like a factory hall or interior of an automobile.

This full array is positioned by hand or placed in a stand or on a traverse system. The full array is positioned in front of a sound emitting structure. The hologram distance is determined by an ultrasonic system, or by a laser triangulation system implemented in the array. The source plane is defined by a part of the object which is closest to the array and parallel to the hologram plane. Again, the source-free area between source and sensors is defined and a measurement is conducted.
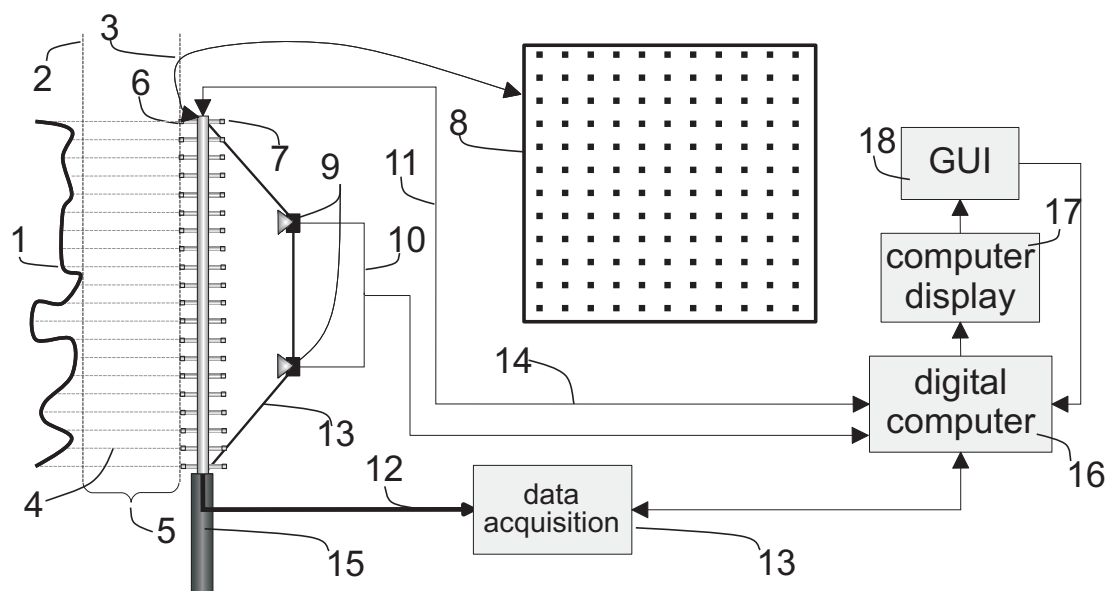
Figure 6.7: schematic overview of embodiment three: portable double-layered array

Table 6.4: list of components of embodiment three in Figure 6.7

1	object contour	10	video data transport
2	source plane	11	positioning signal transport
3	hologram plane	12	signal transport hologram
4	contour detection	13	data-acquisition hardware
5	standoff distance	14	source contour signal transport
6	front layer sensor array	15	grip
7	back layer sensor array	16	computer
8	array frame	17	computer screen
9	stereo camera vision	18	graphical user interface

The measurement of the double-layered array is carried out through parallel channels by the multi-channel data acquisition system. The necessary source image data is collected by a stereo view camera combination, which is used to filter out the sensors that block the visual source image. NAH data-processing is conducted equally to the primary embodiments. However, obtaining the correct holograms for the desired frequencies is different. The back layer of sensors combined with the front layer of sensors is used to differentiate between sound originating from the front and the back. Subsequently, the signals from the back of the array are subtracted from the signals originating from the front (source) of the array, thus the desired hologram is obtained.

This type of set-up potentially supports real-time NAH, because of the extremely fast data-processing algorithms. In all embodiments, but particularly useful in this system, the use of wireless data collection improves handling and flexibility. Communication through connections marked by 10, 11, 12, and 14 in Figure 6.7 then become wireless.

6.5 Conclusions

The ANSITE system provides accurate, automated sound field visualization. The sound imaging system helps localize and analyse sound sources in existing and new products. Such a system can be operated by a non-expert in the field of acoustic measurements, although some training may be required. The system can be used to measure e.g. small objects like a mobile phone, large objects like a truck, and everything in between. A large variety of acoustic source information and visualization is obtainable. Examples are sound pressure, particle velocity and sound intensity in three dimensions between the source and hologram plane, and also into parts of the far-field. This allows for acoustic overlays of the source image, radiation from the source into the far-field, total radiated sound power, and so on. Possible system configurations include: Serial single sensor, line or full-sensor array measurement over a pre-defined grid with a traverse robot and an object in a special clamping unit in or outside an anechoic room; A static or portable full array measurement with sensors able to determine the distance to the object in front of the array. The industrial application of a number of these sound imaging system embodiments is shown in the next chapter.

Industrial Applications of Sound Imaging

The practical application of NAH is significantly improved with the development of AN-SITE, especially due to the implementation of border-padding and regularization tools based on the methods discussed in chapter 4. The validation of specific parts of the system are already described in chapter 5, here the various embodiments of the ANSITE system are tested in industrial practice. Three different cases are shown. The first case consists of a small aperture at a relatively high resolution on the top cover of a hard disk drive. The inverse solution at the source is compared to laser vibrometer tests on the surface. Secondly, an industrial research setup with a dynamical buckling cylinder is treated, which is used to verify dynamical models and observe the structural vibrations. Finally, a large scale industrial case with a hydraulic diesel generator illustrates the possibilities of the system in noise source detection, behavior and insight into possible solutions.

7.1 Hard disk cover vibrations

The first industrial application of sound imaging technology is performed on a standard electronic component used in personal computers, laptops, video recorders, etc.: the hard disk drive. This case is considered as an example for a large range of small electronic devices that were already tested during this research and are suitable for tests with the sound imaging system. Examples of these small electronic devices are cell phones, computer components, displays, cooling fans, navigation equipment, printed circuit boards, etc. In this particular case, a Quantum Fireball LCT10 hard disk drive is used to illustrate some of the possibilities for visualization and identification. Also, the inverse calculation from a pressure hologram to normal particle velocity on the top cover surface of the hard disk drive is compared to laser vibrometer measurements. This makes it possible to qualitatively, as well as quantitatively, analyse the performance of the ANSITE system

compared to a laser vibrometer.

7.1.1 measurement set-up

Embodiment one, which is described in Section 6.4.1, is used as the basic measurement setup for the Quantum Fireball LCT10 hard disk drive measurement case. Figure 7.1 shows the hard disk drive mounted on a black aluminum stand that holds the metal drive cover in a vertical direction, while facing the traverse system.
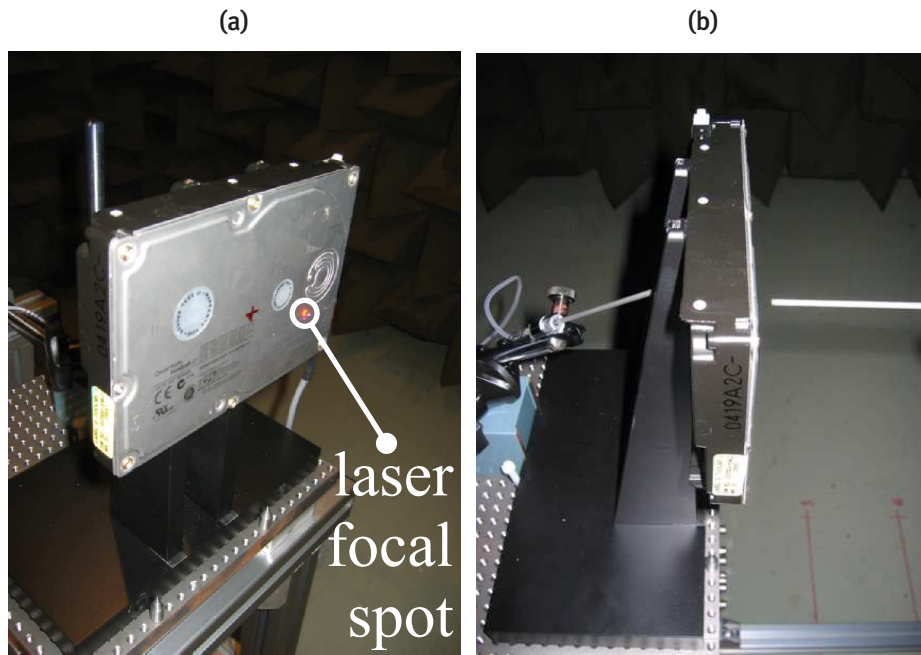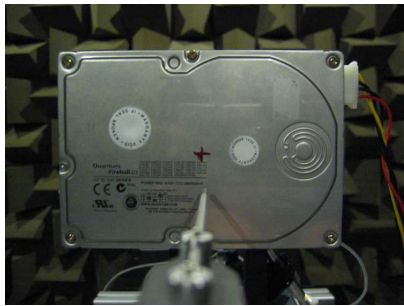

Figure 7.1: a: measurement setup of the hard disk drive that is vertically mounted on a black aluminum stand in a semi-anechoic room, the laser vibrometer samples the metal top cover; b: the hologram is spatially sampled by a single miniature Sonion 8002 microphone at $z_h = 1$ cm (to the right) mounted on a traversing beam, a reference microphone is positioned near the bottom (left side in this picture) of the hard disk drive

A Polytec OFV-5000 laser vibrometer with an OFV-511/512 sensor head is mounted on top of the microphone beam of the three-dimensional traverse system. The laser scans an equidistant grid on the top cover of the hard disk drive, which is shown in Figure 7.1a. Secondly, the same grid points of the laser measurement are used for the holographic acoustic measurements where the microphone is positioned at a standoff distance of $z_h = 1$ cm, which is shown in Figure 7.1b. The microphone that is positioned at the back of the hard disk drive and to the left of the picture in Figure 7.1b is used as a phase reference for both the laser vibrometer and the hologram microphone.
In order to fully test the potential of the ANSITE system, the same sparse measurement

aperture is used for the laser and the acoustic hologram measurements, contrary to general NAH measurements where often an aperture much larger than the source of interest is chosen. The hard disk drive is 10.1 cm in vertical and 14.7 cm in horizontal direction in the current setup, while the measurement aperture height is only 7.5 cm and the aperture width is 12.5 cm with a minimum sensor spacing of 5 mm. In this case the minimum sensor spacing is chosen first. Based on that choice, (2.23), the SNR and a save estimation the EPR, a standoff distance z_h results. All necessary parameters of this measurement are provided in Table 7.1, including a photograph of the scanning microphone in front of the hard disk drive.

Table 7.1: hard disk drive measurement parameters

source: hard disk drive Quantum Fireball LCT10 (idle spinning)		
total aperture height	$Y = 7.5$ cm	
sensors in vert. dir.	$M = 15$	
min. vert. sensor spacing	$\Delta y = 5$ mm	
total aperture width	$X = 12.5$ cm	
sensors in vert. dir.	$N = 25$	
min. hor. sensor spacing	$\Delta x = 5$ mm	
standoff distance	$z_h = 1$ cm	
total hologram positions	$N \times M = 375$	
frequency band	$0 - 10$ kHz	
set-up:		
2 Sonion 8002 microphones, 2 channel matched pre-amplifier		
Polytec OFV-5000 vibrometer controller, OFV-511/512		
3D high-resolution traverse system, 4 channel Siglab analyser		
Intel duo core WinXp system with $Matlab^{\text{TM}}$ 7.4		

7.1.2 results

The vibrational velocity of the top cover in normal direction is measured by the laser and compared to the inverse calculation of the normal particle velocity at the hard disk surface which follows from the sound pressure hologram at a standoff distance of $z_h = 1$ cm. The measured aperture is marked with the dashed rectangle on the hard disk cover picture, which is shown in Figure 7.2a. The sound pressure hologram for the frequency of interest $f_s = 1075 Hz$ is plotted in Figure 7.2b.

Often, peaks in the average sound pressure spectrum represent the most interesting frequencies for the analysis of vibration and acoustic noise generated by products. One of the peaks is situated at $f_s = 1075$ Hz and is chosen here to further process and investigate with the ANSITE software.
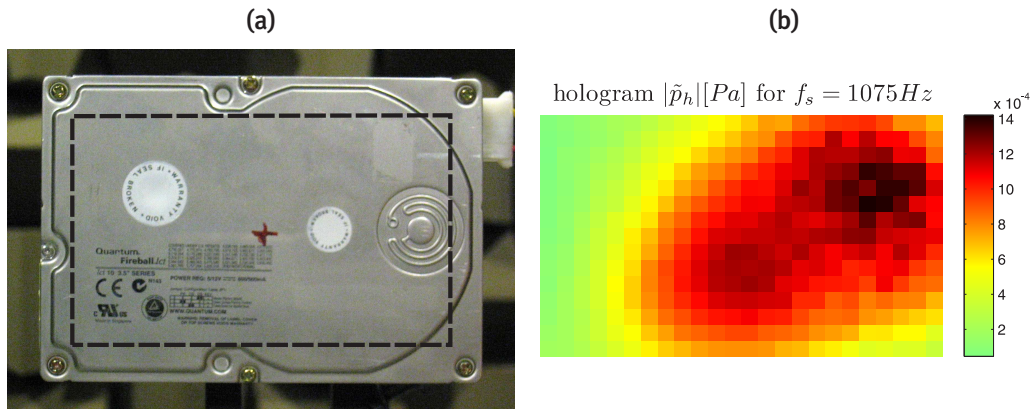
Figure 7.2: photo of the hard disk cover with a dashed rectangle that marks the microphone and laser aperture (a) and the sound pressure hologram at $f_s = 1075$ Hz (b)

The calculation of the inverse solution, from the sound pressure hologram to normal direction particle velocity on the hard disk cover, includes eighth order linear predictive border-padding with various types of filter functions and stopping rules. In Figure 7.3, three columns with results are shown, the left and right column are reconstructed particle velocities which are obtained from PNAH, and regularization based on L-curve and GCV type stopping rules respectively. The center column is reserved for the measured laser vibrometer velocities of the cover, the source velocity image is copied for all rows in order to conveniently compare these with the PNAH results. Notice that all images have their own scaling and thus pay attention to the color bars for the quantitative analysis.

The GCV stopping rule (also in combination with the COS iteration) either over- or under-regularizes, which results in a poor SSIR (see Figure 7.3b3, c3, e3, and f3) or in sound images with heavy noise blow-up (see Figure 7.3a3 and d3). This is in agreement with similar results found in the numerical and controlled experiments in chapter 4 and 5, which illustrates that the GCV stopping rule is undesirable in industrial practice.

On the other hand, the L-curve stopping rule performs much better and much more consistent (as shown in the first column of Figure 7.3) compared to the GCV. The truncation filter results in Figure 7.3f1 show the largest quantitative (over-estimated velocities) and qualitative errors compared to the laser velocities in Figure 7.3f2. The qualitative results for the exponential (b1), modified exponential (c1), Tikhonov (d1) and modified Tikhonov (e1) filter are comparable to, and very well matching with, the laser velocities in the center column of Figure 7.3, although quantitatively, the exponential filter performs somewhat better.

Finally, the COS iteration stopping rule with ζ-criterion automatically determined a modified exponential filter with $k_{co} = 117\frac{rad}{m}$ and a slope ratio $\phi = 1$ with a resulting normal particle velocity image that is shown in Figure 7.3a1. This result compares very well, both quantitatively and qualitatively, to the laser image. Also, the linear predictive border-padding performs very well since the errors around the edges are minimal when the
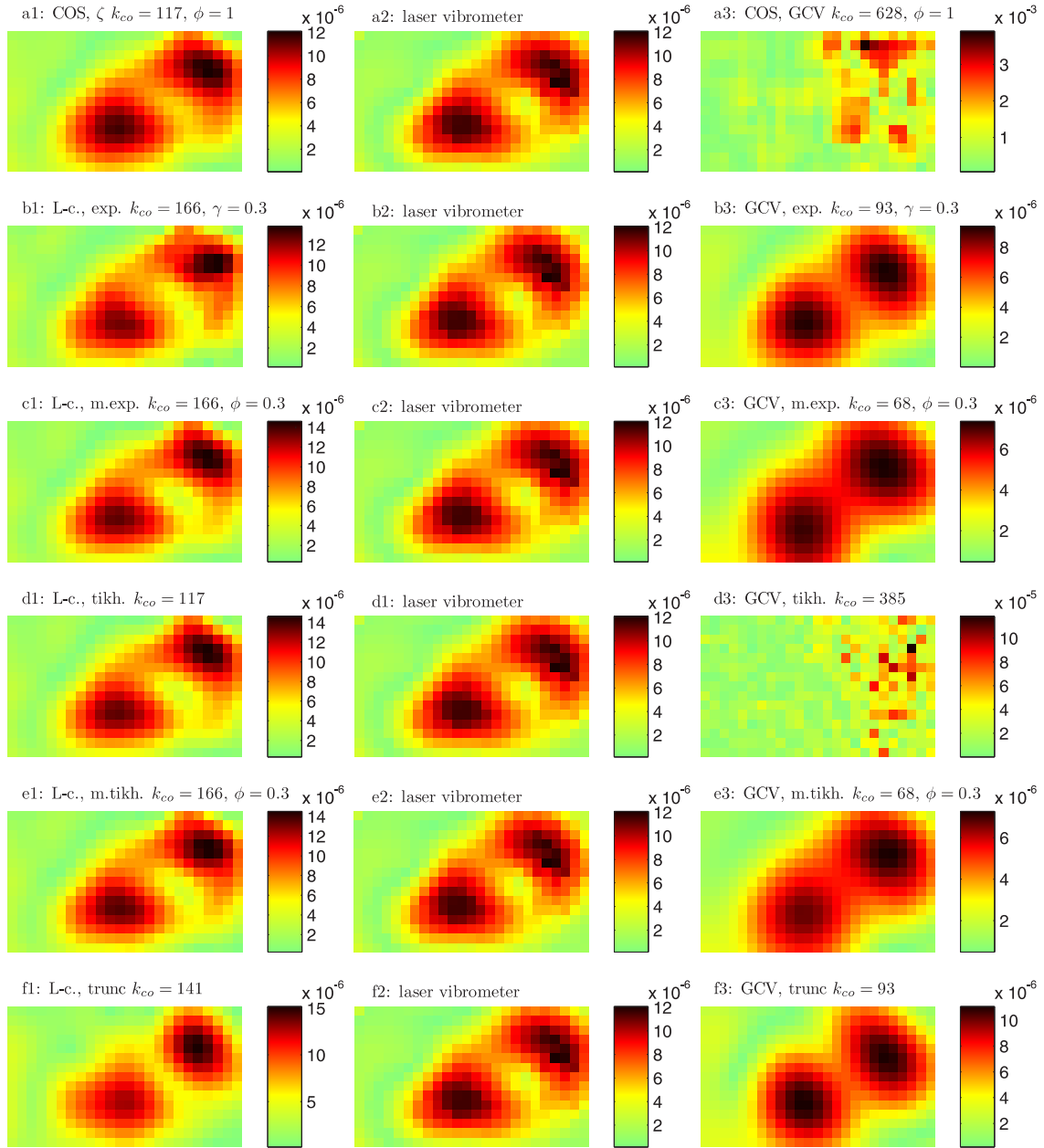
Figure 7.3: hard disk drive sound source images of $|\tilde{u}_z(x,y)|$ [m/s] at $f_{s2} = 1075$ Hz for various types of filter functions and stopping rules with PNAH (left and right columns) and the laser vibrometer (center column)

correct regularization is applied. These results illustrate the practicability and high performance of border-padding and regularization by means of COS iteration in a typical high-resolution, automated industrial case study.

7.2 Dynamical behavior of a cylinder

The previous section shows that near-field sound imaging is a powerful analytical tool for visualization of sound radiation from, and estimation of vibrations of, dynamical structures. Now, this tool is used in a cylindrical setting in the experimental validation of the results from (28; 27). Therefore, a close collaboration between STW projects 05792 on "dynamical buckling of thin-walled structures" and 06618 on "inverse acoustics", of which this thesis is part of, has been established. The object of interest is a dynamically loaded cylindrical shell with a top-mass. For this reason, Cylindrical NAH (CNAH) is implemented in the ANSITE software package. It is the first time that an NAH system has been used for this kind of dynamical system. Some of the possible visualization and calculation options for such structures are observed and explored in this section.
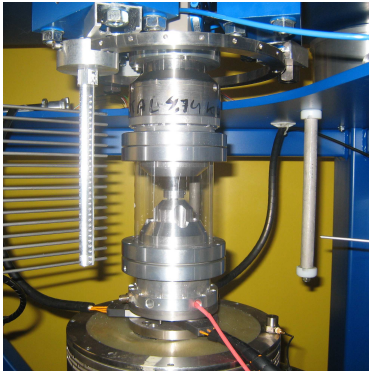
7.2.1 measurement set-up

Up to now, the implemented and explored NAH process is based on a planar geometry. Now, the cylindrical geometry is used, because the cylindrical shell requires a different geometry to visualize the vibrations and pressure variations on the source surface properly. The basic idea of the inverse solution with NAH is the same, only now the inverse propagator is calculated from a hologram cylinder to a source cylinder.

Before the inverse solution is calculated the sound pressure hologram is measured. The center of the transparent polyethylene terephthalate (PET) cylinder with a radius of $r_s = 4.4$ cm is the center around which a microphone line array rotates at a hologram radius of $r_h = 8.7$ cm. The specific details of the measurement are provided in Table 7.2, including a photograph of the aluminum microphone line array (left) in front of the PET cylinder and the shaker at the bottom. The microphone line array has 15 Sonion 8002 microphones above each other with a minimal sensor spacing of 1 cm.

The construction around the PET cylinder is used to mount the microphone array on. The maximum required number of observable wavelengths in circular direction is set to 12, which results in steps of $15°$ in a circular direction of the microphone line-array. Again, the resulting spatial sampling wavenumber, the SNR and an estimation of the EPR are used to determine a save hologram distance from (2.23).

A spatially stationary reference microphone provides the necessary phase information in order to link the separate lines of sound pressure into a single complex sound pressure hologram cylinder. Now that the hologram cylinder is available, the inverse solution is calculated. The process steps are very much the same as the PNAH process, the main difference is the inverse propagator, which is based on Hankel functions. The CNAH process and inverse propagation function for external cylindrical problems is extensively described and derived in (56). Linear predictive border-padding is only applied in the vertical direction and not in the circumferential direction since the first and final line array

Table 7.2: cylindrical NAH measurement parameters of dynamical buckling cylinder structure

source: dynamical buckling PET cylinder		
total aperture height	$Y = 15\,\mathrm{cm}$	
sensors in vert. dir.	$M = 15$	
min. vert. sensor spacing	$\Delta y = 1\,\mathrm{cm}$	
hologram circumference	$X_r = 54.7\,\mathrm{cm}$	
minimum horizontal angle	$\phi = 15°$	
sensors circumferential dir.	$N = 24$	
radius hologram cylinder	$r_h = 8.7\,\mathrm{cm}$	
radius source cylinder	$r_s = 4.4\,\mathrm{cm}$	
total hologram positions	$N \times M = 360$	
frequency band	$0 - 3\,\mathrm{kHz}$	
shaker excitation frequency	$180\,\mathrm{Hz}$	
set-up:		
16 Sonion 8002 microphones, 16 channel matched pre-amplifier		
16 channel Soundscape iBox A/D converters		
2 Soundscape Mixtreme 192 PCI cards with TDIF interface cables		
Intel dual core WinXp system with $Matlab^{\mathrm{TM}}$ 7.4		
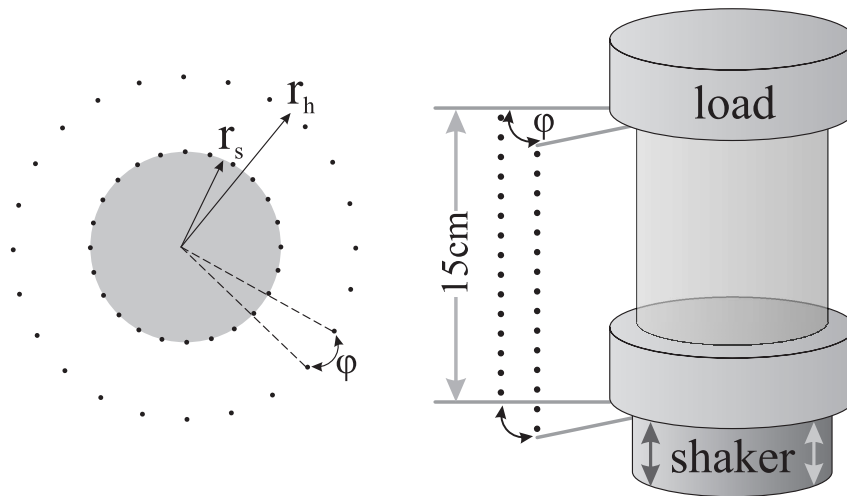
Figure 7.4: CNAH cylinder setup with the hologram and source cylinder top-view at the left and the schematic cylinder drawing including the shaker and load at the right

measurements connect smoothly, which poses no problems for the spatial FFT in terms of leakage. All regularization is performed by the COS iteration in combination with a modified exponential filter.

(a) shaker excitation frequency $f = 180$ Hz

(b) $f = 541$ Hz

(c) $f = 901$ Hz

(d) $f = 1261$ Hz
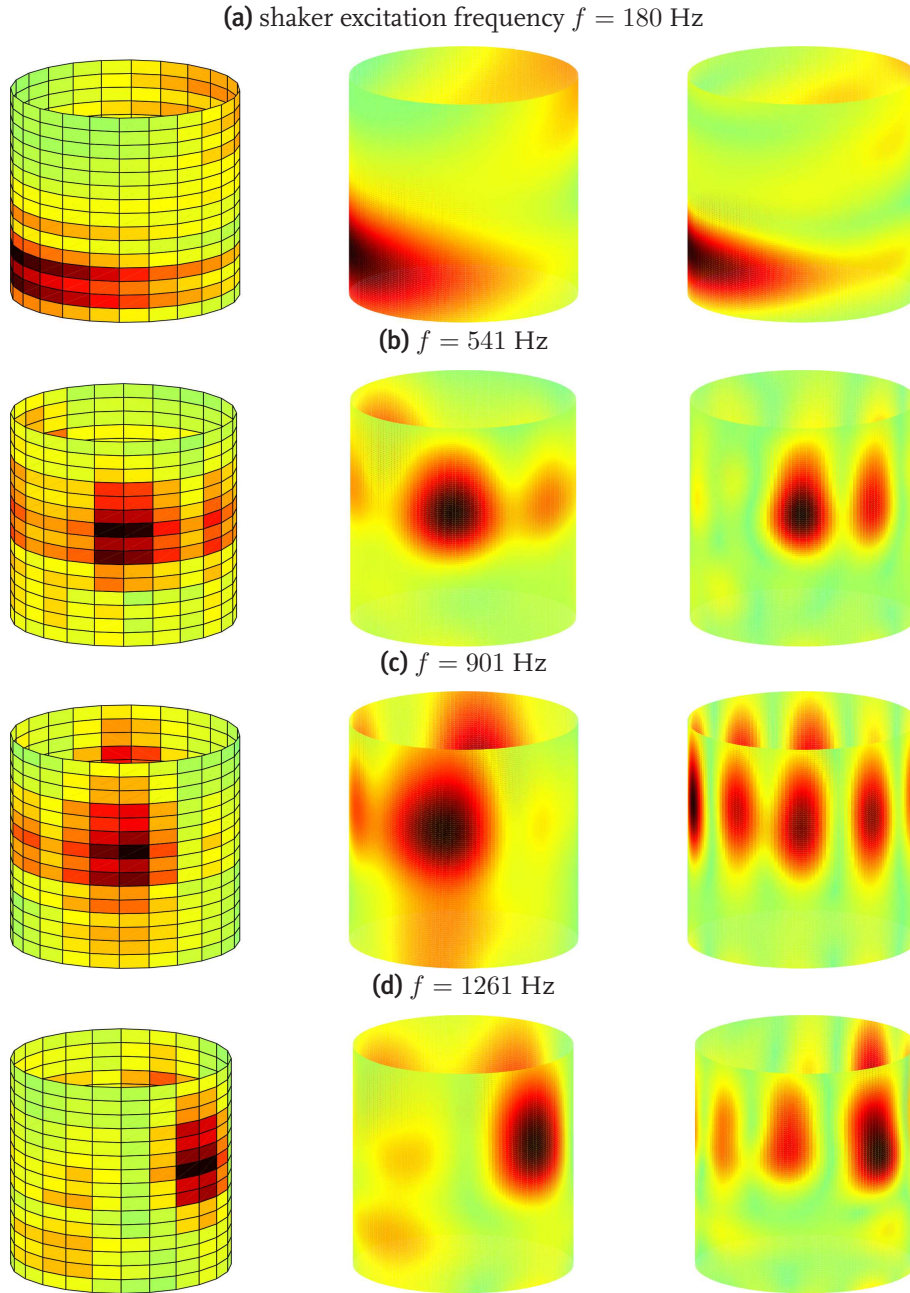
Figure 7.5: cylinder measurement at $r = r_h$ (left), $|\tilde{p}(\phi, y, r_h)|$ hologram (center), $|\tilde{p}(\phi, y, r_s)|$ source image (right) for four different frequencies

7.2.2 results

The cylinder base is excited by the shaker at an excitation frequency of 180 Hz. At this frequency, stationary vibrational patterns emerge from the PET cylinder surface and the radiated sound pressure fluctuations are registered by the microphone array. For some of the peak frequencies, the measured sound pressure amplitudes are shown in the left column of Figure 7.5. After inverse CNAH processing, the sound pressure distribution

at the source cylinder at $r = r_s$ is visualized in the right column of Figure 7.5. The results for the excitation frequency of 180 Hz in Figure 7.5a show a non-parallel interaction between the shaker and cylinder base, which results in a 'wobble' in the PET cylinder. This behavior was unexpected and not taken into account in the dynamical model. The other peak frequencies show circular deflection shapes that partly match the shapes following from the dynamical model. At $f = 901$ Hz in Figure 7.5c, a clear standing wave pattern is visible, which includes five full waves. This result on the source seems odd, because the hologram contains two clear maxima, while the source image has a standing wave pattern. This is a nice illustration of the resolution improvements obtained by NAH: the lower wavenumbers hardly get boosted in the inverse propagation, while the higher wavenumbers are upgraded significantly above the low wavenumbers shown in the hologram.

Application of CNAH sound imaging on a dynamically loaded thin-walled cylindrical structure successfully visualized circular deflection shapes on the cylinder surface and provided much insight into the problem. Also, a flaw in the experimental set-up was uncovered, which was due to the wobbling, non-parallel shaker excitation of the cylinder base. Future work includes the installation of a new shaker and the application of a full cylindrical microphone array. A full array makes it possible to investigate beating (28) and other non-stationary effects, required for proper validation of the buckling models. Also, more extensive validation of the results is required for a better understanding of wave patterns and behavior of the cylinder walls and possible imperfections of the structure itself, which possibly cause mixed modes and unpredicted disturbances. In conclusion, near-field sound imaging shows great potential for further analysis and future dynamical model analysis and verification for this type of research.

7.3 Large scale construction equipment

The final case in this series illustrates the wide applicability of the technique and expands the high-resolution methods to a much larger scale and lower spatial sound image resolutions. Also, this is an example of a typical industrial case in search of the strongest noise sources and their behavior. Eventually, the sound imaging technology is used to help counter these noise sources and be able to measure and predict the consequences of anti-noise measures. More specifically, the source of interest is a hydraulic diesel generator of International Construction Equipment (ICE) used to drive large vibrator hammers for the construction industry. Measurements are performed outside, at three sides of the machine, and at different engine power levels.
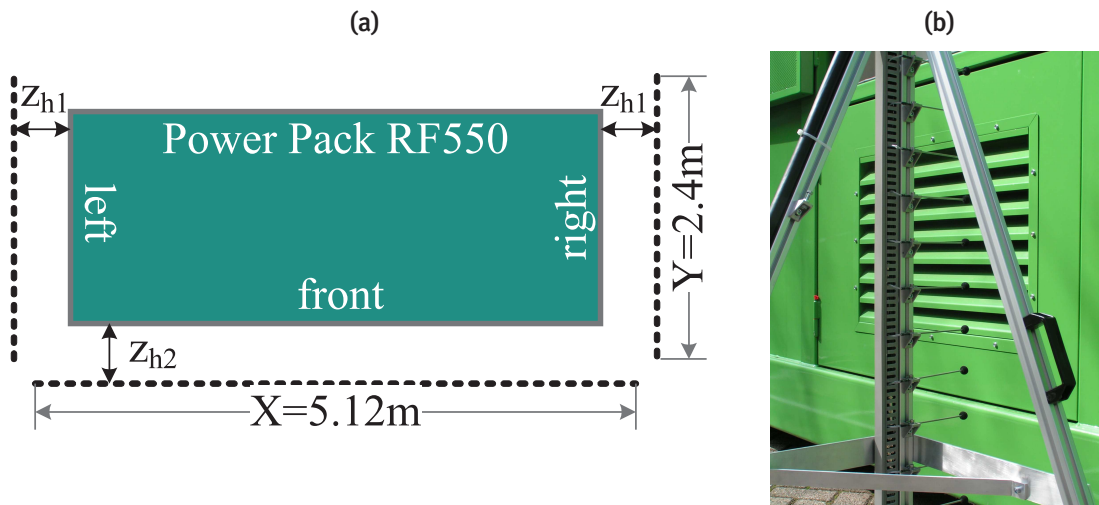
Figure 7.6: schematic top-view of the generator and the hologram positions surrounding it (a) and a close-up of the line array with Sonion 8002 microphones (b), the wind caps are applied for the outside measurements

7.3.1 measurement set-up

In this case, the ICE hydraulic generator Power Pack RF550 drives a hydraulic load at 80 percent power (1860 rpm) which results in 290 bar hydraulic load pressure. Sound pressure holograms at three sides of the generator are measured with a 2.5 m line array that is moved in horizontal direction over rails. Figure 7.6a shows the schematic measurement setup with the generator in the center, which is flanked on three sides by the hologram positions marked by the small rectangles. The used measurement set-up is considered a large scale and non-anechoic version of embodiment two from section 6.4.2, with a 31 channel line array and one spatially stationary microphone used as phase reference. The environmental disturbances are neglected since the high near-field sound pressure levels and the temporal averaging are believed to largely overrule these propagating effects. The qualitative information is focussed in the near-field of the sound source. Also, disturbances that are caused by the wind are suppressed by the wind caps shown in the close-up of the microphone array in Figure 7.6b.

More details on the measurement settings are provided in Table 7.3, which shows that the spatial sampling is performed at 8 cm intervals and two different standoff distances for the front and both sides. A rather large step-size is chosen, because there are 31 sensors available and a coarse overview of the complete system is requested in this case. The front side standoff distance is larger compared to the sides in order to minimize possible aliasing problems based on (2.23), because the sound pressure levels at the front side are considerably higher compared to the sides. The line-array should be carefully aligned with respect to the source plane of the generator. The large size of the complete measurement set-up allows small errors, which is due to the relatively small impact of

Table 7.3: large scale NAH measurement parameters of ICE hydraulic generator Power Pack RF550

source: ICE hydraulic generator Power Pack RF550		
total aperture height	$Y = 2.48$ m	
sensors in vert. dir.	$M = 31$	
min. vert. sensor spacing	$\Delta y = 8$ cm	
total aperture width (sides)	$X = 2.4$ m	
sensors in hor. dir. (sides)	$N_s = 30$	
total aperture width (front)	$X = 5.12$ m	
sensors in hor. dir. (front)	$N_f = 64$	
min. hor. sensor spacing	$\Delta x = 8$ cm	
standoff distance (sides)	$z_{h1} = 30$ cm	
standoff distance (front)	$z_{h2} = 40$ cm	
total hologram positions	$N \times M = 3844$	
frequency band	$0 - 3$ kHz	
set-up:		
32 Sonion 8002 microphones, 32 channel matched pre-amplifier		
32 channel Soundscape iBox A/D converters		
2 Soundscape Mixtreme 192 PCI cards with TDIF interface cables		
Intel duo core WinXp system with $Matlab^{TM}$ 7.4		

minor positioning errors. The frequency band of interest is relatively low, because the main problem area is in the range of 50 to 500 Hz, while at higher frequencies there are no evanescent waves available for this SSR.

7.3.2 results

In this case, the first step in the identification of the main sources of disturbance is to pick out a number of the highest peaks from the spectrum and calculate various sound images of the source. First, the main peak of three times the engine speed at $f_{s1} = 93$ Hz is observed ($3 \cdot \frac{1860}{60} = 93$). The sound pressure distribution at the source planes at both sides and the front is plotted over time, which is normally shown in a movie on the computer screen. As an alternative to the movie, the spatial source images are plotted for a number of time steps for all sides in Figure 7.7.

To calculate the time step images, small positive phase changes are made for the complex sound pressure values over the whole aperture. The bottom image set connects to the top image set so an impression of the wave propagation around the source is obtained. From these images it is clearly visible that the acoustic source is the exhaust, which is located at the top of the generator pack, marked by the gray circle. It also shows that sound waves at these low frequencies expand in all directions and also reach the operator and construction site personnel in the immediate surroundings.

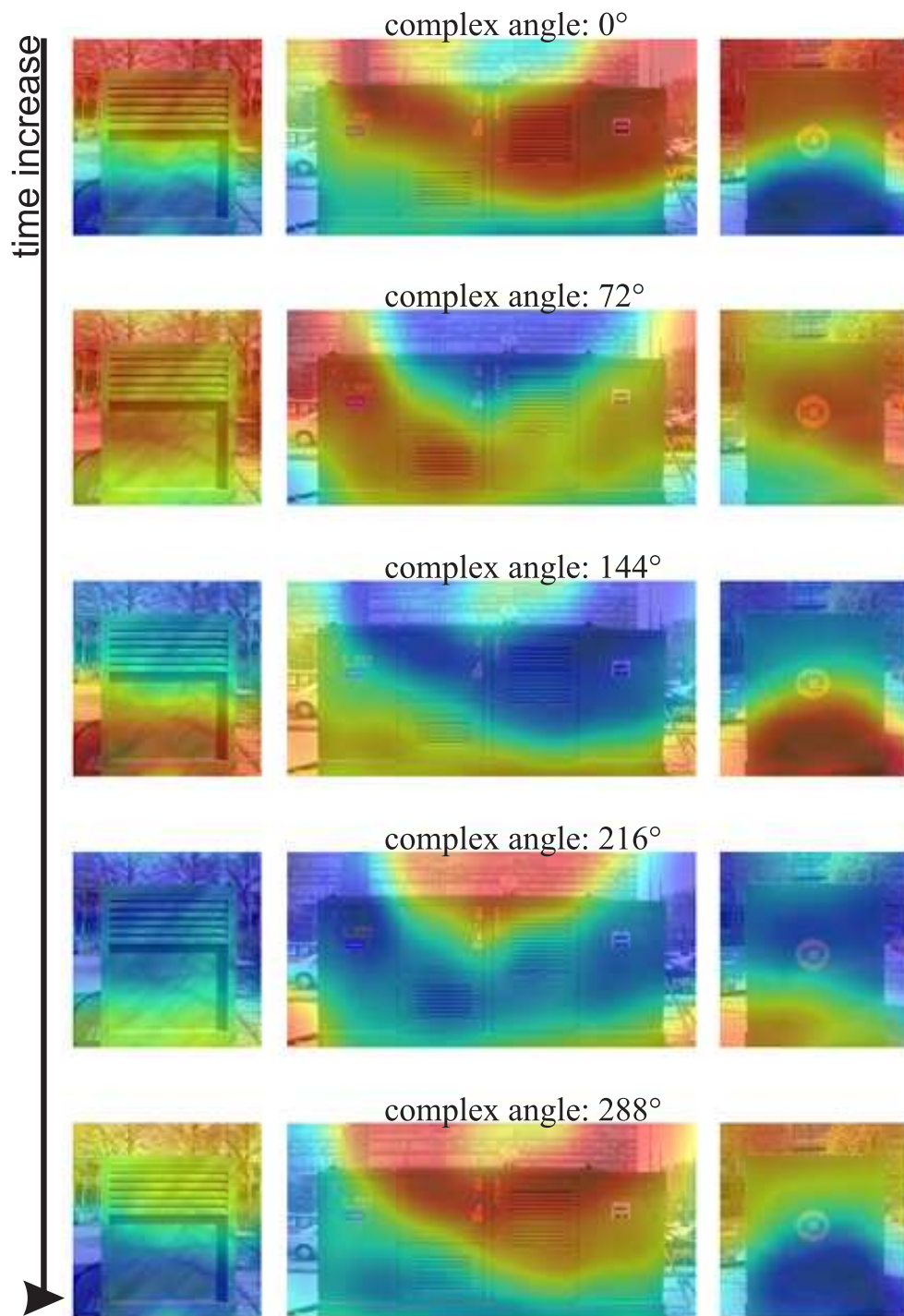**Figure 7.7:** time variant sound pressure source images of ICE hydraulic generator Power Pack RF550 at $f_s = 93$ Hz for three sides (left, front and right)

The next two highest peaks from the spectrum are situated at $f_{s2} = 279$ Hz and $f_{s3} = 353$ Hz. Figure 7.8 shows the sound intensity in normal direction, which is also obtained from the PNAH calculations performed on the measured sound pressure hologram. Fig-

(a) f_{s2} = 279 Hz, 80% load; leaking or vibrating door edges
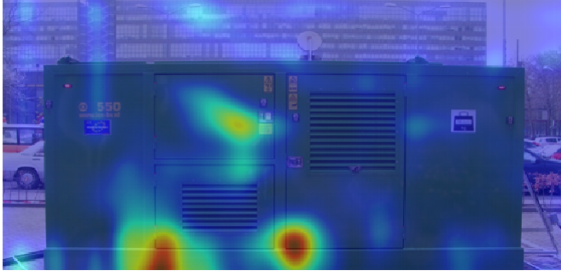
(b) f_{s3} = 353 Hz, 80% load; transmission through ventilation bracket
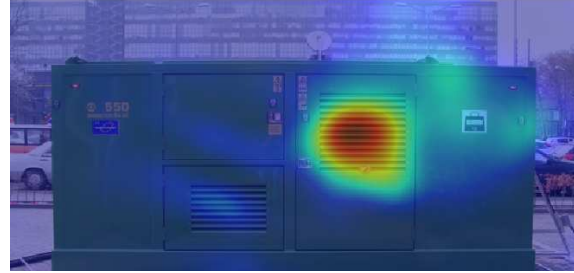

Figure 7.8: normal sound intensity images (red is high intensity, blue refers to low sound intensity) of the front side of the ICE hydraulic generator Power Pack RF550

ure 7.8a shows the areas where most sound power is radiated from or through the construction. Here some areas near the lower corners of the doors are either leaking or vibrating, which causes the high sound intensity in these problem areas. At f_{s3} = 353 Hz the main problem is situated in the ventilation bracket where the sound intensity, as shown in Figure 7.8b, is very high in this area in particular.

Following the identification of the major problem areas for this product, a number of anti-noise measures can be taken. After these measures are applied to the product, again, the near-field sound imaging tests may be performed to compare the improvements to the old situation and identify the next level of noise sources that require treatment.

7.4 Conclusions

This chapter has illustrated the applicability of Fourier based near-field sound imaging for industrial practice. It is shown that the embodiments from chapter 6 are applied and properly operating in practice, even under harsh conditions, outside an anechoic chamber. The hard disk drive case showed great correspondence between laser vibrometer measurements and acoustic inversion from sound pressure at z_h = 1 cm to normal direction particle velocity on the top cover, especially when the automated process with linear predictive border-padding and COS iteration with ζ-criterion is applied. The second case with the cylinder surface illustrated the possibility of NAH operating on a different geometry than, the usually applied, planar NAH. The external Cylindrical NAH system requires hologram measurements on a cylindrical aperture with a constant radius with respect to the center of the source cylinder of interest. The results show the clear visualization of circular modes for future dynamical model verification and non-parallel excitation by the shaker. Finally, a large scale, low spatial sound image resolution case was treated that consists of a hydraulic generator used in construction. The measurements were successfully performed outside with a portable line array system. The results give insight into the main disturbances and their behavior, with clear problems identified at

the exhaust on the top, the ventilation brackets and the base plate. Results from these and comparable cases are a great step forward in the understanding and identification of the acoustic and vibrational sources in industrial products and systems.

Conclusions and Recommendations

8.1 Conclusions

This thesis describes the development, implementation, application and testing of a fully automated Fourier based near-field sound imaging system that is capable of spatial resolutions below one millimeter. The main problem areas for practical application of Fourier based NAH have been identified and possible solutions have been put forward. The key contributions of this thesis are proper spatial sampling, data-based hologram extrapolation and k-space regularization with modified filter functions and Cut-Off and Slope (COS) stopping rules. Furthermore, this thesis has shown the importance of all the individual elements in the total sound imaging system, from measurement set-up to eventual visualization and interpretation, which are carefully integrated and working as a unity. The resulting automated near-field sound imaging technology Eindhoven (ANSITE) system has shown practical relevance and utility in industry during this research, while the main system components have been scientifically validated.

More into detail, the following achievements were made in this thesis:

- Spatial sampling, sensor dimensions, measurement noise and standoff distance are very important factors in the determination of the spatial sound image resolution (SSIR), as is shown in chapter 2. If the standoff distance is too small, compared to the spatial sensor resolution and signal-to-noise ratio (SNR), it is possible that spatial aliasing occurs. The standoff distance or spatial sensor resolution acts as a natural anti-aliasing filter. It is also shown that the ratio between the maximum evanescent and propagating wave amplitudes (EPR) at the source is a crucial factor in the determination of the optimal standoff distance.

- In chapter 3, a truncated hologram aperture extrapolation method based on an autoregressive model, called linear predictive border-padding, is introduced. This method is used to counter the difficulties with spatial windowing for Fourier based NAH in a fast and converging manner. The strategy to pre-process the spatial acoustic data before the FFT is applied is robust and minimizes leakage and distortion of the acoustic field. By decoupling the spatial pre-processing from inverse propagation and regularization, a highly versatile method, without any pre-knowledge of noise color and variance, resulted. The use of hologram aperture data to implement a physically relevant filter and extrapolate the finite aperture shows great improvements compared to standard windowing and other forms of data extrapolation, which have also been compared to each other numerically.

- The newly introduced modified exponential filter, combined with the Cut-Off and Slope (COS) iteration method and a ζ-criterion (based on the L-curve criterion) in chapter 4 out-performs all filter function and stopping rule combinations that have been tested in this thesis in case of medium to good noise conditions. Overall, the results show that the optimal regularization method depends heavily on the type of source, the spatial source distribution and the signal-to-noise ratio of the hologram data.

- The practical relevance of the methods that were introduced in this thesis has been illustrated in chapter 5 with experimental results which followed from measurement set-ups in an anechoic environment. It has been found that the overall best regularization performance is achieved by the automated COS with ζ-criterion regularization method in combination with the modified exponential filter, which is in full agreement with the numerical experiments.

- Furthermore, the high resolution case study has shown that the spatial sound image resolution, which has been derived in chapter 2, is strongly dependent on the EPR. In the three point sources case, the evanescent part at the source is much stronger than the propagating part, which influences the spatial aliasing conditions heavily. The derived spatial resolution formula results in the classical resolution definition by Maynard and Williams (29) when $EPR = 0$ dB, however, the obtainable SSIR becomes smaller when $EPR > 0$.

- Linear predictive border-padding has been compared to a number of other spatial anti-leakage and windowing methods for Fourier based NAH. Here, it is shown that linear predictive border-padding is superior in all shown cases to spatial windowing and spline border-padding. Also, these practical results show much similarity with the numerical experiments in chapter 3.

- In chapter 6, a system is described that automatically determines an "appropriate" solution for the provided inverse problem, which takes away the burden of the end-

user. The ANSITE system provides accurate, automated sound field visualization. The sound imaging system helps localize and analyse sound sources in existing and new products. Such a system can be operated by a non-expert in the field of acoustic measurements, although some training may be required.

- The system can be used to measure e.g. small objects like a mobile phone, large objects like a truck, and everything in between. Possible system configurations include: Serial single sensor, line or full-sensor array measurements over a pre-defined grid with a traverse robot and an object in a special clamping unit in or outside an anechoic room; A static or portable full array measurement with sensors able to determine the distance to the object in front of the array.

- Experiments on industrial cases have been performed. These experiments have shown a wide applicability of Fourier based NAH for a large number of different source types and aperture sizes. The processing speed and ease of use of Fourier based NAH in a combination with linear predictive border-padding is particularly well-suited for fast processing, which is much appreciated in industrial practice. chapter 7 has illustrated the results and ways of interpretation of the resulting sound images. The ANSITE system is used to identify noise sources, to provide more insight into the origination and propagation of sound waves in front of the object of interest, and to provide a highly accurate quantitative analysis of the source.

8.2 Recommendations

Although the near-field sound imaging system that has been developed and described in the previous chapters is fully functioning and working properly, there are always questions and uncertainties remaining, in particular the following subjects are of interest:

- Further investigation of the consequences of the EPR in spatial sound image resolution and the spatial aliasing problems is required, in order to develop a framework which allows to better predict or detect possible spatial aliasing. Special attention should be paid to the determination of the EPR directly from measurements.

- Besides extrapolation of the aperture edges outward, border-padding is also applicable to fill gaps in the hologram aperture. This allows the use of several patches along the area of interest with non-equidistant measurement grids, since border-padding permits coupling of the separate patches to form a rectangular grid. The goal is to develop methods to apply linear predictive border-padding to fill gaps in the aperture or in between different hologram parts.

- Expand the possibilities and processing speed of the COS algorithm even more and explore new ways to weigh the perturbation (noise blow-up) and filter errors (over-

smoothing). Interesting new developments are introduced in (8) where a parameter choice method called Normalized Cumulative Periodogram (NCP) is introduced, for example.

- Investigate the influence of sensors in the near-field of the sound source. This influence becomes specifically important for very high resolutions, large and dense arrays of sensors and short standoff distances. Possible disturbances like (back) scattering, reflections and acoustic impedance changes are of special interest in these cases.

- A double layered array can be used to differentiate between waves originating from the source and waves originating or reflecting from behind. A method is required that filters background noise and reflections, which allows for measurements in acoustically hazardous areas. In practice, a portable array is mostly used in an industrial environment, outside an anechoic environment. Waves from the back and sides need to be detected, because they are originating from the (in theory) source-free area and should thus be canceled out. Recently, a method was introduced that is intended to deal with this problem (13; 21), however a Fourier based method should be found which could directly be integrated in the Fourier-based NAH framework developed in this thesis.

Bibliography

[1] J.S. Bendat and A.G. Piersol, *Measurement and analysis of random data*, John Wiley and Sons, New York, 1966.

[2] J.P. Burg, *Maximum entropy spectral analysis*, Ph.D. thesis, Stanford University, CA, United States of America, 1975.

[3] J.W. Cooley and J.W. Tukey, *An algorithm for the machine calculation of complex fourier series*, Mathematics of Computation **19** (1965), 297–301.

[4] P. Craven and G. Wabba, *Smoothing noisy data with spline functions*, Numerical Mathematics **31** (1979), 377–403.

[5] D. Gabor, *A new microscopic principle*, Nature **161** (1948), 777–778.

[6] D. Gabor, *Microscopy by reconstructed wave-fronts*, Proceedings of the Royal Society of London. Series A, Mathematical and Physical Sciences **197** (1949), no. 1051, 454–487.

[7] B.K. Gardner and R.J. Bernhard, *A noise source identification technique using an inverse helmholtz integral equation method*, ASME Transactions Journal of Vibration Acoustics **110** (1988), 84–90.

[8] J. Gomes and P.C. Hansen, *A study on regularization parameter choice in near-field acoustical holography*, Proceedings of Acoustics 2008 (2008).

[9] J. Hadamard, *Lectures on cauchy's problem in linear partial differential equations*, Yale University Press, New Haven, 1923.

[10] J. Hald, *Stsf - a unique technique for scan-based near-field acoustic holography without restrictions on coherence*, Tech. Report 1, Brüel & Kjær Technical Review, 1989.

[11] J. Hald, *Stsf - a unique technique for scan-based near-field acoustic holography without restrictions on coherence*, Tech. Report 2, Brüel & Kjær Technical Review, 1989.

[12] J. Hald, *Patch near-field acoustical holography using a new statistically optimal method*, Proceedings of Internoise 2003, Seogwipo, Korea (2003), 2203–2210.

[13] J. Hald, *Patch holography using a two-layer handheld array with an extended sonah algorithm*, Proceedings of Euronoise 2006, Tampere, Finland (2006).

[14] J. Hald, J. Mørkholt, P. Hardy, D. Trentin, M. Bach-Andersen, and G. Keith, *Array bases measurement of radiated and absorbed sound intensity components*, Proceedings of Acoustics 2008, Paris, France (2008).

[15] P.C. Hansen, *Rank-deficient and discrete ill-posed problems*, Ph.D. thesis, Technical University of Denmark, Lyngby, Denmark, 1996.

[16] P.C. Hansen, T.K. Jensen, and G. Rodriguez, *An adaptive pruning algorithm for the discrete l-curve criterion*, Journal of Computational and Applied Mathematics **198** (2006), 483–492.

[17] F.J. Harris, *On the use of windows for harmonic analysis with the discrete fourier transform*, Proceedings of the IEEE **66** (1978), 61–83.

[18] Z. Havranek and L. Bejcek, *Local patch acoustic holography methods in enclosed spaces*, Proceedings of Acoustics 2008, Paris, France (2008).

[19] S. Haykin, *Adaptive filter theory, 3rd edition*, Prentice-Hall, Upper Saddle River, United States of America, 1996.

[20] J. Ih, J. Kim, and B. Kim, *Acoustic field prediction of complex radiators by using near-field measurements and bem*, Proceedings of the 11th International Modal Analysis Conference, Florida (1993), 1396–1401.

[21] F. Jacobsen, X. Chen, and V. Jaud, *A comparison of statistically optimized near field acoustic holography using single layer pressure-velocity measurements and using double layer pressure measurements*, The Journal of the Acoustical Society of America **123** (2008), no. 4, 1842–1845.

[22] S.V. Kalinin, S. Jesse, B.J. Rodriguez, J. Shin, A.P. Baddorf, H.N. Lee, A. Borisevich, and S.J. Pennycook, *Spatial resolution, information limit, and contrast transfer in piezoresponse force microscopy*, **17** (2006), 3400–3411.

[23] I. Kauppinen, *Reconstructon method for missing or damaged long portions in audio signal*, Journal of the Audio Engineering Society **49** (2001), 1167–1180.

[24] B. Kim and J. Ih, *On the reconstruction of the vibro-acoustic field over the surface enclosing an interior space using the boundary element method*, The Journal of the Acoustical Society of America **100** (1996), no. 5, 3003–3016.

[25] Y. Kim and P.A. Nelson, *Spatial resolution limits for the reconstruction of acoustic source strength by inverse methods*, Journal of Sound and Vibration **265** (2003), 583–608.

[26] G.H. Koopmann, L. Song, and J.B. Fahnline, *A method for computing acoustic fields based on the principle of wave superposition*, **86** (1989), no. 6, 2433–2438.

[27] N.J. Mallon, *Dynamic stability of thin-walled structures: a semi-analytical and experimental approach*, Ph.D. thesis, Eindhoven University of Technology, 2008.

[28] N.J. Mallon, R.H.B. Fey, and H. Nijmeijer, *Dynamic stability of a thin cylindrical shell with top mass subjected to harmonic base-acceleration*, International Journal of Solids and Structures **45** (2008), no. 6, 1587–1613.

[29] J.D. Maynard, E.G. Williams, and Y. Lee, *Nearfield acoustic holography: I. theory of generalised holography and the development of nah*, The Journal of the Acoustical Society of America **78** (1985), 1395–1413.

[30] A.F. Metherell, H.M.A. El-Sum, J.J. Dreher, and L. Larmore, *Introduction to acoustical holography*, The Journal of the Acoustical Society of America **42** (1967), no. 4, 733–742.

[31] P.A. Nelson and S.H. Yoon, *Estimation of acoustic source strength by inverse methods: Part i, conditioning of the inverse problem*, Journal of Sound and Vibration **233** (2000), 643–668.

[32] A.V. Oppenheim, *Digital signal processing*, Prentice-Hall, Englewood Cliffs, United States of America, 1975.

[33] D.L. Phillips, *A technique for the numerical solution of certain integral equations of the first kind*, J. Assoc. Comput. Mach. **9** (1962), 84–97.

[34] K. Preston and J.L. Kreuzer, *Ultrasonic imaging using a synthetic holographic technique*, Applied Physics Letters **10** (1967), no. 5, 150–152.

[35] J.W.S. Rayleigh, Phil. Mag. **42** (1896), no. 5, 493–498.

[36] F.F. Sabins, *Remote sensing*, W.H. Freeman and Company, San Francisco, United States of America, 1978.

[37] K. Saijyou and S. Yoshikawa, *Accuracy improvement of reconstruction in near-field acoustical holography by applying data extrapolation method*, Japanese Journal of Applied Physics **37** (1998), 3022–3027.

[38] K. Saijyou and S. Yoshikawa, *Reduction methods of the reconstruction error for large-scale implementation of near-field acoustical holography*, The Journal of the Acoustical Society of America **110** (2001), no. 4, 2007–2023.

[39] A. Sarkissian, *Extension of measurement surface in near-field acoustic holography*, The Journal of the Acoustical Society of America **115** (2004), 1593–1596.

[40] A. Sarkissian, *Method of superposition applied to patch near-field acoustic holography*, The Journal of the Acoustical Society of America **118** (2005), no. 2, 671–678.

[41] R. Scholte, I. Lopez, and N.B. Roozen, *Quantitative and qualitative verification of pressure and velocity based planar near-field acoustic holography*, Proceedings of the 13th International Congress on Sound and Vibration, Vienna, Austria (2006).

[42] R. Scholte, I. Lopez, N.B. Roozen, and H. Nijmeijer, *Application of high precision k-space filters and stopping rules for fully automated pnah*, Proceedings of the 14th International Congress on Sound and Vibration, Cairns, Australia (2007).

[43] R. Scholte, I. Lopez, N.B. Roozen, and H. Nijmeijer, *Experimental application of high precision k-space filters and stopping rules for fully automated near-field acoustic holography*, International Journal of Acoustics and Vibration **accepted** (2008).

[44] R. Scholte, I. Lopez, N.B. Roozen, and H. Nijmeijer, *Truncated aperture extrapolation for fourier-based near-field acoustic holography by means of border-padding*, The Journal of the Acoustical Society of America **conditionally accepted** (2008).

[45] R. Scholte, I. Lopez, N.B. Roozen, and H. Nijmeijer, *Wavenumber domain regularization for near-field acoustic holography by means of modified filter functions and cut-off and slope iteration*, ACTA Acustica United with Acustica **94** (2008), 339–348.

[46] R. Scholte, N.B. Roozen, and I. Lopez, *Regularization in pnah by means of l-curve*, Proceedings of Forum Acusticum 2005, Budapest, Hungary (2005).

[47] R. Scholte, N.B. Roozen, and I. Lopez, *Spatial sampling and aliasing in acoustic imaging*, Proceedings of the 12th International Congress on Sound and Vibration, Lisbon, Portugal (2005).

[48] R. Steiner and J. Hald, *Near-field acoustical holography without the errors and limitations caused by the use of spatial dft*, Proceedings of the 6th International Congress on Sound and Vibration (1999), 843–850.

[49] R. Steiner and J. Hald, *Near-field acoustical holography without the errors and limitations caused by the use of spatial dft*, International Journal of Acoustics and Vibration **6** (2001), 83–89.

[50] A.N. Tikhonov, *Solution of incorrectly formulated problems and the regularization method*, Soviet Math. Dokl. **4** (1963), 1035–1038.

[51] N.P. Valdivia, *Study of the comparison of the methods of equivalent sources and boundary element methods for near-field acoustic holography*, The Journal of the Acoustical Society of America **120** (2006), no. 6, 3694–3705.

[52] W.A. Veronesi and J.D. Maynard, *Digital holographic reconstruction of source with arbitrarily shaped surfaces*, The Journal of the Acoustical Society of America **85** (1989), no. 2, 588–598.

[53] R. Visser, *A boundary element approach to acoustic radiation and source identification*, Ph.D. thesis, University of Twente, 2004.

[54] Z. Wang, *Helmholtz equation-least squares hels method for inverse acoustic radiation problems*, Ph.D. thesis, Wayne State University, Detroit, 1995.

[55] Z. Wang and S.F. Wu, *Helmholtz equationŰleast-squares method for reconstructing the acoustic pressure field*, The Journal of the Acoustical Society of America **102** (1997), no. 4, 2020–2032.

[56] E.G. Williams, *Fourier acoustics: Sound radiation and nearfield acoustical holography*, Academic, London, Great-Brittain, 1999.

[57] E.G. Williams, *Regularization methods for near-field acoustical holography*, The Journal of the Acoustical Society of America **110** (2001), no. 4, 1976–1988.

[58] E.G. Williams, *Continuation of acoustic near-fields*, The Journal of the Acoustical Society of America **113** (2002), no. 3, 1273–1281.

[59] E.G. Williams and J.D. Maynard, *Holographic imaging without the wavelength resolution limit*, Phys. Rev. Lett. **45** (1980), 554–557.

Summary

Noise pollution is a generally acknowledged problem in modern day society. The current tendencies towards lightweight and cheaper product design are primarily responsible for increasing nuisance, annoyance and environmental problems caused by acoustic noise. There are several reasons for research towards technologies that facilitate acoustic noise reduction. Nowadays, low noise design of consumer electronics, high-tech systems and automotive are restricted to increasingly stringent regulations and quality aspects. Effective countermeasures in order to reduce sound radiation are only taken when the source of sound is known. "Inverse Acoustics" is a very effective method to visualize and quantize the sound sources, which reconstructs source information based on measurements away from the source, yet in the near-field. In fact, the system is able to reconstruct the entire acoustic message that a source radiates in the direction of interest. The current methods for source reconstruction produce sound images with very little detail, they often require cumbersome numerical calculations and models, and they are often highly impractical for industrial applications. This research focuses on fast and accurate measurement and signal processing methods for inverse acoustics that are applicable in practical situations which require high resolutions under hazardous acoustic conditions. The inverse process is based upon spatial and wavenumber domain Fourier techniques, also referred to as Near-field Acoustic Holography. More in detail, spatial properties with respect to aliasing, leakage, signal-to-noise ratio and sensor set-ups are investigated and explicit methods and rules are developed to assist in proper determination of the acoustic holograms. In order to correctly transform the spatial hologram data into the wavenumber domain or k-space, a method called border-padding is developed. This method, which is an alternative to spatial windowing, is highly accurate without slowing down the processing time considerably. Another important factor is regularization, which is required since the inverse process is highly ill-posed. Without proper filtering action taken, noise blows up as the hologram-source distance or the wavenumber grows. In this research project a method is developed to automatically determine the proper filter function and filter parameters, which is a near-optimal trade-off between noise blow-up and deterioration of useful source information. These important properties are combined in a fully

automated near-field sound imaging system design. At the Technical University of Eindhoven two versions of this system were developed and built; a large version that is based in the semi-anechoic room of the laboratory and a portable system that is suitable for small electronic devices and high-tech systems. A number of practical cases are used to qualitatively as well as quantitatively validate the improvements with respect to existing methods and illustrate the possibilities for industrial application.

Samenvatting

Geluidsoverlast is een erkend probleem in de huidige moderne maatschappij. De oplopende irritatie, overlast en schade aan het leefmilieu door akoestische verstoring worden in de eerste plaats veroorzaakt door de trend richting lichtgewicht en goedkoper productontwerp. Er zijn meerdere redenen om het onderzoek naar methodes die geluids- en verstoringsonderdrukking beter inzichtelijk en mogelijk maken. In de huidige industriële praktijk van consumenten elektronica, high-tech systemen en automotive moeten producenten aan immer strenger wordende eisen wat betreft geluid emissies en kwaliteitseisen voldoen. Effectieve maatregelen die geluidsafstraling minimaliseren zijn enkel mogelijk wanneer de bron van het geluid bekend is. Inverse akoestiek is een verzamelnaam voor efficiënte methodes, die het mogelijk maken geluidsbronnen te visualiseren en kwantificeren op basis van ruimtelijke metingen van geluid op een bepaalde afstand van de bron, in het nabijheidsveld. Sterker nog, het systeem is in staat tot op zekere afstand van de bron, in elke gewenste richting, het gehele geluidsveld te berekenen. De huidige methoden voor geluidsbron reconstructie resulteren over het algemeen in geluidsbeelden met relatief lage resoluties, waarbij daarnaast gebruik moet worden gemaakt van zware numerieke berekeningen en modellen, waardoor het in veel gevallen niet praktisch is voor de industriële toepassing. Dit onderzoek richt zich op snelle en nauwkeurige meet- en signaalverwerkingsmethoden voor inverse akoestiek, die goed toepasbaar zijn in praktische situaties die een hoge resolutie vereisen, onder moeilijke akoestische omstandigheden. Het inverse proces is gebaseerd op Fourier transformaties in het plaats en golfgetal domein, wat ook wel 'Near-field Acoustic Holography' wordt genoemd. Specifiek wordt er aandacht besteedt aan het onderzoek naar spatiële eigenschappen op het gebied van 'aliasing', 'leakage', signaal-ruis verhouding en plaatsing of keuze van sensoren, op basis hiervan worden er regels en richtlijnen vastgesteld bij de meting en bepaling van akoestische hologrammen. Een nieuwe methode genaamd border-padding is ontwikkeld waarmee een geoptimaliseerde transformatie van de spatiële hologramsinformatie mogelijk gemaakt wordt. Deze methode, die in feite een alternatief is op de toepassing van spatiële 'windows', is zeer nauwkeurig zonder dat het berekeningsproces merkbaar vertraagd wordt. Een andere belangrijke factor in het proces is regularisatie,

die noodzakelijk is wanneer een inverse proces zeer slecht geconditioneerd is. Zonder adequate filters blaast de meetruis op wanneer de afstand tot de bron of het golfgetal toeneemt. Tijdens dit onderzoeksproject is een methode ontwikkeld die automatisch de juiste filter functie en instellingen bepaald, dit is een bijna optimale afweging tussen het opblazen van ruis en het wegfilteren van nuttige informatie over de bron. De voorgaande eigenschappen worden gecombineerd in het ontwerp van een volledig geautomatiseerd 'near-field sound imaging' systeem. Twee versies van dit systeem zijn inmiddels op de Technische Universiteit Eindhoven ontworpen en gerealiseerd; een grote versie die in de semi-anechoïsche ruimte wordt ingezet en een portable systeem dat geschikt is voor kleine elektronische apparaten en high-tech systemen. Een aantal praktijkvoorbeelden worden ingezet om het systeem en de verbetering ten opzichte van bestaande methoden kwantitatief en kwalitatief te valideren voor industriële toepassing.

Dankwoord / Acknowledgements

Dit proefschrift zou niet bestaan zonder de hulp, ondersteuning en inbreng van vele mensen. Ze allemaal noemen zou teveel ruimte innemen, maar ik doe toch een poging de belangrijkste mensen te benoemen en bij deze te bedanken. Allereerst bedank ik mijn eerste promotor Prof. Bert Roozen, die me de kans gaf mijn dromen te laten ontstaan tijdens mijn stage bij Philips, om deze vervolgens te kunnen realiseren in dit promotie project. Daarnaast wil ik mijn tweede promotor Prof. Henk Nijmeijer bedanken voor de uitstekende ondersteuning, goede gesprekken, het in goede banen leiden van mijn (soms) onbegrensde enthousiasme, de samenwerking en het groeiende plezier op het gebied van valorisatie en de kritische blik op mijn werk. Uiteraard mag mijn copromotor Dr. Ines Lopez niet in dit rijtje ontbreken. Ik wil Ines graag bedanken voor de creatieve sessies, de inhoudelijke inbreng in mijn werk en de fijne samenwerking en prettige gesprekken over van alles en nog wat. Ook wil ik de overige leden van de promotiecommissie, te weten Prof. André de Boer, Prof. Wim Desmet, Prof. Eddy Gerretsen en Dr. Earl G. Williams bedanken voor het aandachtig lezen, bediscussiëren en becommentariëren van mijn werk.

Ik wil STW bedanken voor hun financiële ondersteuning van dit project, de mede projectgenoten aan de Universiteit van Twente en de leden van de gebruikerscommissie voor de interessante discussies en nuttige inbreng tijdens de gebruikerscommissie en project vergaderingen. Naast alle wetenschappelijke zaken is het ook van groot belang het ontwikkelde in praktijk te brengen en te testen. Een grote rol hierin heeft Pieter van Hoof gespeeld, waarvoor mijn dank. Daarnaast wil ik ook mijn dank uiten aan Harrie van de Loo, Peter Hamels, Jan de Vries, Rens Kodde, de mannen van GTD en alle mensen van de praktische ondersteuning. In het bijzonder wil ik mijn kamergenoten Theo Hofman en Joris van den Boom bedanken voor de vele uurtjes discussie, brainstorms, goede gesprekken en plezier. Verder wil ik de studenten Xander Schuurbiers, Pasquale Romagnano, Osman Dönmez, Ferhad Kamalizadeh en Matthijs Verweijmeren, die ik de afgelopen jaren heb mogen begeleiden, bedanken. Daarnaast alle zeer gewaardeerde (oud) collega's die de afgelopen jaren mijn verblijf op de TU/e nog een stuk aangenamer

en interessanter hebben gemaakt, waarbij ik in het bijzonder Apostolos, Arjen, Dennis, Erik, Ewout, François, Jan, Jeroen, Jeroen, Lia, Matthijs, Niels, Niels, Petra, Ramon, René, Rob, Rob, Roel, Stan, Tijs, Thijs, Tom, Willem-Jan en Wouter wil noemen.

Uiteraard wil ik ook familie en vrienden bedanken voor het aanhoren van al mijn geluid over geluid en de broodnodige ontspanning en andere zaken die belangrijk zijn in het leven. Vooral de trip naar London met Ex-heren3 tijdens de laatste loodjes van het schrijven van mijn proefschrift en het opknappen van het nieuwe huis van Robin en Jenine hebben me heel veel goed gedaan. Tenslotte zijn er twee mensen die ik in het bijzonder wil bedanken voor hun oneindige steun en warmte tijdens mijn promotie periode, maar ook zeker in de hele weg daar naartoe: mijn ouders Chris en Lucy.

Curriculum Vitae

Rick Scholte was born on March 24th, 1979 in Zwolle, the Netherlands. After finishing secondary school at the Carolus Clusius College in Zwolle in 1997, he studied Electrical Engineering at the University of Twente (UT), Enschede, the Netherlands. During his internship at Philips Centre for Industrial Technology (currently known as Philips Applied Technologies) in Eindhoven, he worked on an Acoustic Holography set-up. Following this internship, Philips invited him to perform his M.Sc. project at Philips as part of an acoustic imaging research project. During his M.Sc. project, which he successfully finished in March 2004, the potential of acoustic imaging emerged and a number of problems of industrial partners were handled by the acoustic system he designed. Subsequently, a Ph.D. project proposal was subjected to and funded by the Dutch Technology Foundation (STW). The project called "Inverse Acoustics" is a cooperation between the Eindhoven University of Technology and the University of Twente. Since July 2004, he is one of the Ph.D. students in the aforementioned project, specifically working on acoustic signal processing, in the Dynamics and Control group at the department of Mechanical Engineering of the Eindhoven University of Technology. The results of this research are presented in this thesis. As a result of his growing interests to utilize his research, in December 2007, he received a Valorisation Grant provided by STW for a new high-tech business development initiative called "Sound Imaging, a Sound Business". He is planning to launch a Sound Imaging company early 2009.